UNIVERSITÀ DEGLI STUDI DI PADOVA

Dipartimento di Fisica e Astronomia "Galileo Galilei"

Master Degree in Physics

Final Dissertation

Phenomenology of Axion Models with a Light Radial Mode

Thesis supervisor

Prof. Luca Di Luzio

Thesis co-supervisor

Dr. Philip Sørensen

Candidate

Andrea Zoppi

Academic Year 2025/2026

Abstract

The QCD axion is one of the most well-motivated extensions of the Standard Model. It provides an elegant solution to the strong CP problem while also delivering a non-thermal mechanism for dark matter production. In field theoretical models, the axion is identified as the light angular mode of a complex scalar field, while the heavy radial mode is integrated out. However, if the radial mode is sufficiently light, it can give rise to interesting dynamics and phenomenology. This thesis aims to investigate the cosmological dynamics of such a light radial mode and its implications for the QCD axion through the parametric resonance mechanism, building on the framework proposed by Co, Hall, and Harigaya (Phys. Rev. Lett. 120, 211602 (2018)). We generalize this framework, demonstrating that the radial mode can account for a significant fraction of the present-day dark matter abundance, while critically examining both the strengths and limitations of this scenario. Since this mechanism is intrinsically non-linear, we present a detailed analytical treatment and validate our results through lattice simulations. Finally, we derive theoretical and experimental constraints on the light radial mode arising from the Scalar-Higgs portal interaction.

Contents

Convention and acronyms

Convention

We adopt a mostly plus signature for both M_4 and the spatially flat FLRW metric, with line elements

$$ds^2_{M_4} = -dt^2 + dx^2 + dy^2 + dz^2,$$
$$ds^2_{\mathrm{FLRW}} = -dt^2 + R^2(t)\left(dx^2 + dy^2 + dz^2\right),$$

while $g_{\mu\nu}$ refers to a generic metric.
The affine connection is given by

$$\Gamma^{\mu}_{\nu\alpha} = \frac{1}{2} g^{\mu\sigma}(-\partial_\sigma g_{\nu\alpha} + \partial_\nu g_{\sigma\alpha} + \partial_\mu g_{\nu\alpha}).$$

Natural units are employed: $c = \hbar = k_B = 1$.

Acronyms

DM: dark matter

PR: parametric resonance

QCD: Quantum Chromodynamics

mis: misalignment mechanism

PQ: Peccei-Quinn

ALP: axion-like particle

SM: Standard Model

SSB: spontaneous symmetry breaking

VEV: vacuum expectation value

UV: ultraviolet

IR: infrared

(p)NGB: (pseudo)Nambu-Goldstone bosons

EW: electroweak

RD/MD: radiation/matter domination

EOM: equation of motion

CDI: cold dark matter isocurvature

CMB: Cosmic Microwave Background

EBL: Extragalactic background light

ISL: Inverse-Square Law

EEP: Einstein Equivalence Principle

WEP: Weak Equivalence Principle

NDA: Naive Dimensional Analysis

exp: experimental

RH: reheating

BBN: Big Bang Nucleosynthesis

GUT: Grand Unification Theory

QG: Quantum Gravity

RGEs: Renormalisation Group Equations

FLRW: Friedmann-Lemaître-Robertson-Walker

Introduction

The Standard Model (SM) of particle physics is the quantum field theory that successfully unifies electromagnetic, weak, and strong interactions. Despite its remarkable experimental success, some observations, such as the existence of dark matter (DM) or the non-zero neutrino masses, constitute indisputable evidence that the present theory must be extended. In addition to these, the SM presents theoretical puzzles associated with unexplained small numbers, such as the cosmological constant and the CP-violating QCD angle, constrained by experiment to satisfy $|\bar{\theta}| \lesssim 10^{-10}$.

One of the most compelling extensions of the SM is provided by the QCD axion [1, 2], which dynamically solves the strong CP problem while providing a natural DM candidate. The construction requires a Lagrangian equipped with a global $U(1)_{\mathrm{PQ}}$ symmetry, exact at the classical level but anomalous under QCD, which is spontaneously broken at the UV scale f_a. Such a symmetry is known as Peccei-Quinn (PQ) symmetry after its proposers [3, 4]. Generally, this setup is achieved by a complex scalar field Φ. The axion is then identified with the angular mode of Φ, corresponding to the pseudo-Nambu-Goldstone-Boson (pNGB) associated with the broken $U(1)_{\mathrm{PQ}}$, while it is generally assumed that the radial excitation is heavy and integrated out.

The QCD axion has profound implications for cosmology. Through the misalignment mechanism [5–7], it can account for a significant fraction of the observed cold DM abundance, and if the PQ symmetry is broken after inflation, the subsequent decay of the network of cosmic strings and domain walls [8, 9] provides an additional contribution. Within this elegant theoretical framework, the QCD axion is particularly compelling because of its potential experimental accessibility. A broad experimental programme is currently investigating the axion parameter space using a variety of complementary approaches [10], and the next generation of experiments is expected to explore much of the parameter space associated with the QCD axion.

A recent analysis in Ref. [11] demonstrated that, for large initial values of the complex field, the cosmological evolution can efficiently produce a population of axion and radial fluctuations via parametric resonance. This mechanism involves genuinely non-linear dynamics and therefore cannot be treated fully analytically; the authors followed the evolution under a set of assumptions, which we review and adopt throughout this work. The parametric resonance mechanism is distinguished from the misalignment mechanism and the decay of the cosmic string by the region of parameter space it selects: a smaller axion decay constant f_a. The price to pay is the presence of a radial mode whose mass lies well below the energy scale f_a, which constitutes the underlying assumption of the scenario. Several experimental efforts are currently targeting this region of parameter space, such as IAXO [12] and CAST [13] for solar axions, MADMAX [14] and BREAD [15] for halo axions.

This thesis is devoted to the analysis of the cosmological implications of a light radial mode in the context of QCD axion models, and is organised as follows. In Chapter 1 we review the basics of axion cosmology and the dynamics of a scalar field in an expanding Universe. In Chapter 2, we turn to the central topic of the thesis: the cosmological role of a light radial mode and its impact on the QCD axion. Working in the minimal setup containing only the axion and the radial mode, following the framework of Co et al. [11], we analyse in more detail the production of axion and radial fluctuation from the parametric resonance mechanism. We highlight key challenges inherent to this scenario and demonstrate that the radial population can constitute a significant fraction of the observed DM abundance. The intrinsic non-linear nature of the dynamics makes a purely analytical treatment insufficient; accordingly, Appendix A presents a preliminary lattice simulation of the parametric resonance, which allows us to follow the field evolution beyond the linear regime, and test the validity of the assumptions adopted in Chapter 2 and in Ref. [11]. In Chapter 3 we extend the minimal setup by coupling the radial mode to the SM field content through the simplest renormalisable interaction, the Scalar–Higgs portal. Finally, in Chapter 4, we derive the experimental bounds on the light scalar with a Higgs portal, drawing on cosmological, astrophysical, and laboratory experiments. More technical details on the behaviour of a scalar field during inflation, the thermalisation of the radial condensate, and the numerical evolution in standard misalignment are provided in Appendix B, C, and D.

Chapter 1

An overview of axion cosmology

1.1 Basics of cosmology and thermodynamics in the Early Universe

The expanding universe. The Universe is homogeneous and isotropic at spatial scales larger than 10^2 Mpc. It is described by the translation and rotation invariant Friedmann-Lemaître-Robertson-Walker (FLRW) metric, in comoving coordinates

$$ds^2_{FLRW} = -dt^2 + R(t)^2 \left[\frac{dr^2}{1-kr^2} + r^2 d\theta^2 + r^2 \sin(\theta)^2 d\phi^2 \right] \overset{\text{(if k=0)}}{=} -dt^2 + R^2(t)[dx^2 + dy^2 + dz^2], \tag{1.1}$$

where $R(t)$ is the scale factor and $k = 0, \pm 1$ is a constant that describes the global geometry ($k = 0$ for flat, $k = +1$ for closed, i.e., the geometry of a sphere, and $k = -1$ for open geometry, i.e., the geometry of a hyperbolic surface). In this thesis, we will work with $k = 0$ in agreement with the experimental measurements.
Due to the symmetry of the FLRW metric, the calculation of the affine connection is particularly simple [16]. The non-zero components are:

$$\Gamma^0_{ij} = R\dot{R}\delta_{ij}, \quad \Gamma^i_{0j} = \frac{\dot{R}}{R}\delta^i_j, \quad \dot{} \equiv \frac{d}{dt}. \tag{1.2}$$

The matter-energy content of the Universe is modelled as a generic fluid, whose stress-energy tensor [17] is constrained by the homogeneity and isotropy to have the form

$$T^\mu_\nu = \text{diag}(-\rho, p, p, p), \tag{1.3}$$

where ρ is the energy density and p the pressure. The stress-energy tensor obeys the conservation law $\nabla_\mu T^{\mu\nu} = 0$. In such a Universe, Einstein's equations of General Relativity specialise to the Friedmann equations,

$$H^2 = \frac{8\pi G}{3}\rho, \quad \frac{\ddot{R}}{R} = -\frac{4\pi G}{3}(\rho + 3p). \tag{1.4}$$

Here, $H \equiv \dot{R}/R$ is the Hubble expansion rate, and the present value is the so-called Hubble constant, where

$$H_0 = h\frac{100 \text{ km}}{\text{sec} \cdot \text{Mpc}} = 2.1\ h\ 10^{-33}\text{eV}. \tag{1.5}$$

There is an uncertainty in h: based on Planck cosmological data [18], the current determination leads to $h = 0.674 \pm 0.005$, while alternative determinations based on late-time observations [19] find higher values $h = 0.73 \pm 0.01$. In this thesis, we will take the numerical value $h \sim 0.7$.

In the spatially flat metric, the current energy density is equal to the critical density,

$$\rho_{\text{crit}} \equiv \frac{3H_0^2}{8\pi G}\,. \tag{1.6}$$

Matter-energy content. A simple equation of state describes many components of the Universe,

$$p = w\rho, \quad w = \text{cost}. \tag{1.7}$$

From the conservation-of-energy equation, $\nabla_\mu T^{\mu 0} = 0$, we obtain that the energy density scales as

$$\rho \propto R^{-3(1+w)}. \tag{1.8}$$

The relevant cases are:

- $w = 0$ describes non-relativistic matter (dust), $p_m = 0$ and $\rho_m \propto R^{-3}$.
- $w = 1/3$ describes relativistic particles (radiation), $p_r = \frac{1}{3}\rho_r$ and $\rho_r \propto R^{-4}$.
- $w = -1$ describes vacuum energy, $p_\Lambda = -\rho_\Lambda$ and $\rho_\Lambda \propto \text{cost}$.

The actual Universe is composed of a sum of different components: matter, radiation, and dark energy. The energy densities of these components today, at t_0, are expressed in terms of ratios with respect to the critical density,

$$\Omega_i \equiv \frac{\rho_i(t_0)}{\rho_{\text{crit}}}. \tag{1.9}$$

The current energy budget of the universe, taking $h \sim 0.7$, is

$$\Omega_\Lambda \simeq 70\%, \quad \Omega_m \simeq 5\% + 25\%, \quad \Omega_r \lesssim 10^{-4}, \tag{1.10}$$

where the matter contribution has two components: normal baryonic matter ($\Omega_b \simeq 5\%$) and unknown DM ($\Omega_{DM} \simeq 25\%$). The three components evolve differently with the scale factor; their relative weights in the composition of the Universe change with time. From Fig. 1.1, we can see that matter started dominating the Universe at $R > R_{\text{eq}} = \Omega_r/\Omega_m \simeq 1/3400$, i.e., at matter-radiation equality, at temperature $T_{eq} \sim 0.8$ eV.

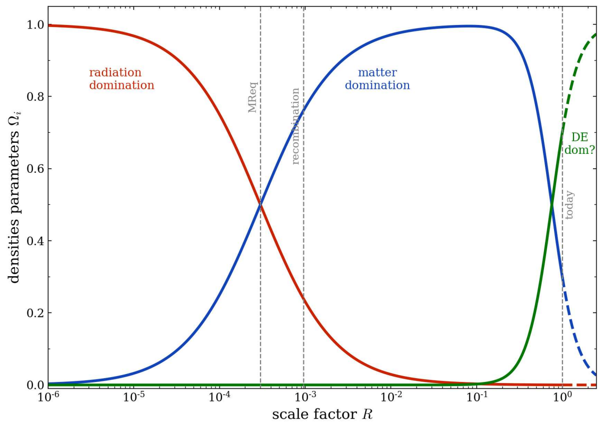

Figure 1.1: Simplified evolutions of the components of the (flat) Universe as a function of the scale factor R. In red, the energy density of radiation, in blue, the matter, and in green, the vacuum energy. Figure adapted from Ref. [20].

Simple analytic results of the Friedmann equations hold for the epochs in which either matter (MD) or radiation (RD) dominated the total energy density,

- During RD at $R \ll R_{\rm eq}$,

$$R(t) \propto \sqrt{t}, \quad H(t) = \frac{1}{2t}. \tag{1.11}$$

- During MD at $R(t_0) > R \gg R_{\rm eq}$,

$$R(t) \propto t^{\frac{2}{3}}, \quad H(t) = \frac{2}{3t}. \tag{1.12}$$

The age of the Universe is given by

$$t_U = \int_0^1 \frac{da}{aH} = \frac{1}{H_0} \cdot \begin{cases} 1/2 \text{ if } \Omega_r = 1 \\ 2/3 \text{ if } \Omega_m = 1 \end{cases} . \tag{1.13}$$

Evidence of DM. The present cosmological DM density, averaged over the whole Universe, is presented in terms of the combination of parameters [21],

$$\Omega_{DM} h^2 = 0.12 \pm 0.01 \ . \tag{1.14}$$

Astrophysical and cosmological observations can be reproduced assuming that DM is a kind of cold, non-interacting, stable matter, with adiabatic inhomogeneities [20],

- *Matter*: its equation of state has a constant parameter $w = 0$.
- *Cold*: DM behaves as a non-relativistic fluid at the crucial time of matter-radiation equality T_{eq}, when structure formation begins.
- *Non-Interacting*: the interactions of DM with itself or between DM and ordinary matter are small enough to be neglected.
- *Stable*: DM is present since the early phase of the Universe and has not disappeared until now.
- *Adiabatic*: on cosmological scales, the composition of the cosmological fluid is the same everywhere.

The evidence of the DM arises at three different scales,

- The Universe would not have acquired the appearance that we observe today if not for the role that DM played: the distribution of galaxies and the Cosmic Microwave Background (CMB) temperature anisotropies cannot be explained with ordinary matter.
- Cluster of galaxies scale. For example, one experimental evidence comes from the observation of a pair of colliding clusters known as the *bullet cluster*. Two clusters of galaxies collided, and visible matter interacts significantly with itself. DM, on the other hand, experienced negligible collisions with itself and with normal matter, such that the DM clouds of the two systems simply passed through each other. Most of the baryonic mass in the bullet cluster is in the form of hot gas whose distribution can be traced through its X-ray emissions. The distribution of the total mass, visible and dark, was independently measured through weak lensing. The results can be seen in Fig. 1.2.

- Galactic scale. In spiral galaxies, the visible mass is concentrated in the central bulge and the disk arms. From Newton's law, the circular velocity $v_{\rm circ}$ of a test particle of mass m is related to the mass M contained within a distance r from the centre, assuming spherical symmetry

$$v_{\rm circ} = \sqrt{\frac{GM(r)}{r}}. \tag{1.15}$$

Observation at a large distance r notes that $v_{\rm circ} \sim$ cost instead of $v_{\rm circ} \propto \sqrt{1/r}$ as expected from Newton's law, as illustrated in Fig. 1.3. This implies that additional mass has to be present.

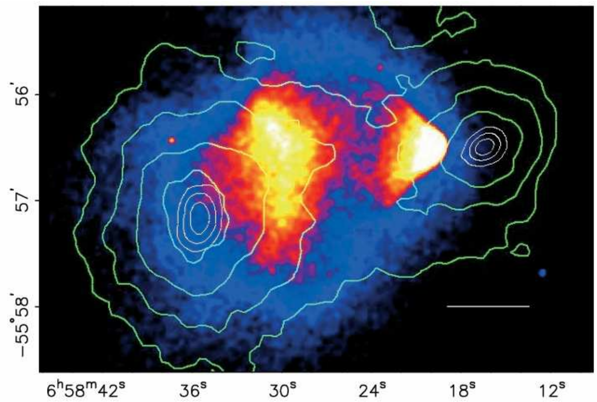

Figure 1.2: *Bullet clusters:* the collision of a pair of clusters of galaxies, with the colored map representing the X-ray image of the hot baryonic gas. The total mass is reconstructed through weak lensing, shown with green contours. The white bar corresponds to the length of 200 kpc. Figure from [22].

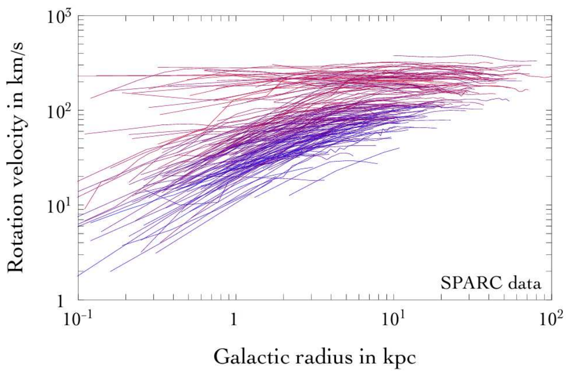

Figure 1.3: The SPARC compilation of 175 galaxies, showing that the rotational velocity from the galactic center tends to be constant at large distances. Figure from [23].

Particles in thermal equilibrium. A particle is in thermal equilibrium if its interaction rate $\Gamma \sim n\sigma$ is faster than the expansion rate of the Universe, i.e., $\Gamma \gg H$. The total energy density of relativistic species in thermal equilibrium of the Universe, which can have different temperatures T_i, is given by

$$\rho_r(T) = \frac{\pi^2}{30} g_*(T) T^4, \quad g_*(T) = \sum_{\text{boson}, m_i \ll T} g_i \left(\frac{T_i}{T}\right)^4 + \frac{7}{8} \sum_{\text{fermion}, m_i \ll T} g_i \left(\frac{T_i}{T}\right)^4, \tag{1.16}$$

where it is understood that T is the temperature of the thermal bath of photons, m_i, g_i the mass and degrees of freedom of the species, and g_* is the effective number of relativistic degrees of freedom of the energy density. The number density of non-relativistic particles in thermal

equilibrium, with $m \gg T$ is exponentially suppressed, $n_{NR}(T) \propto e^{-\frac{m}{T}}$.
Since the Universe cannot exchange heat with any "outside system", its evolution in the thermal equilibrium conserves the entropy, $S = sV$, where V is the volume, and

$$s \equiv \frac{2\pi^2}{45} g_{*s}(T) T^3, \tag{1.17}$$

is the entropy density. The entropy is dominated by the relativistic species. Summing over all the relativistic degrees of freedom,

$$g_{*s}(T) = \sum_{\substack{\text{boson,} \\ m_i \ll T}} g_i \left(\frac{T_i}{T}\right)^3 + \frac{7}{8} \sum_{\substack{\text{fermion,} \\ m_i \ll T}} g_i \left(\frac{T_i}{T}\right)^3. \tag{1.18}$$

Entropy conservation implies that

$$g_{*s}(T) R^3 T^3 = \text{cost}. \tag{1.19}$$

Universe in the past. Based on General Relativity, standard thermodynamics, and the SM, we can extrapolate the thermal history of the Universe at least until temperatures of the order of the weak scale. We briefly recap the particularly important periods that are well known in standard textbooks, i.e. [16, 24]. Going back in time and, accordingly, up in temperature,

- *Recombination, $T \sim 0.3$ eV.* At relatively low temperatures, the usual matter in the Universe was in the state of neutral gas (mainly hydrogen). At an earlier stage, i.e., at higher temperatures, the binding energy was insufficient for keeping electrons in atoms, and the matter was in the state of baryon-electron-photon plasma. Before this epoch, photons actively scattered off electrons in the plasma, while after recombination, the neutral gas was transparent to photons.
- *Big Bang Nucleosynthesis (BBN), $T \sim 1 - 10$ MeV.* At high temperatures, protons and neutrons were free in cosmic plasma, but after the Universe cooled down due to expansion, neutrons were captured into nuclei. As a result, besides hydrogen, there are light nuclei in primordial plasma: mostly helium-4 and also a small amount of deuterium and helium-3. Good agreement between BBN theory and observations is one of the cornerstones of the theory of the Early Universe.
- *Neutrino decoupling, $T \sim$ MeV.* Before that, neutrinos were in thermal equilibrium with the rest of matter, and after that, they freely propagate through the Universe.
- *Cosmological phase transition.* Going further back in time, we come to the epochs that have not been directly probed by observations so far. Hence, we have to make more or less reasonable extrapolations.
  1. Transition from quark-gluon matter to hadronic matter. The energy scale of strong interactions determines its temperature and is about $T \sim 200$ MeV.
  2. Electroweak (EW) transition: at temperatures above 10^2 GeV (energy scale of EW interactions), the Higgs condensate is absent, and the gauge bosons have zero masses. The present phase with broken EW symmetry, Higgs condensate, is the result of the EW transition that occurred at a temperature of order 10^2 GeV.
  3. Other transitions emerge beyond the SM scenario, for example, at the Grand Unification Theory (GUT) or the PQ energy scale. However, the maximum temperature

in the Universe may be below this energy, and this transition never occurred in the Early Universe.

- *Inflation.* Cosmological observations strongly suggest that the Early Universe underwent a phase of rapid accelerated expansion, known as inflation, during which the energy budget was dominated by the potential energy of a scalar field called the *inflaton.* At the end of this phase, the inflaton energy is transferred to SM particles through a process called reheating, resulting in a hot thermal bath characterised by the reheating temperature T_{RH}.

  The duration of inflation is conveniently quantified by the number of e-folds N, defined as the logarithm of the ratio of the scale factor at the end and beginning of the inflationary phase,

$$N \equiv \ln\left(\frac{R_{\text{end}}}{R_{\text{initial}}}\right). \tag{1.20}$$

  For inflation to successfully predict the cosmological observation, one typically requires $N \gtrsim 50$ [16].

1.2 Scalar field cosmology

Although there has been no direct observation of a fundamental scalar particle apart from the Higgs, such particles play an important role in modern particle theories and cosmology. In this section, we will review the non-thermal dynamics of a scalar field, which will be applied both to the axion and radial fields in Chapter 2.

1.2.1 Classical scalar field

The properties of any system in fundamental physics are specified by its action. In the case of a single scalar field, in a generic metric $g_{\mu\nu}$,

$$S = \int d^4x\sqrt{-g}\mathcal{L}_\phi, \tag{1.21}$$

where $\sqrt{-g} \equiv \sqrt{|\det(g_{\mu\nu})|}$. The Lagrangian density, in a mostly plus signature is given by

$$\mathcal{L}_\phi = -\frac{1}{2}g^{\mu\nu}\partial_\mu\phi\partial_\nu\phi - V(\phi). \tag{1.22}$$

The stress-energy tensor is obtained by varying the action with respect to the metric,

$$T_{\mu\nu} = -\frac{2}{\sqrt{-g}}\frac{\delta(\sqrt{-g}\mathcal{L}_\phi)}{\delta g^{\mu\nu}} = \partial_\mu\phi\partial_\nu\phi - g_{\mu\nu}\left[\frac{1}{2}g^{\alpha\beta}\partial_\alpha\phi\partial_\beta\phi + V(\phi)\right]. \tag{1.23}$$

Requiring that the field is the source of a perfect fluid, then isotropy and homogeneity of the FLRW require that at large scale,

$$\phi(t,x) \equiv \phi(t), \tag{1.24}$$

such that $T_{\mu\nu}$ takes the perfect fluid form, with pressure and energy density from Eq. (1.3),

$$\rho_\phi = T_{00} = \frac{1}{2}\dot{\phi}^2 + V(\phi), \quad P_\phi\ \delta^i_j = T^i_j = \left(\frac{1}{2}\dot{\phi}^2 - V(\phi)\right)\delta^i_j. \tag{1.25}$$

The classical equation of motion of the field comes from the variational principle,

$$\frac{\delta S}{\delta\phi} = 0 \Longrightarrow \Box\phi - \frac{\partial V}{\partial\phi} = 0, \tag{1.26}$$

up to a total derivative. The box operator acting on a scalar field can be rewritten, using $\Gamma^{\mu}_{\mu\alpha} = \frac{1}{2} g^{\mu\sigma}\partial_\alpha g_{\mu\sigma}$,

$$\Box\phi \equiv \nabla_\mu \partial^\mu \phi = \frac{1}{\sqrt{-g}} \partial_\mu \left(\sqrt{-g}\ g^{\mu\nu}\partial_\nu\phi\right). \tag{1.27}$$

In the flat FLRW metric (1.1) the homogeneous field equation of motion becomes

$$\ddot{\phi} + 3H\dot{\phi} + V' = 0, \quad ' \equiv \frac{d}{d\phi}. \tag{1.28}$$

1.2.2 Essentials of the misalignment mechanism

The misalignment mechanism assumes that the field is displaced from the minimum of the potential, as one would expect, for example, to arise from quantum fluctuations during inflation. We now show that this initial misalignment can produce non-relativistic DM with large occupation numbers. The classical equation of motion for the homogeneous mode, derived in Eq. (1.28) with a generic polynomial potential, can be rewritten as

$$\ddot{\phi} + 3H\dot{\phi} + M^2(\phi)\phi = 0, \tag{1.29}$$

where we introduce the field-dependent mass term $M(\phi)$. As we will see, producing a non-relativistic condensate requires that the mass is slowly varying $\dot{M}/M^2 \ll 1$. At an initial time t_i during RD, we assume the following initial conditions,

$$\phi(t_i) \equiv \phi_i, \quad \dot{\phi}(t_i) = 0, \quad H(t_i) = \frac{1}{2t_i}. \tag{1.30}$$

With a sufficiently flat potential, the solution of this equation can be separated into two regimes, depending on the value of $H \sim T^2/M_{pl}$:

- In a first epoch, the temperature is high, and thus $H \gg M(\phi)$. The field behaves as an overdamped oscillator and remains frozen at its initial value. This follows from the integral of motion,

$$\frac{1}{R^3}\frac{d}{dt}\left(\dot{\phi}R^3\right) \simeq 0, \tag{1.31}$$

  which implies $\dot{\phi}(t) \simeq \frac{\dot{\phi}(t_i)}{R^3(t)}$, with $\dot{\phi}(t_i) = 0$, one gets $\phi(t) \simeq \phi_i = \text{cost}$.

- At a later time, one has $H \ll M(\phi)$, and the field begins coherent oscillations around the minimum that are faster compared to the cosmological expansion rate. In this regime, the friction term $3H\dot{\phi}$ induces a slow change in the oscillation amplitude. Eq. (1.29) can be solved by writing the scalar field as $\phi(t) = A(t)\cos\left(\int_{t_{\rm match}}^{t} M(\phi(t'))dt'\right)$ and, in the WKB approximation [25–27],

$$A(t) \simeq \phi_{\rm match}\left(\frac{M(\phi_{\rm match})R^3(t_{\rm match})}{M(\phi(t))R^3(t)}\right)^{\frac{1}{2}}. \tag{1.32}$$

  This solution describes fast oscillations whose amplitude decays slowly due to both the expansion of the universe and the time-dependence of M. The self-consistency of the approximation requires

$$\left|\frac{\dot{A}}{MA}\right| = \frac{1}{2}\left[\frac{\dot{M}}{M^2} + \frac{H}{M}\right] \ll 1, \tag{1.33}$$

  confirming that both the mass and the Hubble rate must slowly with respect to the leading frequency M.

The transition between the two regimes is conventionally defined by the matching condition $3H(t_{\rm match}) \simeq M(\phi_{\rm match})$, treated as a sharp boundary. A comparison with numerical solutions for a constant mass $M(\phi) = M$, carried out in Appendix C, shows that the optimal matching occurs at $1.6\, H(t_{\rm match}) \simeq M$. For a temperature-dependent mass, the precise coefficient acquires corrections, but remains of order unity.

In the WKB regime, the averaged energy density and pressure are obtained by averaging over fast oscillations, at leading order from Eqs. (1.25), (1.32),

$$\rho_\phi = \left\langle \frac{\dot{\phi}^2}{2} + \frac{M^2}{2}\phi^2 \right\rangle \simeq \frac{M^2}{2}A^2, \quad p_\phi = \left\langle \frac{\dot{\phi}^2}{2} - \frac{M^2}{2}\phi^2 \right\rangle = \frac{\dot{A}^2}{2}, \tag{1.34}$$

and the field behaves as non-relativistic matter for $t > t_{\rm match}$, using Eq. (1.33),

$$w_\phi = \frac{p_\phi}{\rho_\phi} \simeq \left(\frac{\dot{A}}{MA}\right)^2 \simeq 0. \tag{1.35}$$

It follows from Eq. (1.34) that the energy density in a comoving volume $\rho_\phi R^3$, is not conserved if the scalar mass changes in time. However, the quantity

$$N = \rho_\phi \frac{R^3}{M} = \frac{1}{2} M_{\rm match} R^3_{\rm match} \phi_i^2, \tag{1.36}$$

remains constant and can be interpreted as the comoving number of non-relativistic quanta of mass M.
Using conservation of entropy from Eq. (1.19) and the matching condition in the RD era,

$$g_{*s}(T) T^3 R^3 = \text{cost}, \quad H_{\rm match} = 0.33 \sqrt{g_*(T_{\rm match})} \frac{T^2_{\rm match}}{M_{pl}} = \frac{M_{\rm match}}{3}. \tag{1.37}$$

The present-day energy density can be written parametrically as [28],

$$\rho_\phi(t_0) \simeq 0.17 \ \frac{\rm keV}{\rm cm^3} \cdot \sqrt{\frac{M(t_0)}{\rm eV}} \sqrt{\frac{M(t_0)}{M_{\rm match}}} \left(\frac{\phi_i}{10^{11}{\rm GeV}}\right)^2 \left(\frac{g_*(t_{\rm match})}{3.36}\right)^{\frac{3}{4}} \left(\frac{g_{*s}(t_{\rm match})}{3.91}\right)^{-1}. \tag{1.38}$$

At the onset of oscillations, the produced quanta are semi-relativistic, with characteristic momentum $p \sim H_{\rm match} \ll T_{\rm match}$. Their velocity dispersion at later times is [28],

$$\delta v(t) \sim \frac{H_{\rm match}}{M_{\rm match}} \left(\frac{R_{\rm match}}{R(t)}\right) \ll 1. \tag{1.39}$$

If we define, as customary, the occupation number $\mathcal{N}_{\rm occupation}$ as the ratio between the energy density of scalar particles and the density in a volume associated with their de Broglie wave length $\lambda = \frac{2\pi}{vM}$, for a particle of mass M with distribution $\delta v \ll 1$,

$$\mathcal{N}_{\rm occupation} = \frac{\rho_\phi}{M/\lambda^3} \sim \frac{(2\pi)^3}{\frac{4\pi}{3}} \frac{n_{\phi,0}}{M_0^3 \delta v^3}. \tag{1.40}$$

Using $R_0/R_{\rm match} \sim T_{\rm match}/T_0 \sim \sqrt{M M_{\rm match}}/T_0$, and considering a constant mass $M_0 = M_{\rm match} \equiv M$, this typically leads to very high occupation numbers for each quantum state and light mass,

$$\mathcal{N}_{\rm occupation} \sim 10^{42} \left(\frac{eV}{M}\right)^{\frac{5}{2}}. \tag{1.41}$$

1.2.3 Virial theorem and equation of state

Consider, in general, a scalar potential bounded from below of the form

$$V(\phi) = \frac{\lambda_n}{2n}\phi^{2n}, \quad n \in \mathbb{N}, \tag{1.42}$$

with a dimensionfull coupling $[\lambda_n] = 4 - 2n$.
In this case the effective mass is $M^2(\phi) = \lambda_n \phi^{2n-2}$, and in the regime $H \ll M(\phi)$ the equation of motion for zero mode (1.28), at leading order are the following,

$$\ddot{\phi} + \lambda_n \phi^{2n-1} \simeq 0. \tag{1.43}$$

In this limit, the differential equation is a conservative system, which admits an integral of motion

$$\frac{d}{dt}\left(\frac{\dot{\phi}^2}{2} + V(\phi)\right) \simeq 0. \tag{1.44}$$

The solutions of the Eq. (1.43) are oscillatory functions [29].
Define

$$x \equiv \frac{d}{dt}\left(\frac{1}{2}\dot{\phi}\phi\right), \tag{1.45}$$

averaging over many oscillations,

$$\langle x \rangle = \lim_{T\to\infty}\frac{1}{T}\int_0^T dt\; x(t) = \lim_{T\to\infty}\frac{1}{T}\left(\frac{1}{2}\dot{\phi}\phi\Big|_T - \frac{1}{2}\dot{\phi}\phi\Big|_0\right) \to 0, \tag{1.46}$$

since the boundary term remains finite, because it is an oscillatory function, while $\frac{1}{T} \to 0$ in the limit $T \to \infty$.
Using the equation of motion (1.28) in the regime $M(\phi) \gg H$, the left-hand side at leading order can be expressed as

$$0 = \langle x \rangle = \frac{1}{2}\langle \ddot{\phi}\phi + \dot{\phi}^2 \rangle \simeq \left\langle \frac{1}{2}\dot{\phi}^2 \right\rangle - \frac{2n}{2}\left\langle \frac{\lambda_n}{2n}\phi^{2n} \right\rangle = \langle \text{Kin} \rangle - n\langle \text{Pot} \rangle \Longleftrightarrow \langle \text{Kin} \rangle = n\langle \text{Pot} \rangle, \tag{1.47}$$

which is precisely the virial theorem for a generic ϕ^n theory in the oscillatory regime. The corresponding equation of state is

$$w_\phi = \frac{\langle \text{Kin} \rangle - \langle \text{Pot} \rangle}{\langle \text{Kin} \rangle + \langle \text{Pot} \rangle} \simeq \frac{n-1}{n+1}. \tag{1.48}$$

In the WKB approximation, the mass term is nearly constant. So, at leading order $n = 1$, and it behaves approximately as a non-relativistic matter, as proved in Eq. (1.35). While for a quartic theory, $V = \lambda\phi^4$, we get $w_\phi = 1/3$, the equation of state of a relativistic fluid.

1.3 Basics of QCD axion cosmology

In this section, we will review the theoretical basics of the QCD axion and its impact on cosmology. We will be based on Refs. [30, 31].

1.3.1 The QCD axion

QCD suffers from the "strong-CP problem". A topological term is allowed in the Lagrangian:

$$\mathcal{L}_{\theta QCD} = \frac{\theta_{QCD}}{32\pi^2}\tilde{G}G, \tag{1.49}$$

where $G_{\mu\nu}$ is the gluon field strength tensor, and $\tilde{G}_{\mu\nu} = \epsilon_{\mu\nu\alpha\beta}G^{\alpha\beta}/2$ is its dual. This term arises due to the so-called "θ-vacua" of QCD [32].
Specifically, the measurable quantity is

$$\bar{\theta}_{QCD} = \theta_{QCD} + \arg\det M_u M_d\,, \tag{1.50}$$

where M_u, M_d are the quark mass matrices. The θ term is CP violating and gives rise to an electric dipole moment (EDM) for the neutron [33]:

$$d_n \approx 3.6\times 10^{-16}\,\bar{\theta}_{QCD}\,e\;\mathrm{cm}\,, \tag{1.51}$$

where e is the charge on the electron. The (permanent, static) dipole moment is constrained to $|d_n| < 2.9\times 10^{-26}\,e\,\mathrm{cm}$ (90% C.L.) [34], implying $\bar{\theta}_{QCD} \lesssim 10^{-10}$. This is a true fine-tuning problem, since θ_{QCD} could obtain an $\mathcal{O}(1)$ contribution from the observed CP-violation in the EW sector.

From a modern perspective, the basic ingredient of the PQ solution [1–4] of the strong CP problem consists in the introduction of a new spin-zero field $a(x)$, denoted by the axion field, whose effective Lagrangian

$$\mathcal{L}_a = \frac{1}{2}(\partial a)^2 + \mathcal{L}(\partial a, \psi) + \frac{g_s^2}{32\pi^2}\frac{a}{f_a}G\tilde{G} \tag{1.52}$$

is endowed with a quasi shift symmetry $a \to a + \kappa f_a$, where f_a is an energy scale called the axion decay constant, that leaves the action invariant up to the term

$$\delta S = \frac{g_s^2\kappa}{32\pi^2}\int d^4x\; G\tilde{G}. \tag{1.53}$$

The transformation parameter κ is arbitrary and can be chosen to remove the $\bar{\theta}$ term, while the Vafa-Witten theorem [35] ensures that $\langle a\rangle = 0$ in a vector-like theory like QCD, thus solving the strong CP problem dynamically.
The axion mass m_a, induced by QCD instantons, can be calculated in chiral perturbation theory [1, 2]. It is given by

$$m_a \simeq 6\cdot 10^{-6}\;\mathrm{eV}\frac{10^{12}\;\mathrm{GeV}}{f_a}. \tag{1.54}$$

This is a model-independent statement. If f_a is large, the QCD axion can be extremely light and stable, thus an excellent candidate for DM [5, 7, 36]. Bounds on f_a arise from a variety of sources; of particular interest, supernova cooling provides a lower limit [37], while black hole superradiance provides an upper limit [38]. Combined, they constrain the axion decay constant in the range

$$10^8\;\mathrm{GeV} \lesssim f_a \lesssim 6\cdot 10^{17}\;\mathrm{GeV}, \tag{1.55}$$

where the lower bound is affected by many uncertainties. This translates into the following axion mass range,

$$10^{-11}\;\mathrm{eV} \lesssim m_a \lesssim\; 10^{-1}\mathrm{eV}. \tag{1.56}$$

UV completions of the effective Lagrangian axion can be divided into two large classes, according to the way the QCD anomaly of the $U(1)_{PQ}$ current is realised. We will review the simpler model of each.

KSVZ axion. The KSVZ model [39, 40] extends the SM field content with a vector-like fermion $\mathcal{Q} = \mathcal{Q}_L + \mathcal{Q}_R$ in the fundamental of colour, singlet under $SU(2)_L$, neutral under hypercharge, $\mathcal{Q} \sim (3, 1, 0)$, and a SM-singlet complex scalar $\Phi \sim (1, 1, 0)$. In the absence of a bare mass term for $\mathcal{Q}$, the Lagrangian

$$\mathcal{L}_{\text{KSVZ}} = |\partial_\mu \Phi|^2 + \bar{\mathcal{Q}} i \not{D} \mathcal{Q} - \left(y_{\mathcal{Q}} \bar{\mathcal{Q}}_L \mathcal{Q}_R \Phi + \text{h.c.} \right) - V(\Phi) \,, \tag{1.57}$$

features a $U(1)_{PQ}$ symmetry

$$\Phi \to e^{i\alpha} \Phi \,, \quad \mathcal{Q}_L \to e^{i\alpha/2} \mathcal{Q}_L \,, \quad \mathcal{Q}_R \to e^{-i\alpha/2} \mathcal{Q}_R \,. \tag{1.58}$$

The potential

$$V(\Phi) = \lambda_{PQ} \left(|\Phi|^2 - \frac{f_a^2}{2} \right)^2 \,, \tag{1.59}$$

is such that the $U(1)_{PQ}$ symmetry is spontaneously broken, with order parameter f_a. Decomposing the scalar field in polar coordinates

$$\Phi = \frac{1}{\sqrt{2}} (f_a + \chi) e^{i \frac{a}{f_a}} \,, \tag{1.60}$$

the axion field a corresponds to the angular mode (massless at tree level), while the radial mode χ picks up a mass $m_\chi = \sqrt{2\lambda_{PQ}} f_a$. In the PQ broken phase also the fermion $\mathcal{Q}$ gets massive, with $m_{\mathcal{Q}} = y_{\mathcal{Q}} f_a / \sqrt{2}$.

The Lagrangian term (where we neglected the heavy scalar radial mode)

$$\mathcal{L}_{\text{KSVZ}} \supset -m_{\mathcal{Q}} \bar{\mathcal{Q}}_L \mathcal{Q}_R e^{ia/v_a} + \text{h.c.} \,, \tag{1.61}$$

is responsible for the generation of the $aG\tilde{G}$ operator in the effective theory below $m_{\mathcal{Q}}$ [30].

DFSZ axion. The field content of the DFSZ model includes two Higgs doublets $H_u \sim (1, 2, -\frac{1}{2})$ and $H_d \sim (1, 2, +\frac{1}{2})$ and a SM-singlet complex scalar field, $\Phi \sim (1, 1, 0)$. Again, a global $U(1)_{PQ}$ symmetry is imposed and spontaneously broken by the potential in Eq. (1.59). The PQ and Higgs fields interact via the scalar potential:

$$V = \lambda_H \Phi^2 H_u H_d + h.c. \,. \tag{1.62}$$

This term is PQ invariant for Φ with $U(1)_{\text{PQ}}$ charge $+1$, and the Higgs fields each with charge -1. When the PQ symmetry is broken and Φ obtains a vev, the parameters in the Higgs potential, and the coupling constant, λ_H, must be chosen such that the Higgs fields remain light, consistent with the observed 125 GeV SM Higgs, and the EW vev, $v = \sqrt{\langle H_u \rangle^2 + \langle H_d \rangle^2}$.

The Higgs must also couple to all SM fermions, providing their mass through Yukawa terms as usual, e.g.

$$\mathcal{L}_Y \supset \lambda_u \bar{q}_L u_R H_u \,. \tag{1.63}$$

In order for this to be PQ invariant, the SM fermions must be charged under $U(1)_{\text{PQ}}$. After EW symmetry breaking, H is replaced by its vev, inducing axial current couplings between the axion and SM fermions from the chiral term in the fermion mass matrix: $m_u(\phi/f_a) i\bar{u}\gamma_5 u$. This axial current in turn induces the coupling between the axion and $G\tilde{G}$ via the colour anomaly.

1.3.2 Axion cosmology

The cosmological history of the QCD axion is shaped by two key physical events. The first is the spontaneous breaking of the PQ symmetry at the large scale f_a, which gives rise to the axion as the associated Goldstone boson. The axion field is identified with the angular degree of freedom of a complex scalar,

$$\Phi = \frac{\chi + f_a}{\sqrt{2}}\, e^{i\frac{a}{f_a}}\,, \tag{1.64}$$

where the radial mode χ is usually taken heavy and decouples from the low-energy dynamics. The second key event occurs much later, when non-perturbative QCD effects switch on at a temperature $T_{\rm NP} \ll f_a$ and generate a potential for the otherwise massless axion.

The axion field during inflation. Whether the PQ symmetry is broken or unbroken during inflation depends on how f_a compares to the Hubble scale H_I, and the two cases lead to different cosmological histories for the axion field.

- *Post-inflationary scenario ($f_a < H_I$).* Here, the PQ symmetry remains unbroken throughout inflation and only breaks afterwards, once the radiation temperature drops below f_a. At that point Φ acquires a vacuum expectation value, and each causally disconnected Hubble patch independently selects its own value of the misalignment angle $\theta = a/f_a$. The result is a present-day Universe stitched together from many regions with independently random initial misalignment angles θ_i. In this scenario, the domain walls and axionic strings play an important role. Stable domain walls would be cosmologically catastrophic, but the decay of axion strings instead provides a genuine source of relic axions.

  After the end of inflation, the initial misalignment angle θ_i, within a Hubble patch, takes all possible values on the unit circle. For determine the energy density, for a quadratic potential, this is the same as assuming for the initial condition the value

  $$\theta_i \equiv \sqrt{\langle \theta_i^2 \rangle} = \frac{\pi}{\sqrt{3}}. \tag{1.65}$$

  where the angle brackets represent the value of the initial condition averaged over $[-\pi, \pi)$.

- *Pre-inflationary scenario, $f_a > H_I$.* The PQ symmetry is broken during inflation. As in the previous scenario, PQ symmetry breaking establishes causally disconnected patches with different values of θ, and produces topological defects. However, the rapid expansion during inflation dilutes all the phase transition relics. It also stretches out each patch of θ, so that our current Hubble volume began life at the end of inflation with a single uniform value of θ everywhere. This initial value θ_i is drawn from a uniform distribution. However, other bounds that come from isocurvature modes [41] constrain this scenario, which requires a relatively low-energy scale of inflation to be viable.

Misalignment production of axion DM. How the axion potential and mass evolve with the temperature of the thermal bath is central to predicting the relic abundance generated by the misalignment mechanism. In QCD, this temperature dependence is encoded in

$$m_a^2(T) f_a^2 = \zeta_{\rm top.}(T)\,, \tag{1.66}$$

where $\zeta_{\text{top.}}(T)$ is the QCD topological susceptibility. At temperature higher than the QCD deconfining scale, $T \gg \Lambda_{QCD} \sim 160$ MeV, this reduces to a simple power law [42],

$$m_a^2(T) \simeq 10^{-7}\,\frac{\Lambda_{\text{QCD}}^3\, m_a}{f_a^2}\left(\frac{T}{\Lambda_{\text{QCD}}}\right)^{-8}, \tag{1.67}$$

which must be matched onto the zero-temperature value, Eq. (1.54), once $T \lesssim \Lambda_{\text{QCD}}$.

This temperature-dependent mass feeds directly into the axion equation of motion. Treating $a(t)$ as spatially homogeneous, the equation of motion for the misalignment angle $\theta = a/f_a$ reads, at the leading order,

$$\ddot{\theta} + 3H(T)\,\dot{\theta} + m_a^2(T)\,\theta = 0\,. \tag{1.68}$$

The behaviour of this equation was already discussed in Section 1.2.2; the only new ingredient here is the explicit temperature dependence of the mass term. A fully detailed treatment can be found in Ref. [30]. Solving Eq. (1.68) and tracking the resulting energy density until today, it gives the present axion abundance from misalignment, normalized to the critical density ρ_{crit}, in terms of the initial misalignment angle,

$$\Omega_a^{\text{mis}} h^2 \approx 0.12 \cdot \left(\frac{F(\theta_i)}{\pi/\sqrt{3}}\right)^2 \left(\frac{f_a}{2\times 10^{11}\ \text{GeV}}\right)^{7/6}, \tag{1.69}$$

where $F(\theta_i) = \theta_i$ in the pre-inflationary scenario, and $F(\theta_i) = \pi/\sqrt{3}$ in the post-inflationary case, from Eq. (1.65).

Cosmic axion strings. As predicted by the Kibble mechanism [43], when the PQ symmetry is broken after inflation, cosmic strings are produced. Domain walls form between these strings around the QCD phase transition and, if the domain wall number is unity, the string-domain wall network is unstable and decays into axions [8], yielding a matter density [8, 9]

$$\Omega_a h^2\Big|_{\text{string-DW}} \simeq 0.04 - 0.3\left(\frac{f_a}{10^{11}\text{GeV}}\right)^{\frac{7}{6}}. \tag{1.70}$$

These mechanisms most naturally lead to axion DM for $f_a \sim (10^{11} - 10^{12})$ GeV, and the misalignment mechanism could also yield DM for larger f_a as θ_i is reduced.

Chapter 2

The radial mode as cold dark matter

A recent analysis [11] showed that, for sufficiently large initial values of the PQ field, the subsequent cosmological evolution efficiently excites a population of axion and radial mode fluctuations through parametric resonance. This mechanism allows the axion population to account for the total DM abundance, for a viable range of decay constant $f_a \sim (10^8 - 10^{12})$ GeV, with a light radial mode $m_\chi \sim$ GeV.

In this chapter, we generalise the results of [11] and show that the radial mode can be produced in a larger abundance, so it may indeed be a more natural candidate for DM than the axion in the parametric resonance mechanism. In addition, we study the production of radial mode DM via the misalignment mechanism. We further discuss how large initial displacements of the PQ field may arise and explore their cosmological implications. Our results reveal sizable regions of parameter space in which the radial mode accounts for a fraction of the observed DM abundance, with viable decay constant spanning $f_a \sim (10^8 - 10^{17})$ GeV depending on the production mechanism considered, and a sufficiently light radial mode.

2.1 The model

We will work with an SM field content that is neutral under the new global $U(1)_{PQ}$ symmetry. Since, in our scenario, radial mode DM is realised non-thermally via a new degree of freedom, the radial mode weakly interacts with the SM fields. This allows us to treat the dark sector effectively as isolated without affecting the main results. We will address the self-consistency of this assumption in Chapter 3, where we specify how the SM communicates with the radial mode.

We start with a simple realisation of the SSB of the $U(1)_{PQ}$ symmetry,

$$\mathcal{L} = -\left(\partial_\mu \Phi\right)^\dagger \left(\partial^\mu \Phi\right) - V(\Phi), \quad V(\Phi) = \lambda_{PQ} \left(|\Phi|^2 - \frac{f_a^2}{2} \right)^2, \tag{2.1}$$

where $\lambda_{PQ} > 0$ for a potential bounded from below. The field Φ is a complex scalar, a singlet under the SM gauge group, $\Phi \sim (1,1,0)_{SM}$, charged under the global $U(1)_{PQ}$ symmetry with charge Q_Φ. In particular, the field acquires a VEV at the energy scale f_a,

$$\langle \Phi^\dagger \Phi \rangle = \frac{f_a^2}{2}. \tag{2.2}$$

Using the polar parametrisation,

$$\Phi = \left(\frac{\chi + f_a}{\sqrt{2}} \right) e^{i \frac{a}{f_a}}, \tag{2.3}$$

the complex scalar field is decomposed into two real degrees of freedom with a clear interpretation, and the mass spectrum of the theory is organised as follows.

Radial mode χ: a scalar field with mass given by the scale of spontaneous symmetry breaking $m_\chi = \sqrt{2\lambda_{PQ}} f_a$.

Angular mode a: is the (p)NGB called the axion, a pseudoscalar that transforms under the original $U(1)_{PQ}$ via a constant shift.

As explained in Section 1.3, in the QCD axion scenario, the $U(1)_{PQ}$ is anomalous, so that the shift symmetry of the axion a is broken by quantum corrections, and generates a mass term for the angular mode.
To obtain a radial mode that is parametrically lighter than the PQ scale, we will work in the regime of small quartic coupling, $\lambda_{PQ} \ll 1$.

2.2 Non-thermal production mechanism in the Early Universe

We will use two non-thermal mechanisms to produce a population of radial mode χ in the Early Universe. Both require an initial displacement from the minimum of the potential of the homogeneous mode at cosmic time t_i, $\chi(t_i) \equiv \chi_i$, in RD, but with different magnitudes:

Misalignment mechanism: requires a small initial displacement from the VEV, $\chi_i \ll f_a$.

Parametric resonance mechanism: requires a large initial displacement from the VEV, $\chi_i \gg f_a$.

In both cases, we assume a RD epoch until BBN, after which we follow the standard cosmological evolution. Before analysing each mechanism in detail, we first discuss how such an initial displacement may arise naturally in the Early Universe. We will further assume a pre-inflationary scenario, described in Section 1.3.

2.3 Initial condition realization

During inflation, light spectator scalar fields are subject to stochastic fluctuations sourced by the quasi–de Sitter background, with constant Hubble rate $H(t) \simeq H_I$. As emphasised in [44, 45], the super-horizon modes of such a field undergo a random walk, leading to a probability distribution with potentially large variance.
In the pre-inflationary scenario, inflation selects one patch of the Universe within which the spontaneous breaking of the PQ symmetry leads to a homogeneous value of the initial displacement χ_i, drawn from this distribution.
Throughout this discussion, we assume that the radial field is completely decoupled from the inflaton and never thermalises with the SM plasma. Its dynamics during inflation are therefore governed solely by its classical potential, encoded in the effective mass

$$m_\chi^2(\chi) \equiv V''(\chi). \tag{2.4}$$

In the two regimes relevant for our analysis,

$$\begin{cases} m_\chi^2(\chi) \sim m_\chi^2 \quad \text{if} \quad \chi \ll f_a, \\ m_\chi^2(\chi) \sim 3\lambda_{PQ}\chi^2 \quad \text{if} \quad \chi \gg f_a, \end{cases} \tag{2.5}$$

with m_χ^2 the vacuum mass.

Initial condition for the misalignment mechanism. In the small-field regime $\chi \ll f_a$, the equation of motion is reduced to

$$\Box\chi = m_\chi^2 \chi, \quad m_\chi = \sqrt{2\lambda_{PQ}} f_a, \tag{2.6}$$

where the radial field behaves as a free massive scalar. To generate an unsuppressed variance during inflation, we require the light mass regime,

$$m_\chi^2 \ll H_I^2. \tag{2.7}$$

Otherwise, for $m_\chi \gg H_I$ the field rapidly relaxes to the minimum of its potential and does not develop a significant variance. In this regime, the stochastic dynamics yield a gaussian distribution with zero mean and variance, as discussed in Appendix B,

$$\langle\chi^2\rangle_e \simeq \frac{3}{8\pi^2}\left(\frac{H_I^4}{m_\chi^2}\right)\left[1 - e^{-N\frac{2m_\chi^2}{3H_I^2}}\right], \tag{2.8}$$

with N the number of e-folds during inflation, defined in Eq. (1.20). If the inflation lasts long enough, the variance will reach an equilibrium configuration, $\langle\chi^2\rangle_e \simeq \frac{3}{8\pi^2}\left(\frac{H_I^4}{m_\chi^2}\right)$ for $N \gg \frac{H_I^2}{m_\chi^2}$. In the light-mass regime, it is natural to assume that equilibrium is not reached. For example, with $H_I \sim 10^{13}$ GeV and $m_\chi \sim$ GeV, realising axion DM from parametric resonance [11], reaching the equilibrium requires $N \sim 10^{26}$, which is a very large number of e-folds that need a very specific inflationary model. Expanding the exponential for

$$N \ll \frac{3H_I^2}{2m_\chi^2}, \tag{2.9}$$

one obtains the variance at the end of inflation,

$$\langle\chi^2\rangle_e \simeq N\left(\frac{H_I}{2\pi}\right)^2\left[1 - N\frac{m_\chi^2}{3H_I^2} + \mathcal{O}\left(N\frac{m_\chi^2}{H_I^2}\right)\right]. \tag{2.10}$$

The regime of validity requires that the initial displacement remains small,

$$\langle\chi^2\rangle_e \ll f_a^2. \tag{2.11}$$

Taking the benchmark value $N \approx 10^2$, this yields an upper bound on the inflationary scale as a function of f_a, while the validity of the assumption in Eq. (2.7) gives the lower bound,

$$m_\chi \ll H_I \ll 6 \cdot 10^{11}\ \text{GeV}\ \frac{f_a}{10^{12}\ \text{GeV}}. \tag{2.12}$$

In Fig. 2.1, we can see that for $f_a < 10^{15}$ GeV the upper bound is stronger than the current CMB bound,

$$H_I^{\text{exp}} \lesssim 10^{14}\ \text{GeV}\left(\frac{r}{0.01}\right)^{\frac{1}{2}}, \tag{2.13}$$

where the present bound on the tensor-to-scalar perturbation ratio from inflation is $r < 0.036$, from CMB anisotropies [46]. Since the radial masses of interest lie below the GeV scale, the lower bound is extremely mild.

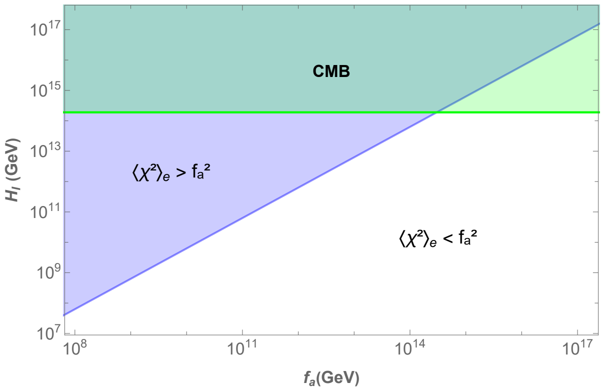

Figure 2.1: Parameter space of the inflationary Hubble scale, H_I, to realise a small kick of the radial mode from the vacuum $\langle\chi^2\rangle_e \ll f_a$. Considering the regime in which $\langle\chi^2\rangle_e$ does not reach the equilibrium configuration at the end of inflation, assuming $N \sim 10^2$, the blue region is excluded, since $\langle\chi^2\rangle_e \gg f_a^2$ contradicts the assumptions underlying the analysis. The green region is ruled out by constraints from the CMB anisotropies, which fix the experimental upper bound $H_I < 10^{14}$GeV. [46]

.

Initial condition for the parametric resonance. To realise the parametric resonance mechanism, we need a large displacement from the true vacuum. In the $\frac{\chi}{f_a} \gg 1$ regime, the potential is approximately quartic,

$$V(\chi) \simeq \frac{\lambda_{PQ}}{4}\chi^4, \tag{2.14}$$

and the wave equation for the scalar field in this regime is at leading order

$$\Box\chi \simeq \lambda_{PQ}\chi^3. \tag{2.15}$$

In this regime, the Hartree–Fock approximation is unreliable due to self-interactions, but the stochastic formalism still applies. Effectively, due to scattering, the field acquires an effective mass term $m_{\text{eff}}^2 \sim H^2\sqrt{\lambda}$. The variance reaches the equilibrium value, as discussed in [45] and derived in Appendix B,

$$\langle\chi^2\rangle_e = \sqrt{\frac{3}{2\pi^2}}\frac{\Gamma\left(\frac{3}{4}\right)}{\Gamma\left(\frac{1}{4}\right)}\frac{H_I^2}{\sqrt{\lambda_{PQ}}} \simeq 10^{-1}\frac{H_I^2}{\sqrt{\lambda_{PQ}}}. \tag{2.16}$$

Using the vacuum mass relation and requiring that $\langle\chi^2\rangle_e \gg f_a^2$, the range of validity on the inflationary scale requires

$$H_I > 10^2\text{GeV} \cdot \left(\frac{m_\chi}{\text{eV}}\right)^{1/2}\left(\frac{f_a}{10^{12}\text{GeV}}\right)^{1/2}. \tag{2.17}$$

As in the misalignment scenario, reaching this equilibrium configuration will require $N \gg f_a/m_\chi > 10^8$.

Instead, for $N \ll \frac{1}{\sqrt{\lambda_{PQ}}}$ the system is in the non-equilibrium regime, and following the evolution will require a detailed numerical simulation. However, we can use a simpler argument to make the point. In the first approximation, the minimum number of e-folds needed to reach $\langle\chi^2\rangle \sim f_a^2$ can be roughly calculated using Eq. the Hartree-Fock approximation, from Eq. (2.10),

$$N \gtrsim 4\pi^2\left(\frac{f_a}{H_I}\right)^2. \tag{2.18}$$

Thus, while inflation can, in principle, generate the large initial displacement required for parametric resonance, doing so necessitates an exceptionally long inflationary epoch in a pre-inflationary scenario, an aspect that is not emphasised in the Co et al. paper [11].

2.4 Radial mode DM from misalignment mechanism

To realise a DM relic, the radial field must behave as a homogeneous perfect fluid on cosmological scales, in accordance with the Cosmological Principle. As discussed above, to avoid non-linear effects, we need a small initial displacement of the radial field from the minimum of the potential, so the working assumption is $\frac{\chi}{f_a} \ll 1$ in this section.
The radial field can be decomposed into a homogeneous mode and fluctuations,

$$\chi(t,x) = \chi_0(t) + \delta\chi(t,x), \tag{2.19}$$

where the homogeneous mode is the classical field $\langle \chi(t,x) \rangle \equiv \chi_0(t)$. As long as $\langle \delta\chi^2 \rangle \ll \chi_0^2(t)$, the fluctuations can be neglected, and the dynamics of the homogeneous mode fully capture the relevant physics for DM production.

2.4.1 Classical EOM

The action in polar field coordinates, in a general background metric with mostly-plus signature $g_{\mu\nu}$,

$$S = \int d^4x\sqrt{-g}\left[-\frac{1}{2}\nabla_\mu\chi\nabla^\mu\chi - \frac{1}{2}\left(1+\frac{\chi}{f_a}\right)^2\nabla_\mu a\nabla^\mu a - \frac{\lambda_{PQ}}{4}(\chi^2+2\chi f_a)^2\right], \tag{2.20}$$

where $\sqrt{-g} \equiv \sqrt{-\det(g_{\mu\nu})}$. The classical EOM follows from the Principle of Least Action, leading to a set of coupled differential equations,

$$\delta S = 0 \implies \begin{cases} \nabla_\mu\left(\left(1+\frac{\chi}{f_a}\right)^2\nabla^\mu a\right) = 0, \\ \nabla_\mu\nabla^\mu\chi - \left(1+\frac{\chi}{f_a}\right)\frac{\nabla_\mu a\nabla^\mu a}{f_a} - 2\lambda_{PQ}f_a^2\,\chi\left(1+\frac{\chi^2}{2f_a^2}+\frac{3}{2f_a}\chi\right) = 0. \end{cases} \tag{2.21}$$

In this regime, the homogeneous mode of both fields dominates the dynamics. At leading order in $\frac{\chi}{f_a}$, the axion zero mode equation reduces to that of a free massless scalar,

$$\ddot{a}_0 + 3H\dot{a}_0 = 0 + \mathcal{O}\left(\frac{\chi}{f_a}\right), \tag{2.22}$$

which has two different solutions, depending on the Cauchy conditions, for $t > t_i$,

$$\dot{a}_0(t_i) = 0 \to a_0(t) = a_0(t_i), \tag{2.23}$$

$$\dot{a}_0(t_i) \neq 0 \to a_0(t) = a_0(t_i) + C\int_{t_i}^{t} e^{-\int_{t_i}^{t'} 3H(\tilde{t})d\tilde{t}}dt'. \tag{2.24}$$

We choose the maximally symmetric vacuum state, that is, the constant solution,

$$\langle a(t,\vec{x}) \rangle \equiv a_0(t) = \text{const} \to \nabla^\mu a_0(t) = \partial^\mu a_0(t) = 0, \tag{2.25}$$

where, in the last equation, we have exploited the fact that $a(t,x)$ is a scalar field. An interesting possibility, explored in Ref. [47], is that the axion field begins with a non-zero initial

velocity, $\dot{a}(t_i) \neq 0$.
In this regime, we can treat the axion dynamics as decoupled from the radial evolution. This is consistent even in a realistic QCD-axion scenario, where the axion acquires a temperature-dependent mass from quantum effects. The axion mass m_a enters the radial EOM only at order $\frac{m_a^2}{f_a}$, so that we can treat them independently.

Expanding the radial equation to linear order in $\frac{\chi}{f_a}$, and renaming $\chi_0(t) \equiv \chi(t)$ for simplicity from now on, the standard Klein–Gordon equation in Eq. (1.28) is the following,

$$\ddot{\chi} + 3H\dot{\chi} + m_\chi^2 \chi \simeq 0, \tag{2.26}$$

with vacuum mass $m_\chi^2 = 2\lambda_{PQ} f_a^2$.
During RD, $H(t) = \frac{1}{2t}$, and the solution is fixed by the initial conditions at cosmic time t_i,

$$\chi(t_i) \equiv \chi_i, \quad \dot{\chi}(t_i) \equiv 0. \tag{2.27}$$

As discussed in Section 1.2.2, once the Hubble rate H drops below $H_{\rm osc}$ defined by $3H(T_{\rm osc}) = m_\chi$, the field begins coherent oscillations around the minimum of its potential. Averaged over many oscillations, the radial condensate behaves as non-relativistic matter, as derived by the virial theorem for a quadratic potential (1.47). In this oscillatory regime with constant mass term, the energy density at a temperature $T \leq T_{\rm osc}$ redshifts as,

$$\rho_\chi(T) \simeq \rho_{osc} \left(\frac{R(T_{\rm osc})}{R(T)}\right)^3 = \rho_{osc} \left(\frac{T}{T_{\rm osc}}\right)^3 \frac{g_{*s}(T)}{g_{*s}(T_{\rm osc})} \overset{(a)}{=} \frac{1}{2} m_\chi^2 \chi_i^2 \left(\frac{T}{T_{\rm osc}}\right)^3 \frac{g_{*s}(T)}{g_{*s}(T_{\rm osc})}. \tag{2.28}$$

where in (a) we have used the matching condition $\rho_{\rm osc} = \frac{1}{2} m_\chi^2 \chi_i^2$, and $g_{*s}(T)$ is the number of effective degrees of freedom.
This expression determines the abundance of the radial mode relic in terms of the initial displacement χ_i, the mass of the radial mode m_χ, and constitutes the radial mode DM relic of the standard misalignment mechanism.

2.4.2 Energy abundance of the radial condensate $\Omega_\chi^{\rm mis}$

The present cosmological DM energy density from the radial condensate through the misalignment mechanism is encoded in the parameters $\Omega_\chi^{\rm mis} h^2$ where $\Omega_\chi^{\rm mis} \equiv \frac{\rho_\chi(T_0)}{\rho_{\rm crit}}$ is the radial energy density today relative to the critical density.
Recall that the starting point of the onset oscillations is determined by $\frac{m_\chi}{3} \sim H_{\rm osc} = 0.3\sqrt{g_*(T_{\rm osc})}\frac{T_{\rm osc}^2}{M_{\rm pl}}$.
The present radial abundance can be expressed as a function of m_χ and χ_i,

$$\Omega_\chi^{\rm mis} \equiv \frac{\rho_\chi(T_0)}{\rho_{\rm crit}} \sim \frac{1}{2} m_\chi^{\frac{1}{2}} \chi_i^2 \frac{T_0^3}{\rho_{\rm crit} M_{\rm pl}^{\frac{3}{2}}} \frac{g_{*s}(T_0)}{g_{*s}(T_{\rm osc})} g_*^{\frac{3}{4}}(T_{\rm osc}). \tag{2.29}$$

To further simplify this expression, we adopt the following assumptions:

- Assume $T_{\rm osc} >$ MeV, i.e., oscillations begin before $e^+e^- \to \gamma\gamma$ annihilation in the thermal bath, which translates into $m_\chi > 10^{-15}$eV. We can therefore take $\frac{g_*^{\frac{3}{4}}(T_{\rm osc})}{g_{*s}(T_{\rm osc})} = \frac{1}{g_{*s}(T_{\rm osc})^{\frac{1}{4}}}$.
- Taking three relativistic neutrino species gives $g_{*s}(T_0) \sim 3.91$

Using the numerical values $T_0 = 2.35 \cdot 10^{-13}$ GeV, $M_{\rm pl} = 2.4 \cdot 10^{18}$ GeV, $\rho_{\rm crit} = 4.7 \cdot 10^{-47}$ GeV^4, $h = 0.7$, the present-day radial abundance can be written as

$$\Omega_\chi^{\rm mis} h^2 = 0.12 \cdot \left(\frac{4 \cdot \chi_i}{10^{12}{\rm GeV}}\right)^2 \left(\frac{m_\chi}{\rm eV}\right)^{\frac{1}{2}} \frac{1}{g_{*s}^{1/4}(T_{\rm osc})}. \tag{2.30}$$

This expression can be inverted to give a relation between the radial mass and its initial displacement,

$$\chi_i = 2.5 \cdot 10^{11}\ {\rm GeV} \left(\frac{\Omega_\chi^{\rm mis} h^2}{0.12}\right)^{\frac{1}{2}} \left(\frac{\rm eV}{m_\chi}\right)^{\frac{1}{4}} g_{*s}^{1/8}(T_{\rm osc}) \simeq 4.5\ \cdot 10^{11}\ {\rm GeV} \left(\frac{\Omega_\chi^{\rm mis} h^2}{0.12}\right)^{\frac{1}{2}} \left(\frac{\rm eV}{m_\chi}\right)^{\frac{1}{4}}, \tag{2.31}$$

where in the last step, we used $g_{*s}(T_{\rm osc}) \sim 10^2$. This assumption is verified a posteriori: from the parameter space in Fig. 2.3, $m_\chi > 10^{-9}$ eV implies $T_{\rm osc} >$ GeV.
So for the radial condensate to be a candidate for DM today, there is a one-to-one correspondence between the initial value χ_i and the mass m_χ.

2.4.3 Constraints

$m_\chi > m_a$. Although in this work we allow for a broad range of possible radial masses, having a radial mode lighter than the angular mode may significantly alter the scenario, depending on the underlying model. To remain conservative, we impose

$$m_\chi > m_a. \tag{2.32}$$

Applying this bound to the QCD axion case and using the standard QCD axion mass relation in Eq. (1.54), with the DM abundance relation in Eq. (2.31), this translates into,

$$\chi_i < 8 \cdot 10^{12}\ {\rm GeV} \left(\frac{\Omega_\chi^{\rm mis} h^2}{0.125}\right)^{\frac{1}{2}} \left(\frac{f_a}{10^{12}{\rm GeV}}\right)^{\frac{1}{4}}. \tag{2.33}$$

Survival of the condensate. If the radial condensate constitutes DM today, it must remain sufficiently long-lived throughout cosmic history. In the Lagrangian (2.1), the only decay channel is the process $\chi \to aa$, which arises from the kinetic term in polar coordinates,

$$\mathcal{L}(a, \chi) \supset -\frac{\chi}{f_a} \partial_\mu a \partial^\mu a. \tag{2.34}$$

This decay is kinematically allowed only if $m_\chi^2 > 4m_a^2$. The amplitude for this process is straightforward to compute, as depicted by the Feynman diagram in Fig. 2.2.

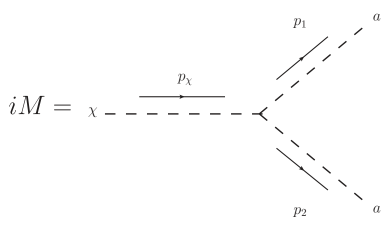

Figure 2.2: Tree-level Feynman diagram for radial decay into two axions $\chi \to aa$

.

In the center-of-mass frame, using the Mandelstan variable $s = m_\chi^2 = 2m_a^2 + 2p_1 \cdot p_2$, one finds

$$iM = \frac{2i}{f_a} p_1 \cdot p_2 = i \frac{m_\chi^2}{f_a} \left(1 - \frac{2m_a^2}{m_\chi^2}\right), \tag{2.35}$$

where we have considered a general axion mass.
The decay rate for a long-lived particle, $\Gamma \ll m_\chi$, is [48]

$$\Gamma(\chi \to aa) = \frac{1}{2m_\chi} \int d\Pi_f |M(\chi \to aa)|^2, \tag{2.36}$$

where the Lorentz invariant phase space factor for a two-final-particle state takes a simple form,

$$\int d\Pi_f \equiv \int \frac{d^3p_1}{(2\pi)^3} \frac{d^3p_2}{(2\pi)^3} \frac{1}{4E_1E_2} (2\pi)^4 \delta^4(p_\chi - p_1 - p_2) = \int \frac{d\Omega_{\rm cm}}{4\pi} \frac{1}{8\pi} \left(\frac{2|\vec{p}|}{E_{cm}}\right). \tag{2.37}$$

Here $|\vec{p}|$ is the magnitude of the three-momentum of either particle in the centre-of-mass frame. Using

$$|\vec{p}|^2 = \frac{m_\chi^2}{4} - m_a^2\ , \quad E_{\rm cm} = m_\chi, \tag{2.38}$$

the decay rate becomes

$$\Gamma_{\chi \to aa} = \frac{m_\chi^3}{16\pi f_a^2} \left(1 - \frac{2m_a^2}{m_\chi^2}\right)^2 \left(1 - \frac{4m_a^2}{m_\chi^2}\right)^{\frac{1}{2}}. \tag{2.39}$$

Requiring the condensate to survive until today implies that its decay rate must be lower than the current Hubble rate $\Gamma_{\chi \to aa} \sim \frac{m_\chi^3}{16\pi f_a^2} < H_0$. As discussed in the previous section 2.4.3, we impose $\frac{m_a^2}{m_\chi^2} \ll 1$, which allows us to approximate $\Gamma_{\chi \to aa} \simeq \frac{m_\chi^3}{16\pi f_a^2}$. This condition yields an upper bound on the radial mass:

$$m_\chi < 3.4 \cdot 10^3 \text{ eV} \left(\frac{f_a}{10^{12} GeV}\right)^{\frac{2}{3}} \left(\frac{H_0}{10^{-42} GeV}\right)^{\frac{1}{3}}. \tag{2.40}$$

Using the current Hubble value $H_0 \sim 1.4 \cdot 10^{-42}$ GeV and the abundance of DM from the misalignment mechanism (2.31), this constraint translates into a lower bound on the initial radial displacement,

$$\chi_i > 5 \cdot 10^{10} \text{ GeV} \left(\frac{\Omega_\chi^{\rm mis} h^2}{0.12}\right)^{\frac{1}{2}} \left(\frac{10^{12}\text{GeV}}{f_a}\right)^{\frac{1}{6}}. \tag{2.41}$$

In addition to the decay channel, the radial condensate could, in principle, be destroyed through efficient annihilation processes of the form $\chi\chi \to aa$. In the naive dimensional analysis (NDA) estimate, taking the incoming χ as quanta from the condensate, the annihilation cross section scales as

$$\sigma(\chi\chi \to aa) \simeq \frac{m_\chi^2}{f_a^4}. \tag{2.42}$$

The corresponding interaction rate is

$$\Gamma(\chi\chi \to aa) = n_\chi(T) \langle \sigma(\chi\chi \to aa) |\vec{v}_{\rm rel}| \rangle \simeq \frac{\rho_\chi(T)}{m_\chi} \frac{m_\chi^2}{f_a^4} |\vec{v}_{\rm rel}|, \tag{2.43}$$

where $\vec{v}_{\rm rel} = \frac{\vec{p}_{\rm rel}}{E_\chi}$ is the relative velocity of the incoming particles. We assume that the condensate has a small but non-zero velocity dispersion. For temperatures below the onset of oscillations, $T < T_{\rm osc}$, the radial energy density is given by (2.28), leading to

$$\Gamma(\chi\chi \to aa) \simeq \left(\frac{m_\chi}{M_{\rm pl}}\right)^{\frac{3}{2}} \left(\frac{\chi_i}{f_a}\right)^2 \frac{T^3}{f_a^2} |\vec{v}_{\rm rel}|, \; T \lesssim T_{\rm osc}. \tag{2.44}$$

Annihilations become efficient only if the interaction rate exceeds the Hubble expansion rate, for $\Gamma(\chi\chi \to aa) > H(T) \sim \frac{T^2}{M_{\rm pl}}$. Using $T_{\rm osc} \sim (M_{\rm pl} m_\chi)^{1/2}$, the condition for efficiency at $T < T_{\rm osc}$ becomes

$$1 > \frac{T}{T_{\rm osc}} > \left(\frac{f_a}{m_\chi}\right)^2 \left(\frac{f_a}{\chi_i}\right)^2 \frac{1}{|\vec{v}_{\rm rel}|}. \tag{2.45}$$

The right-hand side is always larger than unity for any physical relative velocity and not extremely suppressed χ_i, implying that there is no solution in this regime. Thus, annihilations are never efficient for $T < T_{\rm osc}$.
For temperatures above the onset of oscillations, $T > T_{\rm osc}$, the radial energy density is approximately constant, giving the following,

$$\Gamma(\chi\chi \to aa) \simeq \frac{\rho_\chi(T)}{m_\chi} \frac{m_\chi^2}{f_a^4} |\vec{v}_{\rm rel}| \simeq \frac{\chi_i^2}{f_a^2} \frac{m_\chi^3}{f_a^2} |\vec{v}_{\rm rel}|, \quad T > T_{\rm osc}. \tag{2.46}$$

This can be expressed in terms of the decay rate as

$$\Gamma(\chi\chi \to aa) \simeq \left(\frac{\chi_i}{f_a}\right)^2 |\vec{v}_{\rm rel}| \Gamma(\chi \to aa). \tag{2.47}$$

Since we get by construction $\chi_i \ll f_a$, $|\vec{v}_{\rm rel}| \ll 1$, the annihilation rate is always parametrically suppressed relative to the decay rate. Consequently, the process $\chi\chi \to aa$ never becomes efficient, and annihilations do not threaten the survival of the radial condensate.

Inefficient parametric resonance. The DM abundance we derived in Eq. (2.31) is valid only if the radial condensate evolves entirely within the linear regime. In this case, the radial and axion fields remain effectively decoupled at leading order, and the misalignment calculation is reliable. If parametric resonance were efficient, non-perturbative particle production could transfer a significant fraction of the radial homogeneous energy into axions, invalidating the perturbative treatment and altering the final abundance. To ensure that such non-linear effects remain negligible, we impose a conservative upper bound on the initial radial displacement:

$$\chi_i \leq 10^{-1} f_a. \tag{2.48}$$

The parametric resonance mechanism will be treated in Section 2.5.

Isocurvature bound. In the pre-inflationary scenario, radial fluctuations in the light-mass regime satisfy $\delta\chi \sim \frac{H_I}{2\pi}$, and lead to iso-curvature inhomogeneities in the DM density. Using the curvature perturbation on uniform-density hypersurfaces, one finds

$$\left.\frac{\delta\rho_\chi}{\rho_{DM}}\right|_{\rm iso} = \frac{\rho_\chi}{\rho_{DM}} 2\frac{\delta\chi_i}{\chi_i} \sim \frac{\rho_\chi}{\rho_{DM}} \frac{H_I}{\chi_i}. \tag{2.49}$$

These primordial isocurvature fluctuations are encoded in the dimensionless power spectrum $\Delta^2_{\rm iso}(k) = \frac{k^3}{2\pi^2} P_{\rm iso} = \left(\frac{\delta\rho_{DM}(k)}{\rho_{DM}}\right)^2$.

Global fits to Planck data demand that adiabatic fluctuations dominate the primordial spectrum. The constraint is expressed as

$$\frac{\Delta^2_{\rm iso}(k)}{\Delta^2_{\rm iso}(k)+\Delta^2_{\rm adi}(k)} < \beta_{\rm iso}(k). \tag{2.50}$$

At the pivot scale, $k_* = 0.050\ \text{Mpc}^{-1}$, Planck data [21] constrain

$$\beta_{\rm iso}(k_*) < 0.038 \ \ (95\%\ CL), \tag{2.51}$$

assuming uncorrelated standard CDI. On these scales, which re-enter the horizon near the matter-radiation equality, the adiabatic amplitude is well measured and $\Delta^2_{\rm adi} \sim 2.1 \cdot 10^{-9}$ is probed by the CMB. This bound implies

$$\chi_i \gtrsim \frac{H_I}{\pi\sqrt{\beta_{\rm iso}(k_*)\Delta^2_{\rm adi}(k_*)}}. \tag{2.52}$$

Using the light mass assumption $m_\chi \ll H_I$, this bound translates into

$$\chi_i > 3.5 \cdot 10^{-5}\ \text{GeV}\ \frac{m_\chi}{\text{eV}}. \tag{2.53}$$

The axion energy density from the misalignment mechanism. In the radial misalignment scenario, the dynamics of the axions are not affected by the radial mode. This implies that a population of axion condensate is still present and behaves as cold DM once it begins to oscillate, provided it does not thermalise.
The abundance of axion relics from the misalignment mechanism, from Section 1.3, is given by

$$\Omega_a^{\rm mis} h^2 \simeq 0.12 \cdot \theta_i^2 \left(\frac{f_a}{7\cdot 10^{11}\ \text{GeV}}\right)^{\frac{7}{6}}. \tag{2.54}$$

Then the ratio between the angular and radial energy density from the misalignment mechanism is given by, below the temperature $T <$ GeV where the axion starts to oscillate,

$$\frac{\rho_a^{\rm mis}}{\rho_\chi^{\rm mis}} = \frac{\Omega_a^{\rm mis}}{\Omega_\chi^{\rm mis}} \sim\ 0.25 \cdot \frac{\theta_i^2}{\frac{\chi_i^2}{f_a^2}} \left(\frac{10^{12}\text{GeV}}{f_a}\right)^{\frac{5}{6}} \sqrt{\frac{\text{eV}}{m_\chi}}. \tag{2.55}$$

To avoid an overabundance of DM, we impose that the axion energy density is smaller than the radial abundance, which sets an upper bound on the initial misalignment angle θ_i:

$$\theta_i \leq 2\left(\frac{\chi_i}{f_a}\right)\left(\frac{f_a}{10^{12}\text{GeV}}\right)^{\frac{5}{12}}\left(\frac{m_\chi}{\text{eV}}\right)^{\frac{1}{4}}. \tag{2.56}$$

Other mechanisms that could suppress the axion condensate are the thermalisation process and effective decay into photons. Those are not relevant for $m_a \lesssim$ eV, which is the region of interest for the QCD axion mass.

2.4.4 Results for radial mode DM from the misalignment mechanism

As illustrated in Fig. 2.3, the misalignment mechanism leaves a large parameter space region in which the radial condensate can account for the entirety or a fraction of the DM today. In particular, viable solutions require at least $f_a \geq 10^{12}$ GeV, while remaining consistent up to

$f_a \lesssim 10^{18}$ GeV. The range of allowed radial mass is remarkably broad, stretching from 10^{-9} eV to the MeV scale.

Achieving such a light mass relative to the PQ scale inevitably implies a severe hierarchy. In this setup manifests itself as a very small quartic coupling λ_{PQ}. For illustration, taking $m_\chi \sim$ keV, $f_a \sim 10^{12}$ GeV,

$$m_\chi \sim \sqrt{\lambda_{PQ}} f_a \Longrightarrow \sqrt{\lambda_{PQ}} \sim 10^{-18}, \tag{2.57}$$

highlighting the degree of suppression required, an aspect that is not emphasised in the Co. et al paper [11]. This hierarchy is a generic feature of scenarios in which the radial mode is parametrically lighter than the PQ scale. We will discuss the technical naturalness of the light radial mode in Chapter 3.

2.5 Radial mode DM from parametric resonance

When the radial field is initially displaced far from the minimum of its potential, its subsequent evolution becomes nonlinear as soon as oscillations begin. During this phase, coherent oscillations of the homogeneous radial mode induce a time-dependent effective mass for both radial and axion fluctuations. Modes whose frequencies fall within the resonance bands of the background oscillation undergo exponential amplification. This mechanism is described in detail in the Appendix A.
This resonant production of fluctuations efficiently transfers energy from the radial zero mode into excited radial and axion modes. Ultimately, the initial homogeneous energy density is transformed into a bath of radial and axion excitations with comparable energy densities. In Ref.[11], the axion population emerging from this process was assumed to constitute DM. In this section, by contrast, we will instead take the radial population to be responsible for the observed DM abundance.

2.5.1 Analytical dynamics

We take the onset of the evolution to be at time t_i, in RD, and impose the initial conditions

$$\chi(t_i, \vec{x}) = \chi(t_i) \gg f_a, \quad \dot{\chi}(t_i, \vec{x}) = 0, \quad a(t_i, \vec{x}) = a(t_i), \quad \dot{a}(t_i, \vec{x}) = 0. \tag{2.58}$$

We assume that fluctuations are negligibly small at this stage, so all modes begin in their vacuum state.
In the regime $\chi \gg f_a$, the potential is approximately quartic. Taking the homogeneous axion constant from Eq. (2.6), the radial equation of motion simplifies to

$$\ddot{\chi}_0 + 3H\dot{\chi}_0 + \lambda_{\rm PQ}\chi_0^3 \simeq 0\,. \tag{2.59}$$

This is equivalent to a free homogeneous scalar field with effective mass $m_\chi^{\rm eff}(t) = \sqrt{\lambda_{\rm PQ}}\,\chi_0(t)$. We define the initial effective frequency

$$w_i \equiv m_\chi^{\rm eff}(t_i) = \sqrt{\lambda_{\rm PQ}}\,\chi_i\,. \tag{2.60}$$

The field initially evolves slowly because Hubble friction dominates and χ_0 remains approximately frozen at χ_i. As the Universe expands and the Hubble rate decreases, the system eventually becomes underdamped, and the radial field begins to oscillate. The onset of oscillations $t_{\rm osc}$ is implicitly defined by the matching condition

$$H(t_{\rm osc}) \simeq w_i\,. \tag{2.61}$$

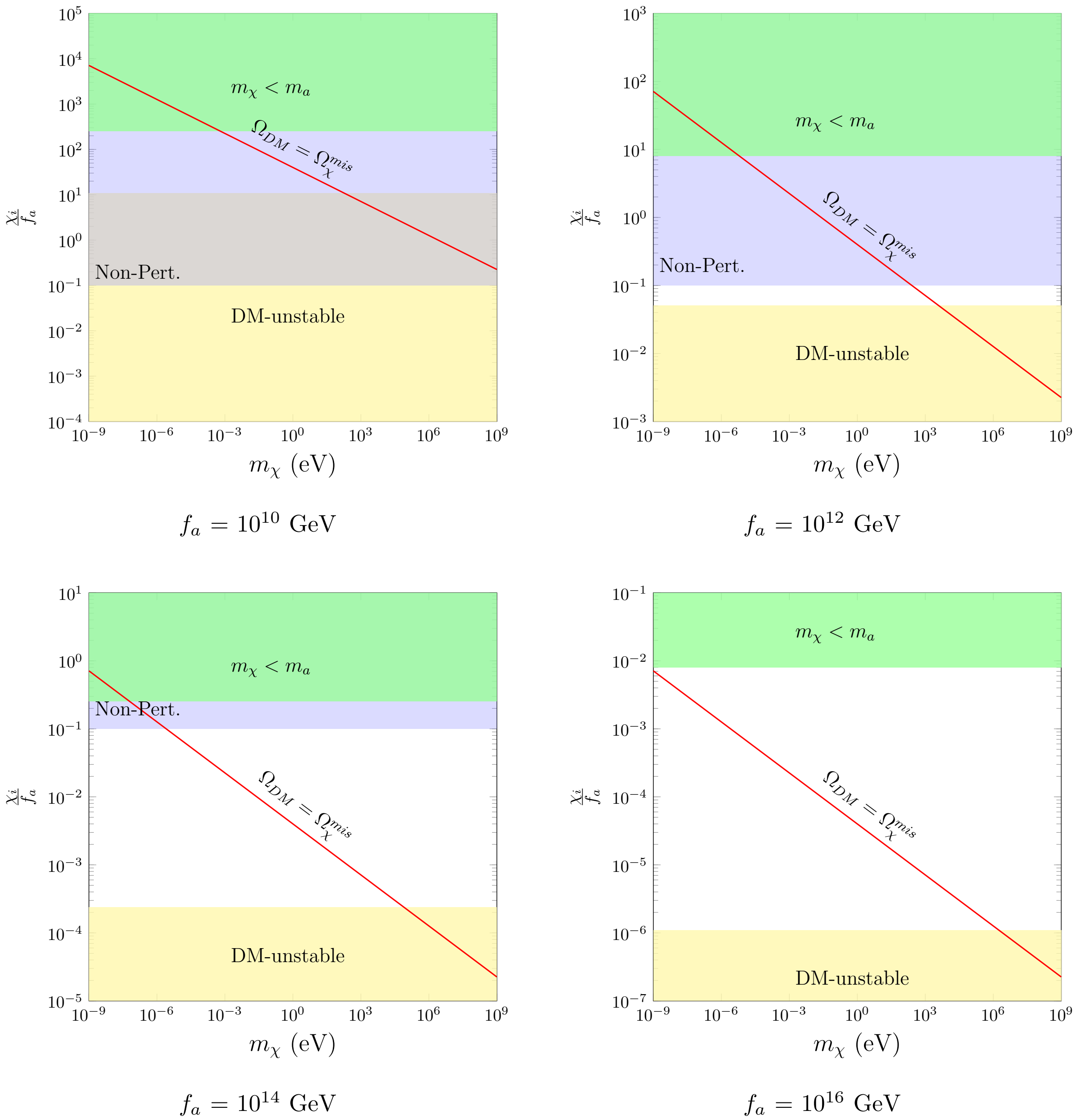

Figure 2.3: Constraints on the parameter space of the radial initial amplitude χ_i and mass m_χ, for different values of f_a. We assume that the full DM abundance is produced from small oscillations of the radial mode via the misalignment mechanism. The yellow region is excluded by efficient radial decay into axions. The blue region indicates where the perturbative assumption $\chi_i < 10^{-1} f_a$ breaks down. The light-green region marks where the axion mass is bigger than the radial mass. The isocurvature bound is not visible on the scale of the plots. The red line indicates the parameter combinations for which the radial condensate reproduces the observed dark-matter abundance today, $\Omega_{DM}^{\rm exp} \sim \Omega_\chi^{\rm mis}$.

As in the standard misalignment mechanism, the field remains overdamped and essentially frozen between the initial time and the onset of oscillations. For this reason, in the first approximation, we can define at t_i physical quantities that remain unchanged until the onset of oscillation. Before analysing the oscillatory regime, we define some useful quantities at $t_{\rm i}$. The homogeneous radial yield,

$$Y_{\chi 0} \equiv \frac{n_{\chi 0}}{s}, \tag{2.62}$$

where s is the entropy density and $n_{\chi 0}$ the number density of the radial zero-mode, in the case of entropy conservation, encodes the occupation number in a comoving volume. At the onset of oscillations, the yield can be expressed in terms of the initial displacement χ_i. Using the matching condition (2.61) in the entropy density,

$$s(T_i) \sim T_{\rm i}^3 \sim (M_{\rm pl} w_i)^{\frac{3}{2}} \,. \tag{2.63}$$

For the number density, since the field is nearly frozen with a quartic potential,

$$n_{\chi 0}(T_i) = \frac{\rho_{\chi 0}(T_i)}{m_\chi^{\rm eff}(T_i)} \sim m_\chi^{\rm eff}(T_i)\chi_0^2(T_i) \sim w_i \chi_i^2, \tag{2.64}$$

where $\rho_{\chi 0}(t_i) = \frac{1}{4}\lambda_{PQ}\chi_i^4 \sim w_i^2\chi_i^2$.
Combining these expressions

$$Y_{\chi 0}(T_i) \equiv \frac{n(T_i)}{s(T_i)} \sim \frac{\chi_i^2}{w_i^{\frac{1}{2}} M_{\rm pl}^{\frac{3}{2}}}. \tag{2.65}$$

Since the FLRW metric is conformally flat and the potential is approximately quartic at early times, it is convenient to introduce rescaled conformal-time and field variables

$$t \to z \equiv w_i \int \frac{dt}{R(t)}, \quad \delta a \to \delta f = R\frac{\chi}{\chi_i}\delta a, \quad \chi_0 + \delta\chi \to X + \delta X \equiv R\frac{(\chi_0 + \delta\chi)}{\chi_i}. \tag{2.66}$$

As discussed in Appendix A, parametric resonance of the fluctuations requires an oscillatory background source, the radial homogeneous mode. With this change of coordinates, the covariant d'Alembertian can be decomposed as

$$\ddot{\chi}_0 + 3H\dot{\chi}_0 = \frac{w_i^2\chi_i}{R^3}\left[X'' - \frac{R''}{R}X\right], \quad {}' \equiv \frac{d}{dz}. \tag{2.67}$$

Using the fact that in RD

$$R \propto \sqrt{t} \propto z, \quad R'' = 0, \tag{2.68}$$

the homogeneous equation of motion reduces to a non-linear oscillator in flat spacetime,

$$X'' + X^3 = 0. \tag{2.69}$$

This reduction is a consequence of the conformal invariance of a $\lambda\phi^4$ theory in a conformally flat background. Equation (2.69) admits an integral of motion, the conformal energy,

$$\frac{X'^2}{2} + \frac{X^4}{4} = \text{const}\,. \tag{2.70}$$

The Cauchy boundary conditions at $z(t_{\rm i}) \equiv z_{\rm i}$, recalling that $\chi_i = \chi(t_i)$, $\dot{\chi}(t_i) = 0$, and normalize the scale factor such that $R(t_i) = 1$,

$$X(z_{\rm i}) = R(z_i)\frac{\chi_0(z_i)}{\chi_i} = 1, \quad X'(z_{\rm i}) = \frac{R(t_i)}{w_i\chi_i}\frac{d}{dt}\left(\chi_0 R\right)\Big|_{t=t_{\rm i}} = \frac{H_i}{w_i}. \tag{2.71}$$

Identifying t_i with the onset of oscillation, $H_i = w_i$, the energy integral gives

$$\frac{X'^2}{2} + \frac{X^4}{4} = \frac{X'^2(z_i)}{2} + \frac{X^4(z_i)}{4} = \frac{3}{4}. \tag{2.72}$$

Separating variables, the integral on the right-hand side can be rewritten as a Jacobi elliptic cosine (see Eq. (A.23) in Appendix A):

$$z - z_i = \sqrt{2} \int_1^{X(z)} \frac{dX}{\sqrt{3 - X^4}} \,. \tag{2.73}$$

The exact solution is

$$X(z) = 3^{1/4}\, \mathrm{cn}\Big(3^{1/4}(z - z_i) - \mathrm{cn}^{-1}\Big(3^{-1/4}, \tfrac{1}{\sqrt{2}}\Big)\,,\, \tfrac{1}{\sqrt{2}}\Big)\,, \tag{2.74}$$

with elliptic modulus $k = 1/\sqrt{2}$, which is independent of the (non-trivial) initial conditions. As discussed in Eq. (A.25), the solution is periodic with period

$$T = \frac{4}{3^{1/4}}\, K\Big(\tfrac{1}{\sqrt{2}}\Big) \simeq 5.6\,, \tag{2.75}$$

where $K(k)$ is the complete elliptic integral of the first kind. The solution is shown in Fig. A.3. In this regime, the homogeneous mode evolves in an effective quartic potential, so the virial

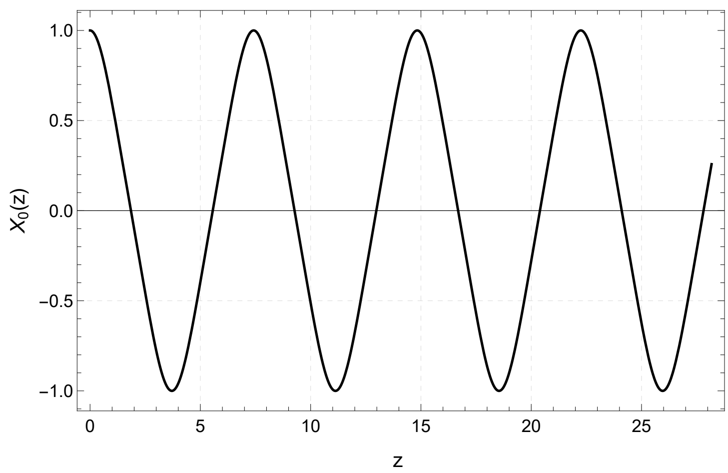

Figure 2.4: The oscillatory solution of the homogeneous mode in Eq. (A.38), in rescale conformal time $z = w_i\eta$ with $X(z_i) = 1,\ X\ (z_i) = 1, z_i = 0$.

theorem, Eq. (1.47), gives the equation of state

$$w_\chi = \frac{\langle \mathrm{Kin}\rangle - \langle \mathrm{Pot}\rangle}{\langle \mathrm{Kin}\rangle + \langle \mathrm{Pot}\rangle} \simeq \frac{1}{3}\,, \tag{2.76}$$

indicating that the oscillating radial condensate behaves as radiation at the background level. Before the decay into fluctuations becomes efficient, the averaged energy density is

$$\rho_{\chi_0} = \langle \mathrm{Kin}\rangle + \langle \mathrm{Pot}\rangle = 3\langle \mathrm{Pot}\rangle \simeq \frac{3}{4}\lambda_{PQ} \left(\frac{R_{osc}}{R(t)}\right)^4 \chi_i^4, \tag{2.77}$$

modulo an order one factor from the integration over $X(t)$.

To analyse the production of axion and radial particles, we include the leading correction from the fluctuation fields. Since the homogeneous axion mode is constant when the radial mode starts to oscillate $a_0(t) = \mathrm{const}$, the leading effect originates from the time-dependent radial

homogeneous background $\chi_0(t)$ acting on the fluctuations $\delta\chi$ and δa.
At the leading order, the EOM for the fluctuations are

$$\begin{cases} \nabla_\mu \left(\left(1 + \frac{\chi}{f_a}\right)^2 \nabla^\mu \delta a \right) \simeq \nabla_\mu \left(\frac{\chi_0^2}{f_a^2} \nabla^\mu \delta a \right) = 0, \\ \Box \delta\chi - 3\lambda_{PQ}\chi_0^2 \delta\chi \simeq 0. \end{cases}$$

Transforming to the rescaled variables of Eq. (2.66), the friction terms are absorbed, and the equations of motion become

$$\begin{cases} \delta X'' - \left(\frac{\nabla^2}{w_i^2} - 3X_0^2 \right) \delta X \simeq 0, \\ \delta f'' - \left(\frac{\nabla^2}{w_i^2} + \frac{X_0''}{X_0} \right) \delta f \simeq 0. \end{cases} \tag{2.78}$$

Quantising the fields in Fourier space with rescaled comoving momenta

$$\kappa_r = \frac{k_{r,\mathrm{com}}}{w_i}, \qquad \kappa_\theta = \frac{k_{\theta,\mathrm{com}}}{w_i}, \tag{2.79}$$

the mode functions satisfy

$$\begin{cases} \delta X''_{\kappa_r} + \left(\kappa_r^2 + 3X_0^2\right) \delta X_{\kappa_r} = 0 + \mathcal{O}(\delta X^2 X_0), \\ \delta f''_{\kappa_\theta} + \left(\kappa_\theta^2 + X_0^2\right) \delta f_{\kappa_\theta} = 0 + \mathcal{O}(\delta f \delta X), \end{cases} \tag{2.80}$$

where we neglect the subleading mass correction ($R^2 f_a^2/\chi_i^2 \ll 1$), which is valid in the regime ($\chi \gg f_a$).

The fluctuation equations take the form of a Lamé equation, introduced in Appendix A, in Eq. (A.48), with resonance parameters

$$\alpha_r = \frac{\kappa_r^2}{\sqrt{3}}, \quad q_r = 3, \quad \alpha_\theta = \frac{\kappa_\theta^2}{\sqrt{3}}, \quad q_\theta = 1. \tag{2.81}$$

These equations possess the characteristic band structure of the Lamé equation. The source of instability is the periodic homogeneous radial background that induces a time-dependent effective mass for the fluctuations, leading to parametric resonance. Consequently, modes lying within instability bands are exponentially amplified even when starting from arbitrarily small initial perturbations. By Floquet's theorem,

$$\delta f_{\kappa_\theta}(z) \sim e^{\mu_\theta(\kappa_\theta)\, z}, \qquad \delta X_{\kappa_r}(z) \sim e^{\mu_r(\kappa_r)\, z}, \tag{2.82}$$

where $\mu_\kappa(q)$ is the Floquet exponent. Modes with $\mathrm{Re}[\mu_\kappa(q)] > 0$ lie inside resonance bands and are exponentially amplified; the stability/instability chart depends only on the resonance parameters (α, q), not on the initial conditions. For $q_\theta = 1$ and $q_r = 3$, the instability bands are

$$0 < \kappa_\theta < 0.9, \quad 1.6 < \kappa_r < 1.75. \tag{2.83}$$

The Floquet exponents for different momenta are computed numerically and shown in Fig. 2.5, while a resonant amplification of a specific radial mode is illustrated in Fig. 2.6.

As seen from Fig. 2.5, the resonant modes satisfy $k \sim w_i$, with physical momenta $p \cdot R = k$. The resulting energy densities are

$$\rho_{\delta a}(t) \sim \frac{w_i}{R(t)}\, n_a(t), \qquad \rho_{\delta\chi}(t) \sim \frac{w_i}{R(t)}\, n_{\delta\chi}(t). \tag{2.84}$$

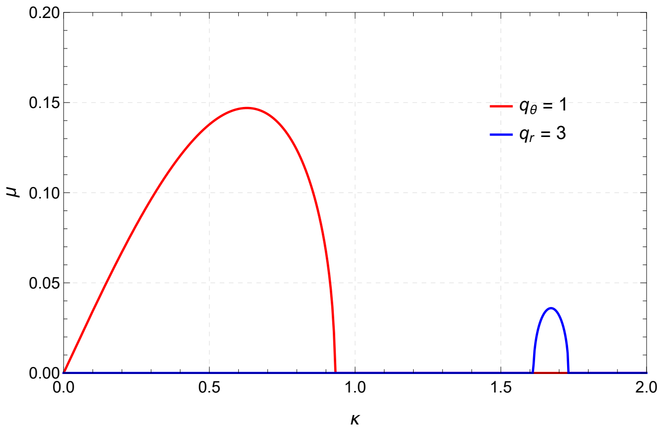

Figure 2.5: Floquet exponent for solutions of the Lamé equation with resonance parameters $q_\theta = 1$ (angular mode) and $q_r = 3$ (radial mode).

The comoving number density of the radial fluctuations produced is defined from the instantaneous dispersion relation $w_{\kappa_r}(z) = \sqrt{\kappa_r^2 + 3X_0^2(z)}$:

$$n_{\kappa_r}(z) = \frac{w_{\kappa_r}(z)}{2}\left(|\delta X_{\kappa_r}|^2 + \frac{|\delta X'_{\kappa_r}|^2}{w_{\kappa_r}^2}\right) - n_{\kappa_r}(z_i) \propto e^{2\mu_r\, z}\,, \tag{2.85}$$

where it is normalised so that the particle number vanishes at z_i. In physical variables, the occupation number of both species grows as

$$n_k \propto e^{2\mu_\kappa\, z(t)}\,. \tag{2.86}$$

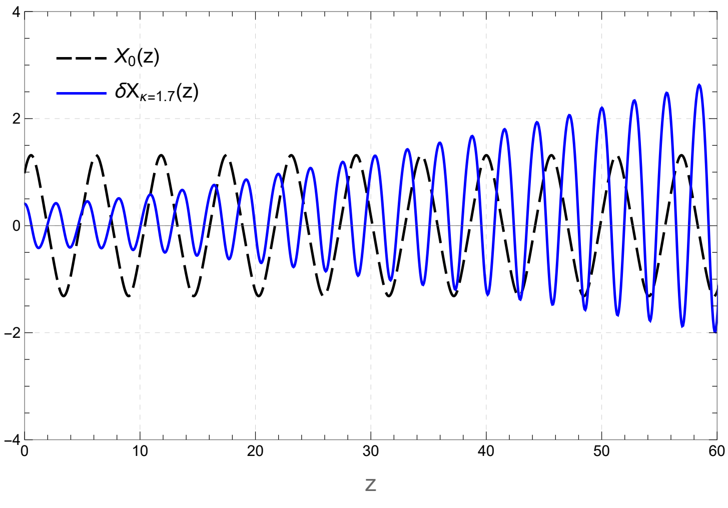

Figure 2.6: Resonant amplification of a radial fluctuation mode for $\kappa_r = 1.73$ and $q_r = 3$. The blue curve shows the growing mode function $\delta X_{\kappa_r}(z)$, while the dashed black curve shows the background oscillation $X_0(z)$.

2.5.2 Non-linear dynamics

In the previous sections, we have shown that an initially homogeneous oscillating radial background efficiently sources axion and radial fluctuations through parametric resonance. Once a significant fraction of modes within the resonance bands becomes populated, the system exits the linear regime. At this stage, the following effects become relevant:

- Particle production reduces the amplitude of the coherent oscillations of the background field. This, in turn decreases the effective oscillation frequency, shifting the position of the resonance bands towards lower momenta.
- Scattering among the produced fluctuations becomes efficient, modifying the resonance structure.

The subsequent evolution is strongly model-dependent and, in general, requires lattice simulations.
In Ref.[11], the authors adopt two key assumptions,

- the initial energy stored in the homogeneous radial mode is transferred, by the end of the parametric resonance, into a comparable population of axion and radial fluctuations. In particular, the dominant excited modes carry comoving momenta ($k \sim \omega_i$), leading to the estimate
$$\rho_\chi(t) \sim \omega_k(t) n_\chi(t), \quad \rho_a(t) \sim \omega_k(t) n_a(t). \tag{2.87}$$
This transfer is expected to occur at early times, roughly at [49],
$$z_{\text{eff}} \sim \mathcal{O}(10^2), \tag{2.88}$$
corresponding to an effective temperature
$$T_{\text{eff}} \sim 0.1 \sqrt{M_{\text{pl}} \sqrt{\lambda_{PQ}} \chi_i} \sim 0.1\ T_i. \tag{2.89}$$
- Approximate adiabaticity, where the comoving yield ($Y_j \equiv n_j/s$) of fluctuation is related to the initial yield,
$$Y_{\delta\chi} \sim Y_{\delta a} \sim Y_{\chi_i}. \tag{2.90}$$

After production, both axion and radial fluctuations redshift and may subsequently behave as non-relativistic matter at late times.
An additional effect arises from the constant mass contribution of the radial mode. The effective frequency of fluctuations is given by

$$\omega_\kappa^2(z) = \kappa_r^2 + 3X_0^2 + R^2 \frac{f_a^2}{\chi_i^2}. \tag{2.91}$$

As the amplitude of the background oscillations decreases due to Hubble expansion, the constant mass term can eventually become dominant. In this regime, the field gradually oscillates around the true minimum of the potential. While the equations of motion formally remain those of the misalignment regime, the late-time state is instead determined by a highly occupied fluctuation spectrum, which subsequently evolves as a non-relativistic component and may contribute to the DM abundance.

These assumptions are clearly non-trivial and must be carefully tested. To this end, we have developed a lattice simulation, described in Appendix A. Our preliminary results indicate that the assumptions are reasonable.

2.5.3 Energy abundance of the radial population Ω_χ^{PR}

From the above discussion, we have a population of radial modes that, soon after the temperature T_{eff}, do not interact efficiently with the axion. The yield expressed as a function of the initial displacement χ_i as

$$Y_\chi \sim Y_i \sim \frac{\chi_i^2}{w_i^{\frac{1}{2}} M_{\rm pl}^{\frac{3}{2}}}, \quad T \simeq T_{\rm eff}. \tag{2.92}$$

The energy density at this temperature is dominated by the physical momenta $p_\chi = \frac{k}{R}$, recalling that excited modes have comoving momenta $k \sim w_i$,

$$\rho_\chi = E_\chi n_\chi \sim \frac{w_i s}{R} Y_i, \qquad T = T_{\rm eff}, \tag{2.93}$$

where s is the entropy density.
The production of the particle occurs very early in time, then the momenta redshift and the constant vacuum mass term dominate the energy of the radial particle well before the matter-radiation equality.
Assuming that the yield remains constant during the expansion of the universe, i.e., no entropy injection and conserved comoving number $n_\chi R^3 = $ const, the today energy density is

$$\rho_\chi(T_0) = m_\chi n_\chi(T_0) = m_\chi s_0 Y_\chi(T_0) \sim m_\chi s_0 Y_i, \tag{2.94}$$

with s_0 the current value of the entropy density. The number density that explains the observed DM abundance $\Omega_{\rm exp}^{DM} h^2 = 0.12$, or equivalently $\frac{\rho_{DM}}{s_0} \sim 0.4$eV, can be expressed as a function of the initial displacement χ_i, the vacuum mass m_χ and the axion decay constant f_a,

$$\Omega_\chi^{PR} h^2 \sim 0.12 \cdot \sqrt{\frac{m_\chi}{10^2 \text{ eV}}} \left(\frac{5 \cdot \chi_i}{10^2 f_a}\right)^{\frac{3}{2}} \left(\frac{f_a}{10^9 \text{ GeV}}\right)^2 . \tag{2.95}$$

Inverting the relation, the initial condition can be expressed parametrically as

$$\chi_i \simeq 2 \cdot 10^{12} \text{ GeV} \left(\frac{\Omega_\chi^{PR} h^2}{0.12}\right)^{\frac{2}{3}} \left(\frac{\text{eV}}{m_\chi} \frac{10^9 \text{GeV}}{f_a}\right)^{\frac{1}{3}} . \tag{2.96}$$

2.5.4 Constraints

Efficient parametric resonance. The parametric resonance mechanism requires a sizable displacement from the minimum of the potential, imposing a lower bound $\chi_i > f_a$.

Survival of the condensate. After the parametric resonance ceases due to back-reaction, roughly at $T_{\rm eff}$, we can trust the perturbative regime. The discussion is completely analogous to the one for the misalignment in section 2.4.3.
Requiring $\Gamma_{\chi \to aa} = \frac{m_\chi^3}{16\pi f_a^2} < H_0$, using the DM abundance in Eq. (2.95) to replace f_a with χ_i, m_χ,

$$\chi_i < 6 \cdot 10^{12} \text{ GeV} \left(\frac{\text{eV}}{m_\chi}\right)^{\frac{5}{6}} \left(\frac{\Omega_\chi^{PR} h^2}{0.12}\right)^{\frac{2}{3}} . \tag{2.97}$$

Warmness bound. The production of DM arises from the non-zero modes, with physical momenta p_χ. The warmness bound [20], requires that at matter-radiation equality $T_{eq} \sim$ eV, $\left.\frac{p_\chi}{m_\chi}\right|_{eq} < 10^{-3}$. Using $p_\chi \cdot R = $ const , $p_\chi(T_{\rm eff}) = w_i$ with $T_{\rm eff} \sim 0.1\sqrt{w_i M_{\rm pl}}$ the physical momenta at equality,

$$p_\chi(T_{\rm eq}) = w_i \frac{R(T_{\rm eff})}{R(T_{\rm eq})} \sim w_i \frac{T_{\rm eq}}{T_{\rm eff}} \left(\frac{g_{*s}(T_{\rm eq})}{g_{*s}(T_{\rm eff})}\right)^{\frac{1}{3}} \sim 3\sqrt{\frac{w_i}{M_{pl}}} T_{eq}, \tag{2.98}$$

where we have taken $R \cdot T \cdot g_{*s}^{\frac{1}{3}} = \text{const}$, and $\frac{g_{*s}(T_{\rm eq})}{g_{*s}(T_{\rm eff})} \sim \frac{1}{50}$.
Using $w_i = \sqrt{\lambda_{PQ}}\chi_i$ and the vacuum mass relation $\sqrt{\lambda_{PQ}} = \frac{m_\chi}{f_a}$, the warmness bound require that

$$\frac{p_\chi}{m_\chi}\Big|_{eq} \simeq 3\frac{T_{eq}}{m_\chi}\sqrt{\frac{m_\chi \chi_i}{M_{\rm pl} f_a}} < 10^{-3}. \tag{2.99}$$

Using the DM abundance (2.96), this gives an upper bound, modulo an order one factor,

$$\chi_i < 7 \cdot 10^{16} \text{ GeV} \left(\frac{\Omega_\chi^{PR} h^2}{0.12}\right)^{\frac{1}{2}}. \tag{2.100}$$

Isocurvature bound. The discussion is completely analogous to the section in the misalignment mechanism 2.4.3 with a light effective mass $\lambda_{PQ}\chi_i^2 \ll H_I^2$. The isocurvature fluctuations are constrained from CMB anisotropies. The bound on the initial displacement is analogous to Eq. (2.52),

$$\chi_i \gtrsim \frac{H_I}{\pi\sqrt{\beta_{\rm iso}(k_*)\Delta^2_{\rm adi}(k_*)}}. \tag{2.101}$$

Using the light mass assumptions for the initial displacement, $H_I > \lambda_{PQ}\chi_i$, the quartic coupling is limited,

$$\lambda_{PQ} < \pi^2 \beta_{\rm iso}(k_*)\Delta^2_{\rm adi}(k_*). \tag{2.102}$$

Using the DM abundance from (2.96), this translates into

$$\chi_i < 10^{16} \text{ GeV} \left(\frac{\text{eV}}{m_\chi}\right)^{\frac{2}{3}} \left(\frac{\Omega_\chi^{PR} h^2}{0.12}\right)^{\frac{2}{3}}. \tag{2.103}$$

Quantum Gravity (QG) bound. At an energy density of the order of the Planck density, fluctuations of the metric become so large that we can no longer assume space-time as a classical metric $g_{\mu\nu}$. This means that without a full QG theory, it is impossible to treat the field ϕ as being classical, unless

$$\begin{aligned} \partial_\mu\phi\partial^\mu\phi &\lesssim M_{\rm pl}^4, \quad \mu = 0,1,2,3, \\ V(\phi) &\lesssim M_{\rm pl}^4. \end{aligned} \tag{2.104}$$

The higher energy density arises from the initial condition for a homogeneous field when $\chi_i \gg f_a$; this bound translates into

$$\lambda_{PQ}\chi_i^4 \lesssim M_{\rm pl}. \tag{2.105}$$

Requiring the perturbative regime for the field part, we get the upper bound $\lambda_{PQ} \lesssim \mathcal{O}(1)$. Then the stronger bound is considered

$$\chi_i < M_{\rm pl}, \tag{2.106}$$

or in another parameterisation,

$$\frac{\chi_i}{f_a} \lesssim 2.4 \cdot 10^9 \left(\frac{10^9 \text{ GeV}}{f_a}\right). \tag{2.107}$$

In our scenario, this constraint is much weaker because we have $\lambda_{PQ} \ll 1$ to realise a light radial mode.

Axion DM from parametric resonance Ω_a^{PR}. Axions produced by parametric resonance are emitted at $T_{\rm eff} \sim 0.1\, T_{\rm osc}$ with momenta $p_a(T_{\rm eff}) \sim w_i$. At lower temperatures, redshift as

$$p_a(T) = w_i \, \frac{T}{T_{\rm eff}} \left(\frac{g_{*s}(T)}{g_{*s}(T_{\rm eff})} \right)^{1/3} . \tag{2.108}$$

For QCD axions, the vacuum mass $m_a \simeq 6\,{\rm eV}\,(10^6\,{\rm GeV}/f_a)$ turns on below $T_{\rm QCD}$, and the non-relativistic transition $p_a(T_{\rm NR}) \simeq m_a$ gives

$$T_{\rm NR} \sim 2.6 \times 10^3\,{\rm MeV} \left(\frac{\rm eV}{m_\chi} \frac{10^9\,{\rm GeV}}{f_a} \right)^{1/3} , \tag{2.109}$$

where we used the radial mode DM condition (2.96) to eliminate χ_i, and assumed $g_{*s}(T_{\rm NR})/g_{*s}(T_{\rm eff}) \sim 1/50$. Since $T_{\rm NR} \gg T_{\rm eq} \simeq 0.8\,{\rm eV}$ throughout the open parameter space of Fig. 2.7, the axions are non-relativistic well before matter-radiation equality.

The DM energy density ratio between the radial and angular population is given by,

$$\frac{\Omega_a^{\rm PR}}{\Omega_\chi^{\rm PR}} \simeq \frac{m_a}{m_\chi} . \tag{2.110}$$

Requiring the axion relic to be subdominant, to avoid overproduction of DM, this is precisely the condition $m_\chi \gg m_a$ discussed in Section 2.4.3. The upper bound is

$$\chi_i \lesssim 10^{13}\ {\rm GeV} \cdot \left(\frac{\Omega_\chi^{PR} h^2}{0.12} \right)^{\frac{2}{3}} . \tag{2.111}$$

2.5.5 Results for radial mode DM from parametric resonance

As illustrated in Fig. 2.7, with the parametric mechanism, the radial field population can account for the entirety of today's DM. In particular, viable solutions require $f_a \in [10^8, 10^{12}]$ GeV. The range of allowed radial mass extends from 10^{-4} eV to the keV scale, which requires a very small λ_{PQ}, as discussed in the misalignment scenario. The initial displacement required χ_i is not fine-tuned.

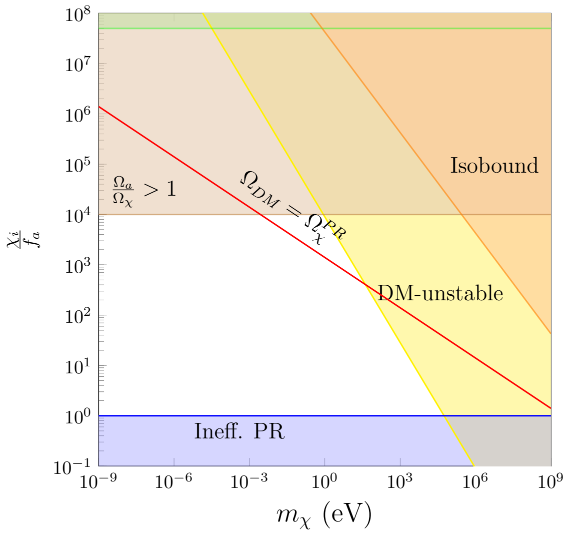

$f_a = 10^9$ GeV

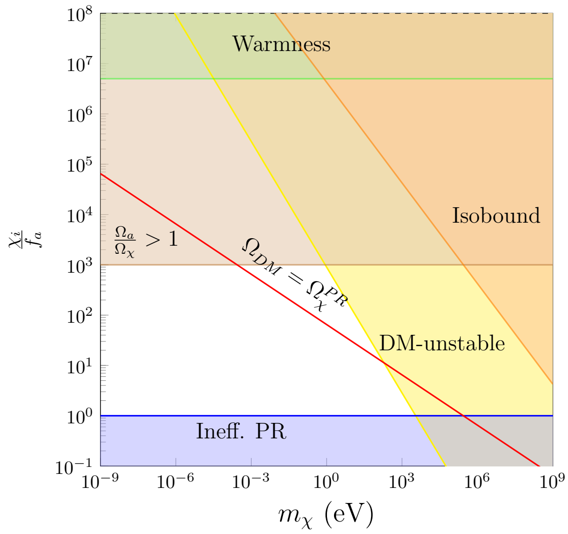

$f_a = 10^{10}$ GeV

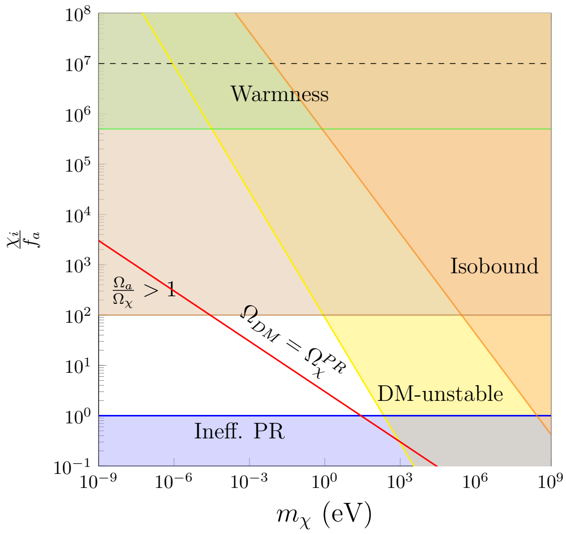

$f_a = 10^{11}$ GeV

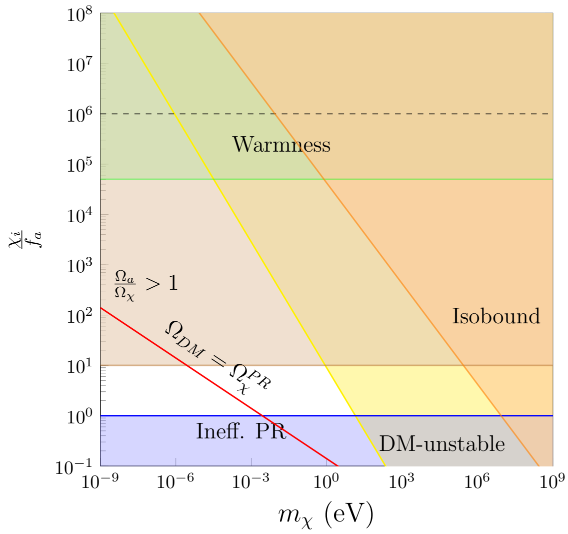

$f_a = 10^{12}$ GeV

Figure 2.7: Constraints on the parameter space of the radial field initial amplitude χ_i and vacuum mass m_χ for different f_a. We assume that DM production is dominated by radial fluctuations from parametric resonance. The yellow-shaded region is excluded due to efficient radial field decay into axions. The blue region indicates where the assumption $\chi_i > f_a$ breaks down. The brown-shaded region is excluded for overproduction of DM. The orange region is ruled out by isocurvature constraints, while the green region corresponds to radial fields that are too warm to constitute viable DM. The black dashed curves denote the upper bound from QG effects, beyond which our calculation is no longer valid. The red line indicates parameter values for which the radial field population produced via parametric resonance accounts for the observed DM abundance today.

Chapter 3

The minimal renormalizable Higgs portal model

In this chapter, we discuss how the radial mode of the PQ field communicates with the SM through the renormalizable Higgs portal interaction $(H^\dagger H)(\Phi^\dagger\Phi)$.

We analyse the model in two regimes. In the first, we review the standard scenario, following Refs. [50–53], where the radial mode has a mass heavier than the Higgs mass, $m_\chi \gg m_h$. In the second regime, motivated by the radial DM scenarios of Chapter 2, and axion DM from parametric resonance [11], we impose $m_\chi \ll m_h$. In this regime, we identify the unique radiatively stable configuration and show that a light radial mode is technically natural.

3.1 The Scalar-Higgs portal model in the QCD axion framework

The Higgs sector of the SM possesses a unique feature: it allows renormalizable interactions with gauge-singlet hidden sectors. In particular, the Higgs bilinear $H^\dagger H$ is the only dimension-two operator in the SM that is both gauge and Lorentz invariant. As a consequence, one can construct the renormalizable interaction

$$(H^\dagger H)(\Phi^\dagger\Phi), \tag{3.1}$$

where Φ is a new (complex) singlet scalar field. This Scalar-Higgs portal is one of the most economical extensions of the SM. The new complex field Φ is identified with the PQ field, charged under a global symmetry $U(1)_{PQ}$ with a SSB pattern. Without loss of generality, we will consider the scalar sector, described by the following Lagrangian,

$$\mathcal{L} = -(D_\mu H)^\dagger(D^\mu H) - (\partial_\mu\Phi)^\dagger(\partial^\mu\Phi) - V(H,\Phi), \tag{3.2}$$

where D_μ is the covariant derivative.

Potential and couplings. In accordance with the convention adopted in [51], we consider the tree-level scalar potential of the form

$$V(H,\Phi) = \lambda_H\left(H^\dagger H - \frac{v^2}{2}\right)^2 + \lambda_\Phi\left(\Phi^\dagger\Phi - \frac{f_a^2}{2}\right)^2 + 2\lambda_{H\Phi}\left(H^\dagger H - \frac{v^2}{2}\right)\left(\Phi^\dagger\Phi - \frac{f_a^2}{2}\right). \tag{3.3}$$

where $v = 246$ GeV is the EW scale and f_a the scale of SSB of the global $U(1)_{PQ}$ symmetry. All couplings are real, $\lambda_H, \lambda_\Phi, \lambda_{H\Phi} \in \mathbb{R}$. For the potential to be bounded from below and to admit a local minimum with $\langle H^\dagger H\rangle, \langle\Phi^\dagger\Phi\rangle \neq 0$, the following conditions must be satisfied:

$$\lambda_H, \lambda_\Phi > 0, \quad \lambda_{H\Phi}^2 < \lambda_H \lambda_\Phi, \tag{3.4}$$

with the potential $V(H, \Phi)$ minimised at

$$\langle H^\dagger H\rangle = \frac{v^2}{2}, \quad \langle\Phi^\dagger\Phi\rangle = \frac{f_a^2}{2}. \tag{3.5}$$

Working in the unitary gauge for the Higgs field and in polar parametrisation for the complex scalar,

$$H = \begin{pmatrix} 0 \\ \frac{\tilde{h}+v}{\sqrt{2}} \end{pmatrix}, \quad \Phi = \frac{\tilde{\chi} + f_a}{\sqrt{2}} e^{i\frac{a}{f_a}}, \tag{3.6}$$

where $(\tilde{\chi}, \tilde{h})$ denotes the gauge eigenstate, with $\langle h\rangle,\ \langle\chi\rangle = 0$. On this basis, the scalar mass matrix is not diagonal and takes the form

$$\mathcal{M}^2 \equiv V''\Big|_{\langle h\rangle, \langle\chi\rangle=0} = 2\begin{pmatrix} \lambda_H v^2 & \lambda_{H\Phi} v f_a \\ \lambda_{H\Phi} v f_a & \lambda_\Phi f_a^2 \end{pmatrix}, \tag{3.7}$$

which is positive definite under the conditions of Eq. (3.4). Diagonalising the mass matrix via an orthogonal transformation,

$$O^T \mathcal{M}^2 O = \mathrm{diag}(m_h^2, m_\chi^2), \qquad O = \begin{pmatrix} \cos(\theta) & \sin(\theta) \\ -\sin(\theta) & \cos(\theta) \end{pmatrix}, \tag{3.8}$$

the mass eigenvalue can be derived as

$$m_{h,\chi}^2 = \lambda_H v^2 + \lambda_\Phi f_a^2 \mp \sqrt{(\lambda_H v^2 - \lambda_\Phi f_a^2)^2 + (2\lambda_{H\Phi} f_a v)^2}\ . \tag{3.9}$$

The mass eigenstates (h, χ) are obtained by rotation,

$$\begin{pmatrix} h \\ \chi \end{pmatrix} = \begin{pmatrix} \cos(\theta) & -\sin(\theta) \\ \sin(\theta) & \cos(\theta) \end{pmatrix} \begin{pmatrix} \tilde{h} \\ \tilde{\chi} \end{pmatrix}, \tag{3.10}$$

with a mixing angle, from the off-diagonal relation in Eq. (3.8), given by

$$\begin{aligned} \tan(2\theta) &= \frac{2\lambda_{H\Phi} f_a v}{\lambda_\Phi f_a^2 - \lambda_H v^2}, \\ \cos(2\theta) &= \frac{\lambda_\Phi f_a^2 - \lambda_H v^2}{\sqrt{(\lambda_H v^2 - \lambda_\Phi f_a^2)^2 + (2\lambda_{H\Phi} f_a v)^2}}. \end{aligned} \tag{3.11}$$

Model parameters. At the Lagrangian level, the model is characterised by five parameters,

$$\lambda_H,\ \lambda_\Phi,\ \lambda_{H\Phi},\ v,\ f_a, \tag{3.12}$$

which determine the mass eigenvalues $m_h,\ m_\chi$ and the mixing angle θ. Different aspects of the theory are more naturally expressed in different parameter bases. EW constraints, for instance, are most conveniently formulated in terms of $\{m_h, m_\chi, \sin(\theta), v, \lambda_{H\Phi}\}$, whereas perturbativity

and vacuum stability analyses are better carried out based on $\{\lambda_H, \lambda_\Phi, v, f_a, \lambda_{H\Phi}\}$.
Using Eqs. (3.11) and (3.9), the latter can be expressed in terms of the former basis,

$$\begin{aligned}
\lambda_\Phi &= \frac{8\lambda_{H\Phi}^2}{\sin^2(2\theta)} \frac{v^2}{m_\chi^2 - m_h^2} \left(\frac{m_\chi^2}{m_\chi^2 - m_h^2} - \sin^2(\theta) \right), \\
\lambda_H &= \frac{m_h^2}{2v^2} \cos^2(\theta) + \frac{m_\chi^2}{2v^2} \sin^2(\theta), \\
f_a &= \frac{m_\chi^2 - m_h^2}{4v\lambda_{H\Phi}} \sin(2\theta).
\end{aligned} \tag{3.13}$$

Theoretical constraints. The theoretical constraints are the following,

- Vacuum stability: the potential must be bounded from below and must admit two non-trivial local minima, as required by the tree-level conditions in Eq. (3.4).
- Perturbative unitarity: following Refs. [54, 55], at the tree-level the partial wave amplitudes $a_j(s)$ of all possible $2 \to 2$ scattering processes satisfy $|Re(a_j(s))| \leq \frac{1}{2}$, which implies

$$\lambda_H, \ \lambda_\Phi, \ |2\lambda_{H\Phi}| \lesssim \frac{4\pi}{3}. \tag{3.14}$$

- EW vacuum stability: the presence of the new scalar modifies the stability analysis of the Higgs potential [53, 56].

RGE. The stability of the Higgs portal model under radiative corrections has been studied extensively in the literature [51], [56], [53].
The tree-level potential and couplings in Eq. (3.3) are understood as defined at the UV scale f_a. For the purpose of extracting qualitative estimates, it is sufficient to consider the scalar sector in isolation. The one-loop RGEs for the quartic couplings, valid above the mass of the heavier scalar, read [51]

$$\begin{aligned}
(4\pi)^2 \frac{d\lambda_H}{d\log(\mu)} &= 24\lambda_H^2 + 4\lambda_{H\Phi}^2, \\
(4\pi)^2 \frac{d\lambda_\Phi}{d\log(\mu)} &= 20\lambda_\Phi^2 + 8\lambda_{H\Phi}^2, \\
(4\pi)^2 \frac{d\lambda_{H\Phi}}{d\log(\mu)} &= 4\lambda_{H\Phi}(3\lambda_H + 2\lambda_\Phi) + 8\lambda_{H\Phi}^2.
\end{aligned} \tag{3.15}$$

3.1.1 Interactions in the mass eigenstate basis

In the parameter basis $\{m_h, m_\chi, \sin(\theta), v, \lambda_{H\Phi}\}$, the trilinear scalar potential, relevant for the phenomenology, is the following

$$V_{\text{trilinear}} = \frac{\kappa_{111}}{2} v h^3 + \frac{\kappa_{112}}{2} v \sin(\theta) h^2 \chi + \frac{\kappa_{221}}{2} v \sin(\theta) h \chi^2 + \frac{\kappa_{222}}{2} v \chi^3, \tag{3.16}$$

where the couplings κ, following the notation of [53], are given by

$$\begin{aligned}
\kappa_{111} &= \frac{m_h^2}{v^2\cos(\theta)}\left(\cos(\theta)^4 + \sin(\theta)^2\frac{2\lambda_{H\Phi}v^2}{m_h^2 - m_\chi^2}\right),\\
\kappa_{112} &= \frac{2m_h^2 + m_\chi^2}{v^2}\left(\cos(\theta)^2 + \frac{2\lambda_{H\Phi}v^2}{m_\chi^2 - m_h^2}\right),\\
\kappa_{221} &= \frac{2m_h^2 + m_\chi^2}{v^2}\left(\sin(\theta)^2 + \frac{2\lambda_{H\Phi}v^2}{m_h^2 - m_\chi^2}\right),\\
\kappa_{222} &= \frac{m_\chi^2}{v^2\sin(\theta)}\left(\sin(\theta)^4 + \cos(\theta)^2\frac{2\lambda_{H\Phi}v^2}{m_\chi^2 - m_h^2}\right).
\end{aligned} \tag{3.17}$$

When allowed kinematically, the trilinear sector mediates the decay $\chi \to hh$, at tree level,

$$\Gamma(\chi \to hh) = \frac{\sin^2(\theta)\kappa_{112}^2 v^2}{32\pi m_\chi}\sqrt{1 - \frac{4m_h^2}{m_\chi^2}}, \quad m_\chi > 2m_h. \tag{3.18}$$

The interaction of the radial mode χ with the SM fields arises from the rotation in Eq. (3.10). Those involving a tree-level single scalar in unitary gauge, in the fermion mass basis, are given by

$$\mathcal{L} \supset \frac{h\cos(\theta) + \chi\sin(\theta)}{v}\left[2m_W^2 W_\mu^+ W^{\mu-} + m_Z^2 Z_\mu Z^\mu - \sum_f m_f \bar{f} f\right], \tag{3.19}$$

where W, Z, f are the massive gauge boson and fermion of the SM. Thus, the couplings of χ into SM matter are universally suppressed by $\sin(\theta)$ with respect to those of pure SM Higgs.

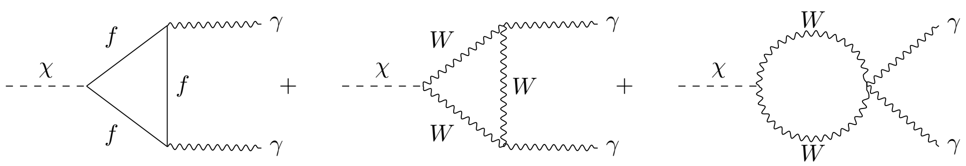

Figure 3.1: Feynman diagrams contributing to the $\chi\gamma\gamma$ effective operator

The couplings of χ with a massless gauge boson arise at one-loop, and in particular, we will consider the interaction with two photons $\chi\gamma\gamma$.
The effective Lagrangian operator for the Higgs interaction with two photons is known [57], then the derivation of the dimension five operators is completely analogous, from the Feynman diagram in Fig. 3.1,

$$\mathcal{L}_{\text{eff}} \supset -\frac{1}{4}\chi g_{\chi\gamma\gamma} F^{\mu\nu}F_{\mu\nu}, \tag{3.20}$$

with couplings suppressed by the mixing angle,

$$g_{\chi\gamma\gamma} = \sin(\theta) g_{h\gamma\gamma} = \sin(\theta)\frac{\alpha_{\text{em}}}{8\pi v}A_\gamma. \tag{3.21}$$

The canonical form for the factor A_γ is given by [57],

$$\begin{aligned}
A_\gamma &= \sum_f N_c^f Q_f^2 F_{\frac{1}{2}}(\tau_f) + F_1(\tau_W), \quad \tau_i \equiv \frac{4m_i^2}{m_\chi^2}, \\
F_{\frac{1}{2}}(\tau) &= -2\tau\left[1+(1-\tau)y(\tau)\right], \\
F_1(\tau) &= 2 + 3\tau + 3\tau(2-\tau)y(\tau)], \\
y(\tau) &= \begin{cases} \arcsin^2(\tau^{-\frac{1}{2}}) & \tau \geq 1 \\ -\frac{1}{4}\left[\log\left(\frac{1+\sqrt{1-\tau}}{1-\sqrt{1-\tau}}\right) - i\pi\right]^2 & \tau < 1, \end{cases}
\end{aligned} \tag{3.22}$$

where N_c^f is the color number of the fermion, ($N_c = 3$ for the quark, $N_c = 1$ for the lepton), and Q_f its electromagnetic charge. In the heavy particle limit $m_i \gg m_\chi$, the top quark and the W boson contributions dominate, and at leading order $A_\gamma \to \frac{47}{9}$.

At energy below the confinement scale Λ_{QCD}, physics is described in terms of hadrons. Using low-energy theorems [57], the effective coupling with nucleon $\chi\bar{N}N$ through the Higgs portal is given by

$$\mathcal{L} \supset g_{\chi NN}\, \chi\bar{N}N, \tag{3.23}$$

where

$$g_{\chi NN} = \sin(\theta)\frac{m_N}{v}\left[\sum_{q=u,..,t} f_q^N\right], \tag{3.24}$$

where f_q^N are the nuclear form factors, which can be estimated with lattice simulation or scattering matrix elements between the pion and the nucleon. From Ref. [58], the numerical value of the form factor is given by,

$$\sum_{q=u,..,t} f_q^N = 0.3\ . \tag{3.25}$$

3.2 Heavy radial mode $m_\chi \gg m_h$

In this section, we review the standard scenario in which the radial mode is expected to be heavier than the Higgs mode, with mass $m_\chi \gg m_h$. As discussed in Section 1.3, the non-observation of axion emission from stars constrains the PQ scale to $f_a > 10^8 - 10^9$ GeV [30], implying a huge separation of scale,

$$\frac{v}{f_a} \ll 10^{-6}. \tag{3.26}$$

Assuming order-unity Lagrangian couplings,

$$\lambda_H, \lambda_\Phi, \lambda_{H\Phi} \sim \mathcal{O}(1), \tag{3.27}$$

and expanding at leading order in the hierarchy $\frac{v}{f_a}$, the mass eigenvalues from Eq. (3.9) are given by

$$\begin{aligned}
m_h^2 &= 2\left(\lambda_H - \frac{\lambda_{H\Phi}^2}{\lambda_\Phi}\right)v^2 + \mathcal{O}\left(\frac{v^2}{f_a^2}\right), \\
m_\chi^2 &= 2\left(\lambda_\Phi + \frac{\lambda_{H\Phi}^2}{\lambda_\Phi}\frac{v^2}{f_a^2}\right)f_a^2 + \mathcal{O}\left(\frac{v^2}{f_a^2}\right),
\end{aligned} \tag{3.28}$$

where m_h corresponds to the mass of the SM Higgs boson and m_χ is the mass of the heavy radial mode. The hierarchy between the UV and IR scales gives rise to a highly suppressed mixing angle,

$$\sin(2\theta) = \frac{2\lambda_{H\Phi}}{\lambda_\Phi}\frac{v}{f_a} + \mathcal{O}\left(\frac{v^2}{f_a^2}\right). \tag{3.29}$$

Since $\sin(\theta)$ rules the strength of the interaction of the heavy scalar with the SM field content, a higher hierarchy implies a weakly coupled interaction.

Using an effective field theory approach, in the standard scenario $m_\chi \gg m_h$, the heavy field can be integrated out. At the tree-level, lead to a threshold correction to the Higgs quartic coupling,

$$V(H)_{\text{tree}} = \lambda\left(H^\dagger H - \frac{v^2}{2}\right)^2, \quad \lambda = \lambda_H - \frac{\lambda_{H\Phi}^2}{\lambda_\Phi}, \tag{3.30}$$

that does not vanish in the decoupling limit $\frac{v}{f_a} \to 0$. This has significant implications for the vacuum stability of the Higgs potential, as discussed in Ref. [56]. Nevertheless, it is worth noting that the 1-loop matching between the UV and IR theory at scale f_a, gives a contribution to the Higgs mass

$$\delta m_h^2 \sim \frac{\lambda_{H\Phi}}{16\pi^2} f_a^2, \tag{3.31}$$

and introduces a severe hierarchy problem if the portal coupling $\lambda_{H\Phi}$ is of order-unity.

3.3 Light radial mode $m_\chi \ll m_h$

Axion DM from parametric resonance [11], as well as in scenarios where the radial component itself constitutes DM, see Figs. 2.3, 2.7 require a light radial mass, $m_\chi \lesssim$ GeV. In this case, there are two independent hierarchies,

$$\frac{v}{f_a}, \frac{m_\chi}{m_h} \ll 1, \tag{3.32}$$

that will affect the parameter space. This is evident from the trace and the determinant of the mass matrix in Eq. (3.7),

$$\begin{aligned} \det(\mathcal{M}^2) &= 4\left(\lambda_H\lambda_\Phi - \lambda_{H\Phi}^2\right)v^2 f_a^2 = m_\chi^2 m_h^2, \\ \mathrm{Tr}(\mathcal{M}^2) &= 2\lambda_H v^2 + 2\lambda_\Phi f_a^2 = m_\chi^2 + m_h^2. \end{aligned} \tag{3.33}$$

From the determinant condition, we can express the combination of couplings parametrically,

$$\left(\lambda_H\lambda_\Phi - \lambda_{H\Phi}^2\right) = \frac{m_\chi^2 m_h^2}{v^2 f_a^2} \simeq 10^{-16}\left(\frac{m_\chi}{\text{GeV}}\right)^2\left(\frac{10^8\text{GeV}}{f_a}\right)^2. \tag{3.34}$$

where in the last step we have used that the Higgs mass is of the order of the EW scale, $m_h \sim v$. The system retains one free parameter, but we can assume that

$$\lambda_H \sim \mathcal{O}(1), \tag{3.35}$$

for two reasons: in the limit $\lambda_{H\Phi} \to 0$ the SM must be recovered, and λ_H receives at one-loop contributions from the top-Yukawa coupling, and is therefore not protected against radiative corrections if taken to be small.
From the determinant relation (3.33), two distinct regimes solve the system:

- A fine-tuned regime: a near-cancellation among the parameters,

$$\lambda_H \lambda_\Phi \sim \lambda_{H\Phi}^2 + \mathcal{O}\left(\frac{m_\chi^2 m_h^2}{v^2 f_a^2}\right), \tag{3.36}$$

  that is in tension with the constraint in Eq. (3.4). The trace equation requires, using $\lambda_H \simeq \mathcal{O}(1)$, that $\lambda_\Phi \lesssim \frac{v^2}{f_a^2}$, so that $\lambda_H v^2 \gtrsim \lambda_\Phi f_a^2$. In this regime, the mixing angle satisfies, from Eq. (3.11),

$$|\tan(2\theta)| \simeq \frac{2|\lambda_{H\Phi}|}{\lambda_H}\frac{f_a}{v} \simeq \sqrt{\frac{\lambda_\Phi}{\lambda_H}}\frac{f_a}{v} \lesssim \mathcal{O}(1). \tag{3.37}$$

  Although the mixing angle can be of the order of unity, this configuration is not radiatively stable, as discussed in Section 3.3.1.

- The most "natural" regime: avoid fine-tuning and requiring a well-defined potential implies

$$\lambda_H \lambda_\Phi \sim \frac{m_\chi^2 m_h^2}{v^2 f_a^2}, \ \lambda_{H\Phi}^2 \ll \lambda_H \lambda_\Phi. \tag{3.38}$$

  With $\lambda_H \sim \mathcal{O}(1)$ and $\lambda_\Phi \sim \frac{m_\chi^2}{f_a^2}$, the trace relation is automatically satisfied, leading to a small mixing coupling,

$$|\lambda_{H\Phi}| \ll \frac{m_\chi}{f_a}. \tag{3.39}$$

  The mixing angle is suppressed,

$$|\tan(2\theta)| \simeq \frac{2|\lambda_{H\Phi}|}{\lambda_H}\frac{f_a}{v} \ll \frac{m_\chi}{m_h}, \tag{3.40}$$

  where in the last step, we have used $v \sim m_h$. This solution is radiatively stable, as is shown in the following Section 3.3.1.

Both solutions require either a severe fine-tuning or very small couplings, a direct consequence of the double hierarchy in the parameter space.

3.3.1 Radiative stability

In the light radial scenario, at the scale f_a, the two hierarchies admit two regimes: either a strong fine-tuning among the couplings or very small couplings, while both require

$$\lambda_\Phi(f_a), \ \lambda_{H\Phi}(f_a) \ll 1. \tag{3.41}$$

Radiative corrections can destabilise fine-tuned configurations by generating loop contributions that substantially alter the potential's structure.
From the RGEs in Eq. (3.15), in both parameter configurations, the couplings remain stable under radiative corrections,

- $\lambda_{H\Phi}$ renormalises multiplicatively, so it never changes sign and remains perturbatively small.
- The RGE of the Higgs quartic λ_H gets a negligible contribution from $\lambda_{H\Phi}$, since $\lambda_{H\Phi} \ll \lambda_H$.

- The RGE of the PQ quartic λ_Φ gets a contribution from $\lambda_{H\Phi}$, however it is stable, since $\lambda_{H\Phi}^2 \lesssim \lambda_H\lambda_\Phi$.

With this simple argument, we can assume both the mixing and quartic couplings stable in the renormalisation-group running from f_a down to v scale.

However, the combination $\lambda_H(\mu)\lambda_\Phi(\mu) - \lambda_{H\Phi}^2(\mu)$ is not protected by any symmetry and receives the following one-loop contribution:

$$(4\pi)^2 \frac{d}{d\log(\mu)} \left(\lambda_H\lambda_\Phi - \lambda_{H\Phi}^2\right) = 24\lambda_H^2\lambda_\Phi + 20\lambda_H\lambda_\Phi^2 - 16\lambda_H\lambda_{H\Phi}^2 - 12\lambda_\Phi\lambda_{H\Phi}^2 - 16\lambda_{H\Phi}^3. \quad (3.42)$$

If this combination is radiatively unstable, then the combination of physical masses receives loop corrections that exceed the tree-level values.

In the fine-tuned regime, the initial conditions are the following.

$$\lambda_H(f_a)\lambda_\Phi(f_a) \sim \lambda_{H\Phi}^2(f_a), \qquad \lambda_\Phi(f_a) \lesssim \frac{v^2}{f_a^2}, \quad \lambda_H(f_a) \sim \mathcal{O}(1), \quad (3.43)$$

and the dominant loop contribution is proportional to $\lambda_H^2\lambda_\Phi$. So, the one-loop contribution at the scale v, with respect to the tree-level value at f_a given in Eq. (3.34), is roughly the following,

$$\frac{\delta_{1L}\left(\lambda_H\lambda_\Phi - \lambda_{H\Phi}^2\right)(v)}{(4\pi)^2\left(\lambda_H\lambda_\Phi - \lambda_{H\Phi}^2\right)(f_a)} \propto \frac{\lambda_H^2(v)\lambda_\Phi(v)}{(4\pi)^2}\left(\frac{f_a^2}{m_\chi^2}\right) \sim \frac{1}{(4\pi)^2}\left(\frac{m_h^2}{m_\chi^2}\right) \gg 1, \quad (3.44)$$

where we have used the stability assumption of the quartic couplings $\lambda_\Phi(v) \lesssim v^2/f_a^2$. Consequently, as soon as the renormalisation scale is lowered below f_a, the potential will change significantly around the minimum.

In the most natural regime, when

$$\lambda_H(f_a) \sim \frac{m_h^2}{v^2} \sim \mathcal{O}(1), \quad \lambda_\Phi(f_a) \sim \frac{m_\chi^2}{f_a^2}, \quad \lambda_{H\Phi}^2(f_a) \ll \lambda_H(f_a)\lambda_\Phi(f_a), \quad (3.45)$$

the leading contribution is subdominant, considering the large logarithm contribution from the RGE,

$$\frac{\delta_{1L}\left(\lambda_H\lambda_\Phi - \lambda_{H\Phi}^2\right)(v)}{(4\pi)^2\left(\lambda_H\lambda_\Phi - \lambda_{H\Phi}^2\right)(f_a)} \propto \frac{\lambda_H^2(v)\lambda_\Phi(v)}{(4\pi)^2\lambda_H(f_a)\lambda_\Phi(f_a)}\ln\left(\frac{v^2}{f_a^2}\right) \sim \frac{\lambda_H(f_a)}{(4\pi)^2}\ln\left(\frac{v^2}{f_a^2}\right) < 1, \quad (3.46)$$

manifesting radiative stability.

Instead, the beta function of the mass receives a contribution from the heavy mass, which could be radiatively unstable even if $\lambda_{H\Phi}^2 \ll \lambda_H\lambda_\Phi$. Using NDA in dimensional regularisation,

$$(4\pi)^2 \frac{dm_\chi^2}{d\log(\mu)} \propto \lambda_{H\Phi}m_h^2 + \mathcal{O}\left(\lambda_{H\Phi}^2 m_h^2, \lambda_\Phi^2 m_\chi^2\right). \quad (3.47)$$

However, looking at the parameter space in Fig. 2.3, 2.7, and also for axion DM from parametric resonance [11], the scenario $\lambda_{H\Phi}^2 \ll \lambda_H\lambda_\Phi$ implies $\lambda_{H\Phi}m_h^2 \ll m_\chi^2$.

Given that the natural regime is the only radiatively stable solution, throughout this thesis, we adopt the parameter assignment

$$\lambda_\Phi \sim \frac{m_\chi^2}{f_a^2}, \quad \lambda_H \sim \mathcal{O}(1), \quad |\lambda_{H\Phi}| \ll \sqrt{\lambda_H \lambda_\Phi}, \tag{3.48}$$

which, as follows from Eq. (3.40), implies a strongly suppressed scalar mixing angle,

$$|\sin(2\theta)| \ll \frac{m_\chi}{m_h}, \tag{3.49}$$

with direct consequences for the phenomenological constraints discussed in Chapter 4.

However, the stability of the potential has to be ensured below the EW scale too, where integrating out the Higgs boson can lead to instability in the low-energy description. At tree-level from the potential in Eq. (3.3), neglecting the derivative contribution, the equation of motion for the Higgs doublet is

$$\left(H^\dagger H - \frac{v^2}{2}\right) + \frac{\lambda_{H\Phi}}{\lambda_H}\left(\Phi^\dagger \Phi - \frac{f_a^2}{2}\right) = 0. \tag{3.50}$$

Inserting into the original potential, we arrived at the following form,

$$V_{IR} = \lambda_{PQ}\left(\Phi^\dagger \Phi - \frac{f_a^2}{2}\right)^2, \quad \lambda_{PQ} = \lambda_\Phi - \frac{\lambda_{H\Phi}^2}{\lambda_H}, \tag{3.51}$$

that is the potential that we have used for the discussion of DM in (2.1). At tree-level, the condition $\lambda_{H\Phi}^2 < \lambda_H \lambda_\Phi$ guarantees $\lambda_{PQ} > 0$, so the IR potential remains bounded from below after integrating out the Higgs. At one-loop, a potentially dangerous correction can arise at the matching scale $\mu = v$. In the small angle limit,

$$|\sin(2\theta)| \ll 1, \tag{3.52}$$

the leading contributions in NDA to the mass and quartic term of the low-energy theory at the matching scale are

$$\begin{aligned} \lambda_{PQ}(v) &\propto \lambda_\Phi - \frac{\lambda_{H\Phi}^2}{\lambda_H} + \frac{\lambda_{H\Phi}^2}{16\pi^2}\log\left(\frac{v}{f_a}\right) + \frac{\lambda_\Phi^2}{16\pi^2}\log\left(\frac{v}{f_a}\right), \\ m_{IR}^2(v) &\propto \left(\lambda_\Phi - \frac{\lambda_{H\Phi}^2}{\lambda_H}\right) f_a^2 + \frac{\lambda_{H\Phi}}{16\pi^2} m_h^2 + \frac{\lambda_{H\Phi}^2}{16\pi^2} m_h^2 + \frac{\lambda_\Phi^2}{16\pi^2} m_\chi^2. \end{aligned} \tag{3.53}$$

Then, in the regime $\lambda_{H\Phi}^2 \ll \lambda_H \lambda_\Phi$ the leading correction from the mixing is the linear term in $\lambda_{H\Phi}$. The ratio with respect to the tree-level mass gives,

$$\frac{|\lambda_{H\Phi}| m_h^2}{16\pi^2 \lambda_\Phi f_a^2} \ll \frac{\sqrt{\lambda_H}}{16\pi^2}\frac{m_h}{m_\chi}\frac{m_h}{f_a} < 1. \tag{3.54}$$

The last inequality is automatically satisfied from the open parameter space in the case of radial DM, in Figs. 2.3, 2.7, and also for axion DM from parametric resonance [11].

3.4 Technically natural light radial mode

In this thesis, we have discussed how a light radial mode can be dynamically relevant, but necessary requires $m_\chi \ll f_a$. Furthermore, in the light Scalar-Higgs portal model, the fact that $m_\chi \ll m_h$ implies a small mixing coupling, $|\lambda_{H\Phi}| \ll \frac{m_\chi}{f_a}$. From a purely pragmatic standpoint, small values are not forbidden; However, it is more pleasant to trace their origin from an underlying symmetry.

In this section, we will discuss the technical naturalness of the light radial mode, first in the DM sector of Eq. (2.1), then in the presence of a Scalar-Higgs portal interaction of Eq. (3.3). The definition of technical naturalness is based on the 't Hooft naturalness criterion [59]:
at any energy scale μ, a physical parameter or set of physical parameters $\alpha_i(\mu)$ is allowed to be very small only if the replacement $\alpha_i(\mu) = 0$ increases the symmetry of the system.

Consider the infrared tree-level action for the PQ complex scalar field, from Eq. (2.1),

$$S = \int d^4x \left[-\partial_\mu \Phi^\dagger \partial^\mu \Phi + m_\chi^2 \Phi^\dagger \Phi - \lambda_{PQ} (\Phi^\dagger \Phi)^2 \right]. \tag{3.55}$$

Under coordinate rescaling,

$$x_\mu \to \eta\, x'_\mu, \tag{3.56}$$

the action transforms as

$$S = \int d^4x' \left[-\eta^2\, \partial_{\mu'} \Phi^\dagger \partial^{\mu'} \Phi + \eta^4 m_\chi^2 \Phi^\dagger \Phi - \eta^4 \lambda_{PQ} (\Phi^\dagger \Phi)^2 \right]. \tag{3.57}$$

Performing the field redefinition $\Phi(x') \to \Phi(x')\eta^{-1}$, which restores canonical normalisation of the kinetic term, the action becomes

$$S = \int d^4x' \left[-\partial_{\mu'} \Phi^\dagger \partial^{\mu'} \Phi + \eta^2 m_\chi^2 \Phi^\dagger \Phi - \lambda_{PQ} (\Phi^\dagger \Phi)^2 \right]. \tag{3.58}$$

In the massless limit $m_\chi \to 0$, the classical scale invariance is restored. So in the pure PQ potential, the light radial is technically natural.

In our setup, the UV completion of the action in Eq. (3.55) emerges at the EW scale v, where the scalar Φ couples to the Higgs doublet H through the Higgs-portal interaction. Thus, in dimensional regularisation, the beta function for the light scalar mass now receives a new contribution:

$$\beta_{m_\chi^2} \propto \lambda_\Phi(\mu) m_\chi^2(\mu) + \lambda_{H\Phi}(\mu) m_h^2(\mu). \tag{3.59}$$

Since $m_h \gg m_\chi$, the second term generically drives the light scalar mass towards the EW scale when values are given by $\lambda_{H\Phi} \sim \mathcal{O}(1)$.
The hierarchy $\frac{m_\chi^2}{m_h^2} \ll 1$ can therefore remain stable under RG evolution only if $\lambda_{H\Phi} \ll \frac{m_\chi^2}{m_h^2}$.
In other words, the light radial mode in the Higgs portal model is technically natural if $\lambda_{H\Phi} \to 0$.

The remaining question is whether the smallness of $\lambda_{H\Phi}$ can itself be justified by a symmetry argument. In the Higgs portal framework, taking the decoupled limit $\lambda_{H\Phi} \to 0$ enhances the Poincaré symmetry [60]. Indeed, for $\lambda_{H\Phi} = 0$, the action is factorised into two independent sectors,

$$S \stackrel{\lambda_{H\Phi}=0}{=} \int d^4x\ \mathcal{L}_\Phi(x) + \mathcal{L}_H(x). \tag{3.60}$$

Each sector is independently invariant under its own Poincaré transformation, so the symmetry group of the theory is enlarged from the diagonal $\mathcal{G}_P^{\Phi+H}$ to the direct product $\mathcal{G}_P^{\Phi} \otimes \mathcal{G}_P^{H}$.
This enhancement is particularly transparent at the level of the conserved Noether currents. In the decoupled theory, the total stress-energy tensor decomposes as

$$T_{\mu\nu}^{H+\Phi} \equiv T_{\mu\nu}^{\Phi} + T_{\mu\nu}^{H}, \tag{3.61}$$

where each contribution is independently conserved:

$$\partial^{\mu} T_{\mu\nu}^{\Phi} = \partial^{\mu} T_{\mu\nu}^{H} = 0. \tag{3.62}$$

Once the portal interaction is activated, $\lambda_{H\Phi} \neq 0$, the energy-momentum can flow between the two sectors, and only the total stress-energy tensor remains conserved. The independent conservation laws are therefore lost, and the symmetry is reduced to the diagonal subgroup. By the 't-Hooft criterion, a small value of $\lambda_{H\Phi}$ is therefore technically natural.

Finally, we emphasise that this argument strictly applies only in the absence of gravity. Gravitational interactions are universally coupled to the total stress-energy tensor and therefore inevitably mix the two sectors, even when $\lambda_{H\Phi} = 0$. The enhanced product Poincaré symmetry should therefore be regarded as only approximate, broken by gravitational effects suppressed by the Planck scale.

Chapter 4

Experimental constraints

In this chapter, we discuss the experimental constraints on the mixing angle of a light singlet scalar with the Higgs boson via the Scalar-Higgs interaction, discussed in Chapter 3. In particular, we will work in the small mixing angle regime, from Eq. (3.52),

$$|\sin(\theta)| \ll \frac{m_\chi}{m_h}. \tag{4.1}$$

From the open parameter space in Figs. 2.7, 2.3, and from the axion DM from parametric resonance [11], the mass range of interest for a light radial mode is

$$m_\chi \lesssim \text{GeV}. \tag{4.2}$$

4.1 χ decay modes

The radial mode can decay into two axions, calculated in Chapter 2, and the decay width of the radial mode into SM field content is the same as the Higgs, but $\sin^2(\theta)$ suppressed. If kinematically allowed, the possible decay channels for $m_\chi \lesssim$ GeV, at leading order are

$$\begin{aligned}
\Gamma(\chi \to \bar{f}f) &= \sin^2(\theta)\frac{G_F}{4\pi\sqrt{2}}N_c^f m_f^2 m_\chi \left(1 - 4\left(\frac{m_f^2}{m_\chi^2}\right)\right)^{\frac{3}{2}}, \quad f = e, \mu, u, d, s, \\
\Gamma(\chi \to aa) &= \frac{m_\chi^3}{16\pi f_a^2}\left(1 - \frac{2m_a^2}{m_\chi^2}\right)^2 \left(1 - 4\left(\frac{m_a^2}{m_\chi^2}\right)\right)^{\frac{1}{2}}, \\
\Gamma(\chi \to \gamma\gamma) &= \frac{g_{\chi\gamma\gamma}^2}{64\pi}m_\chi^3,
\end{aligned} \tag{4.3}$$

where N_c^f is the colour number of the fermion, m_f the fermion mass, and $g_{\chi\gamma\gamma}$ the couplings described in Eq. (3.21).

Instead, the light radial mode gives another decay channel for the Higgs, with a decay rate from the trilinear sector in Eq. (3.16),

$$\Gamma(h \to \chi\chi) = \frac{\sin^2(\theta)v^2}{32\pi m_h}\sqrt{1 - \frac{4m_\chi^2}{m_h^2}}\left(\frac{2m_h^2 + m_\chi^2}{v^2}\left(\sin^2(\theta) + \frac{2\lambda_{H\Phi}v^2}{m_h^2 - m_\chi^2}\right)\right)^2. \tag{4.4}$$

4.1.1 Survival of the radial condensate

In the presence of the Higgs portal, the new decay channels, apart from the axion discussed in Chapter 2, could spoil the homogeneous population. However, a full thermal history of the quartic with the Higgs portal is beyond the scope of this thesis. In this section, we will study the simpler case when the field is oscillating around the true vacuum.
For a radial DM population, with $m_\chi \lesssim$ MeV, the only kinematically allowed decay channel is two photons. The survival of the condensate requires that

$$\Gamma(\chi \to \gamma\gamma) < H_0. \tag{4.5}$$

Using Eqs. (4.3), (3.21), can be expressed parametrically as

$$\frac{m_\chi}{\text{MeV}} < 10^{-8}\left(\frac{H_0}{1.4\cdot 10^{-42}\text{GeV}}\left(\frac{v}{174\text{GeV}}\right)^2 (\sin(\theta)\alpha_{\text{em}}A_\gamma)^{-2}\right)^{\frac{1}{3}}. \tag{4.6}$$

With the experimental value for H_0, m_h, v, taking $\alpha_{\text{em}} \sim 1/137$, $A_\gamma \sim 47/9$, since m_W, $m_t \gg m_\chi$, the condensate survives if

$$m_\chi \lesssim \frac{10^{-7}}{\sin^{2/3}(\theta)}\ \text{MeV}. \tag{4.7}$$

Assuming as benchmark value the natural 't-Hooft regime, modulo order one factor,

$$|\sin(\theta)| \simeq 10^{-2}\cdot\frac{m_\chi}{m_h}. \tag{4.8}$$

the above relation is translated into, using $m_h \simeq 125$ GeV,

$$m_\chi < \text{MeV}. \tag{4.9}$$

The decay of the radial mode into two photons can be larger than the decay channel into two axions. Let us assume the axion to be massless; then it follows that

$$\frac{\Gamma(\chi \to \gamma\gamma)}{\Gamma(\chi \to aa)} \simeq \frac{\alpha_{em}^2 A_\gamma^2}{256\pi^2}\sin^2(\theta)\frac{f_a^2}{v^2}. \tag{4.10}$$

From the above equation, we find that, in general, the photon decay is dominant if

$$\frac{\Gamma(\chi \to \gamma\gamma)}{\Gamma(\chi \to aa)} > 1 \Longleftrightarrow \frac{m_\chi}{m_h} \geq |\sin(\theta)| \geq \frac{v}{f_a}\frac{16\pi}{\alpha_{\text{em}}A_\gamma}, \tag{4.11}$$

where the first inequality comes from the upper bound in the technically natural configuration (4.8). So, for a certain mass range, the observation of the scalar from the decay into two photons is favourable with respect to the two axions, and for the mass at which it is efficient, we expect a bound from the γ ray background.

The scattering of the radial field χ with particles in the thermal bath can, in principle, thermalise the radial mode condensate and erase the abundance of relics required for DM. As mentioned above, a full treatment of the thermalisation of the radial mode is beyond the scope of the thesis. We consider the regime when the radial mode condensate oscillates around f_a, as discussed in detail in the Appendix D. In the small mixing angle regime, scattering processes become efficient for the radial mode masses above

$$m_\chi \geq \text{MeV}. \tag{4.12}$$

4.2 Collider bounds

For $m_\chi \lesssim$ GeV, the dominant collider constraints arise from meson decays and beam-dump experiments.

- CHARM experiment [61]. The CHARM experiment at CERN used a 400 GeV proton beam on a copper target to produce Higgs-like scalars. The bound arises from the leptonic decay channels $\chi \to e^+e^-, \mu^+\mu^-$ whose rates are given in Eq. (4.3). CHARM places strong limits on $\sin^2(\theta)$ for scalar masses in the range of $m_\chi \sim 10 - 10^2\,$MeV.
- E949 experiment [62]. E949 experiments searched for rare kaon decay, also sensitive to $K \to \pi\chi$. The decay rate relevant for this process is

$$\Gamma(K \to \pi\chi) \sim \frac{\sin^2(\theta)}{16\pi m_K}\left(\frac{G_F}{16\pi^2}|V_{ts}^* V_{td}|\frac{m_t^2}{m_W^2}\right)^2 \left(m_K^2 - m_\pi^2\right)^2 , \tag{4.13}$$

  as computed in Ref. [63], where V_{ij} are the elements of the CKM matrix, G_F the Fermi constant. This places a strong constraint on the mixing angles for $m_\chi \lesssim m_K - m_\pi \sim$ 300 MeV.
- LHCb & Belle experiments [64, 65]. Both LHCb at CERN and Belle at KEK searched for the decay of a B-meson into a kaon and a light scalar that subsequently decays to a muon pair $B \to K^*\chi(\to \mu\mu)$. The effective rate for this process is factorised as $\mathrm{Br}(B \to K^*\mu\mu) \sim \mathrm{Br}(B \to K^*\chi) \cdot \mathrm{Br}(\chi \to \mu\mu)$, where $\Gamma(\chi \to \mu\mu)$ is computed in Eq. (4.3), and

$$\Gamma(B \to K^*\chi) \sim \frac{\sin^2(\theta)}{16\pi m_B}\left(\frac{G_F}{16\pi^2}|V_{ts}^* V_{tb}|\frac{m_t^2}{m_W^2}\right)^2 \left(m_B^2 - m_K^2\right)^2 . \tag{4.14}$$

Future sensitivity projections come from the DUNE experiment at Fermilab and from the SHiP experiment proposed at CERN. Both experiments are expected to significantly extend the reach of $\sin^2(\theta)$ for scalar masses $m_\chi \sim 10^8 - 10^9$ eV.
The resulting exclusion regions are shown in Fig. 4.3, where these constraints dominate for $m_\chi \sim 10^8 - 10^9$eV.

4.3 Astrophysical bounds

Light, weakly coupled particles can be efficiently produced in the hot and dense interiors of stars. Once produced, they may escape the stellar medium and thus carry away energy. Any anomalous energy loss would alter stellar evolution, so the absence of such deviations places stringent constraints on the couplings of new light degrees of freedom to SM particles. The Raffelt criterion [66] provides a simple and robust bound: new particles must not transport energy more efficiently than neutrinos. There are several stellar environments in which we are particularly sensitive to novel energy losses:

- Red Giant (RG) cores just before helium ignition and Horizontal Branch (HB) star cores during helium burning. The core consists of a degenerate electron plasma with fully ionized helium nuclei. The dominant radial mode production channel involves Compton and bremsstrahlung processes that involve $g_{\chi\bar{e}e}$. The bound was derived from Ref. [67].
- Core-collapse supernovae (SN). The supernova core is composed of dense nuclear matter, so the dominant radial production mechanism is instead nucleon-nucleon bremsstrahlung,

$$N + N \to N + N + \chi, \tag{4.15}$$

controlled by the $\chi\bar{N}N$ coupling. The observational bound comes from SN1987a: the resulting neutrino burst from core-collapse supernovae was measured for SN1987a in agreement with the SM. Due to significant uncertainty, SN constraints on new light particles should be treated as order-of-magnitude estimates. The bound was derived from Ref. [67].

- Neutron star cooling (NS). In cold neutron stars, the dominant production channel is again nucleon-nucleon bremsstrahlung $N + N \to N + N + \chi$, controlled by $g_{\chi\bar{N}N}$. The observational constraint is derived by comparing the predicted cooling curves with the measured ages and thermal luminosities of nearby isolated neutron stars. The bound was derived from Ref. [68].

4.4 Cosmological bounds

Effective late decays of light scalar particles can significantly affect the thermal and ionization history of the Universe. Consequently, radial mode decays that occur after recombination inject non-thermal photons into the cosmic medium, altering the observed photon distribution. The dominant bound comes from:

- Extragalactic background light (EBL). After recombination, nearly all free electrons are captured by nuclei, rendering the Universe transparent to radiation. Photons produced by late radial mode decays would propagate freely and contribute to the diffuse photon background. Since their energies differ from those of the thermal relic photons, they could in principle be detected as an excess in the EBL.
- Distortion of the CMB spectrum: Energy injection from radial mode decays can perturb the blackbody spectrum of the cosmic microwave background.

The resulting upper limits, illustrated in Fig. 4.2, on the mixing angle $\sin(\theta)$ are derived from Ref. [69]. For masses above the MeV scale, from Eq. (4.9) with not an extremely small mixing angle, the decay rate becomes efficient. Then the radial fields decay much earlier in the thermal history of the Universe. Consequently, bounds from the EBL and CMB are no longer applicable in this mass range.

4.5 Fifth-Force bounds

A light scalar χ coupled to nucleons with strength $g_{\chi\bar{N}N}$ mediates an additional long-range force between macroscopic bodies, supplementing Newtonian gravity with a Yukawa-type interaction. This new force is constrained principally by two classes of experiment that put stringent bounds for mass $m_\chi \lesssim 10^{-1}$ eV, as illustrated in Fig. 4.1.

Inverse-Square-Law (ISL) Tests. At tree level, χ exchange between two point masses m_1 and m_2 separated by a distance r generates a Yukawa correction to the Newtonian potential,

$$V(r) = -\frac{Gm_1m_2}{r}\left(1 + \alpha\, e^{-r/\lambda}\right), \tag{4.16}$$

where the force range is set by the Compton wavelength of the mediator, $\lambda = m_\chi^{-1}$. The dimensionless coupling strength relative to gravity is [70],

$$|\alpha| = \frac{g^2_{\chi\bar{N}N}}{4\pi G m_N^2} \simeq 8 \times 10^{30}\, \sin^2\theta, \tag{4.17}$$

where we used $g_{\chi\bar{N}N} \sim 8 \cdot 10^{-4} \sin\theta$ from Eq. (3.24), with θ the scalar mixing angle and $v \simeq 246$ GeV the Higgs VEV.
Torsion-balance experiments probe deviations from the $1/r$ behaviour of gravity at sub-millimetre to metre scales and are highly sensitive to Yukawa-type potentials of the form (4.16). They provide leading constraints on α for mediator masses in the range $m_\chi \sim 10^{-7}$–10^{-2} eV, corresponding to force ranges $\lambda \sim 10^{-4}$–10^{3} m. The experimental constraints are taken from Refs. [71–75].

Einstein Equivalence Principle (EEP) Tests. The Weak Equivalence Principle (WEP) states that the trajectory of a freely falling body is independent of its mass and internal composition [70]. A scalar coupled to nucleons through the Higgs portal violates this principle because the effective χ-nucleon coupling carries a residual composition dependence, and so $g_{\chi\bar{p}p} \neq g_{\chi\bar{n}n}$. As a result, two test bodies of different composition fall at different rates in the field sourced by χ exchange.

This differential acceleration is quantified by the Eötvös parameter,

$$\eta = 2\left|\frac{a_1 - a_2}{a_1 + a_2}\right|, \tag{4.18}$$

where a_1 and a_2 are the gravitational accelerations of two test masses that fall freely with different compositions toward a common source. An upper bound on η translates directly into an upper bound on the coupling $\sin^2(\theta)$ as a function of m_χ. The most precise bounds on η are provided by the Eöt-Wash torsion-balance experiment [76] and by the MICROSCOPE satellite mission [77].

4.6 Summary plot

4.6.1 Ultralight regime $m_\chi \lesssim 10^{-1}\,\mathrm{eV}$

In this regime, as seen in Fig. 4.1, the dominant bound arises from EEP and ISL tests. Assuming the technically natural regime of the mixing angle $\sin(\theta) \sim 10^{-1} - 10^{-2}\,\frac{m_\chi}{m_h}$, there is a favourable mass range for $m_\chi \lesssim 10^{-6}$ eV.

4.6.2 Intermediate regime $10^{-1}\,\mathrm{eV} \lesssim m_\chi \lesssim \mathrm{MeV}$

In this regime, as seen in Fig.4.2, the dominant bound depends on the mass range. Assuming the technically natural regime of the mixing angle $\sin(\theta) \sim 10^{-1} - 10^{-2}\,\frac{m_\chi}{m_h}$, there is a favourable mass range for $m_\chi \in [10^{-1}, 10^{2}]$ eV.

4.6.3 Heavy regime $\mathrm{MeV} \lesssim m_\chi \lesssim \mathrm{GeV}$

In this regime, as seen in Fig. 4.2, the dominant bounds arise from collider bounds and SN. Assuming the technically natural regime of the mixing angle $\sin(\theta) \sim 10^{-1} - 10^{-2}\,\frac{m_\chi}{m_h}$, there is a favourable mass range for $m_\chi \in [1 - 10]$ MeV. For the value of $\sin(\theta)$ in the figure, the late decay bound to photons is not present.

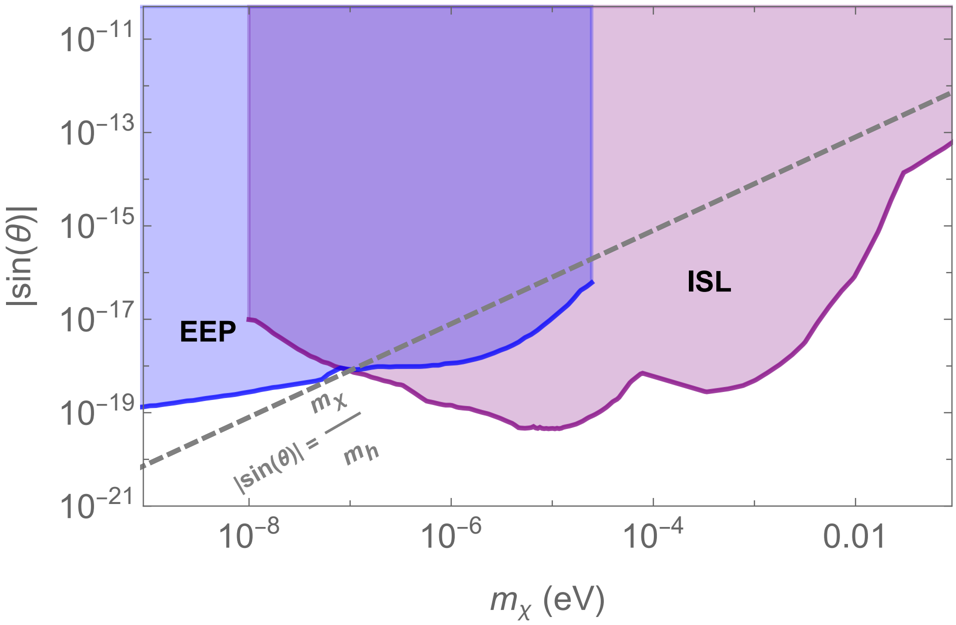

Figure 4.1: Experimental bounds on the mixing angle $\sin(\theta)$ in the ultralight regime $m_\chi \lesssim 10^{-1}$ eV. Dominant constraints arise from ISL and EEP tests. The region above $|\sin(\theta)| = m_\chi/m_h$ corresponds to an unstable scalar potential requiring fine-tuning. The figure is adapted from [78].

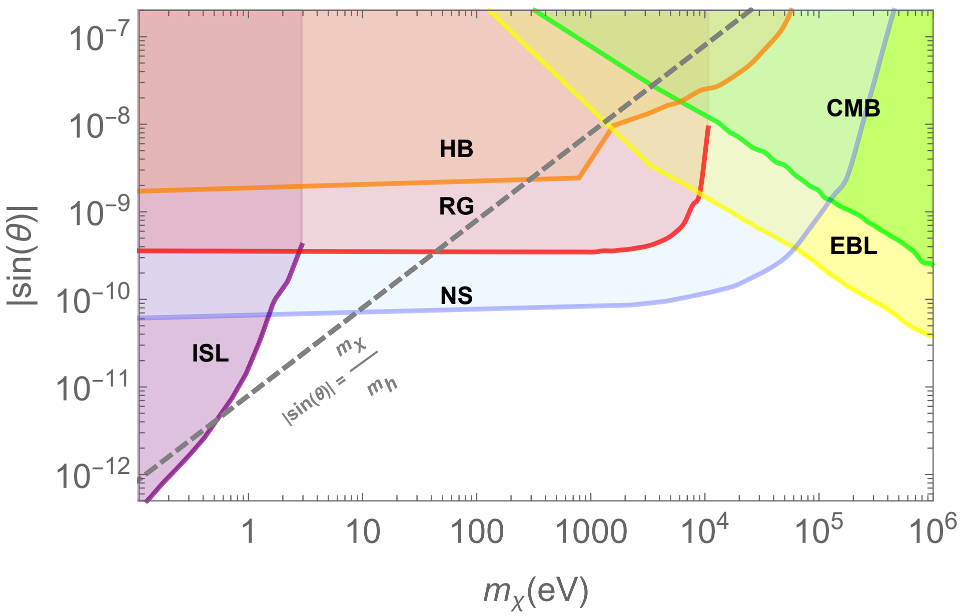

Figure 4.2: Experimental bounds on the mixing angle $\sin(\theta)$ in the intermediate regime 10^{-1} eV $\lesssim m_\chi \lesssim$ MeV. Dominant constraints from the ISL test, astrophysical bound NS,and the cosmological bound EBL. The region above $|\sin(\theta)| = m_\chi/m_h$ corresponds to an unstable scalar potential requiring fine-tuning. The figure is combined from Refs. [67, 68, 78].

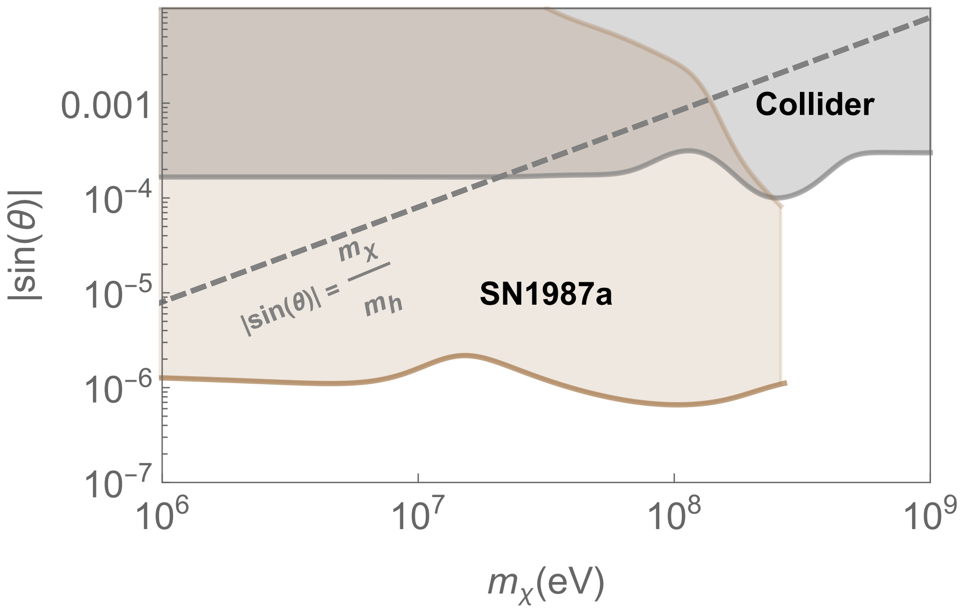

Figure 4.3: Experimental bound on the mixing angle $\sin(\theta)$ in the heavy regime MeV $\lesssim m_\chi \lesssim$ GeV. Dominant constraints from the collider bound and SN1987a. The region above $|\sin(\theta)| = m_\chi/m_h$ corresponds to an unstable scalar potential requiring fine-tuning. The figure is combined from Refs. [67, 79].

Conclusions

This thesis has explored the cosmological and phenomenological implications of a light radial mode in the framework of Co et al. [11].

The main results of Chapter 2 show how a large initial value of the PQ breaking field leads to the cosmological production of axions and radial quanta via parametric resonance. As illustrated in Fig. 2.7, there exist large regions of parameter space allowing the radial mode to constitute a fraction of DM, with $f_a \sim 10^8$–10^{12} GeV and a radial mass $m_\chi \lesssim \mathcal{O}(\text{MeV})$. To follow the non-linear dynamics, the ansatz of Ref. [11] on the population of particles produced by parametric resonance was adopted; the preliminary lattice simulation presented in Appendix A provides supporting numerical evidence for its validity. We have underlined the weakness of this setup: it requires an extremely small quartic coupling, $\lambda_{\text{PQ}} \ll 1$, and a large number of inflationary e-folds to realise the required initial conditions.

Despite these limitations, the scenario has remarkable properties. On the experimental side, several ongoing efforts are targeting the small-f_a window, such as IAXO [12], CAST [13] for solar axions, MADMAX [14], BREAD [15] for halo axions. From a theoretical perspective, a small decay constant also improves the PQ quality problem [30].

In Chapter 3 we discussed the minimal extension that communicates with the Standard Model via a Scalar-Higgs portal, assuming the hierarchy $m_\chi \ll v \ll f_a$, which constrains the structure of the Lagrangian parameters. Using radiative stability arguments, we defined a stable parameter regime and showed that a light scalar mass m_χ is technically natural. Together with the experimental constraints derived in Chapter 4, this allowed us to identify a preferred mass range for the radial mode.

Several directions remain open for future investigation. A systematic lattice study of the parametric resonance, going beyond the preliminary analysis of Appendix A, would allow a precise determination of axion and radial yields. The thermalisation history of the radial mode in the early stages of its evolution has not been fully addressed and deserves dedicated treatment. The smallness of λ_{PQ} calls for a dynamical mechanism that generates it naturally, e.g. an approximate symmetry. Finally, a light radial mode with the properties identified in this work may play a role in other open questions in Early Universe cosmology and particle physics beyond those explored here, making it a well-motivated target for future theoretical and experimental investigation.

Appendix A

Analytic and lattice analysis of parametric resonance

A.1 Introduction to parametric resonance

Parametric resonance is a phenomenon in vibration systems in which the vibration amplitude grows continuously due to periodic variations in system parameters, rather than from an external force, unlike ordinary resonance. For example, wind or vehicle-induced load fluctuations can alter the stiffness of long-span bridges, resulting in resonant vibrations.
Mathematically, this phenomenon is described by the Hill differential equation

$$\frac{dy^2}{dx^2} + f(x)y = 0, \tag{A.1}$$

where $f(x)$ is a function with minimal period T,

$$f(x+T) = f(x). \tag{A.2}$$

In particular, two sub-classes commonly appear in physical problems with resonance, Mathieu's equation, and Lamè's equation, where the former is a special case of the latter.

In our scenario, parametric resonance arises from the oscillating background field's effect on the fluctuations. So the main goal is to determine the parameter for which resonance is efficient. This problem naturally translates into analyzing the stability properties of the solutions, namely identifying the regions in parameter space where solutions remain bounded (stable) and those where they grow exponentially (unstable).

Mathieu's equation

We will recap the mathematical main results in the special case that can be easily generalised. For a complete mathematical derivation of this subject, refer to [29]. The Mathieu's equation has the general form, in terms of resonance parameters (α, q),

$$\frac{d^2x}{dt^2} + (\alpha - 2q\cos(2t))\,x = 0, \quad \alpha, q, t \in \mathbb{R},\ x \in \mathbb{C}. \tag{A.3}$$

For general values, there is no closed form. However, the (un)stability of the solutions is determined only by the pair (α, q), independently on the (non-trivial) initial condition.
This equation is associated with a 2-dimensional first-order system, defined

$$\dot{x} = y, \tag{A.4}$$

the equation takes the form

$$\dot{\mathbf{x}} = P(t)\mathbf{x}, \tag{A.5}$$

with

$$\mathbf{x} = \begin{pmatrix} x \\ y \end{pmatrix}, \quad P(t) = \begin{pmatrix} 0 & 1 \\ -\alpha + 2q\cos(2t) & 0 \end{pmatrix}. \tag{A.6}$$

The periodic matrix has minimal period π,

$$P(t + n\pi) = P(t), \quad n \in \mathbb{Z}. \tag{A.7}$$

The associated fundamental matrix has in the column the linearly independent solution of Eq. (A.5), which we can parameterize as

$$\Phi(t) = \begin{pmatrix} \phi_1(t) & \phi_2(t) \\ \dot{\phi}_1(t) & \dot{\phi}_2(t) \end{pmatrix}, \tag{A.8}$$

that satisfy

$$\dot{\Phi}(t) = P(t)\Phi(t). \tag{A.9}$$

This type of differential equation is well-known in the literature; here, we recall the main theorems to address the stability of the solution.
From Floquet's Theorem the regular system $\dot{\mathbf{x}} = P(t)\mathbf{x}$, where $P(t)$ is an $n \times n$ matrix function with minimal period T, has at least one non-trivial solution $\mathbf{x}_i(t)$ such that

$$\mathbf{x}_i(t + T) = e^{\mu_i T}\mathbf{x}_i(t), \quad \mu_i \in \mathbb{C}, \tag{A.10}$$

where μ_i is called a characteristic or Floquet exponent of the system.
In particular, it can be proven that if the solution has n distinct characteristic exponents, then the Eq. (A.5) has n linearly independent normal solutions of the form,

$$\mathbf{x}_i(t) = \mathbf{p}_i(t)\ e^{\mu_i t}, \tag{A.11}$$

which implies that $\mathbf{p}_i(t)$ has period T.
An unstable solution is characterised by at least one solution with

$$\mathcal{R}e(\mu_i) > 0, \tag{A.12}$$

which depends only on the values of α and q. In the case associated with Mathieu's equation,

$$\mathrm{tr}\{\mathbf{P}(t)\} = 0, \tag{A.13}$$

and using Liouville's theorem [29], we can relate the two charateristic exponent,

$$e^{(\mu_1+\mu_2)T} = \det(\Phi(0)^{-1}\Phi(\pi)) = e^{\int_0^\pi \mathrm{tr}\{\mathbf{P}(s)\}ds} = 1. \tag{A.14}$$

Then,

$$\mu_1 = -\mu_2 \equiv \mu, \tag{A.15}$$

and the form can be found by combining the previous relation with the fact that $e^{\mu_i T}$ is an eigenvalue of the monodromy matrix,

$$\det(\Phi(0)^{-1}\Phi(\pi) - e^{\mu_i T}\mathbb{I}_{2\times 2}) = 0. \tag{A.16}$$

This equation translates into a second-order differential equation

$$(e^{\mu_i T})^2 + e^{\mu_i T}\phi(\alpha, \beta) + 1 = 0, \tag{A.17}$$

where $\phi(\alpha, \beta)$ is a function of the parameter that, in general, does not have an analytic form. The solutions depend on the discriminant,

$$e^{\mu T}, e^{-\mu T} = \frac{1}{2}[\phi \pm \sqrt{\Delta}] \quad , \quad \Delta \equiv \phi^2 - 4. \tag{A.18}$$

Without explicitly specifying Δ, we can make the following deductions.

- $\Delta > 0$: μ is real, and the general solution can be expressed in the form,

$$x(t) = c_1 p_1(t) e^{\mu t} + c_2 p_2(t) e^{-\mu t}, \tag{A.19}$$

  where c_1, c_2 are the integration constant and p_1, p_2 have a minimal period π. The parameter region that satisfies $\Delta > 0$ contains unbounded solutions and is called the unstable parameter region.

- $\Delta < 0$: the characteristic exponents are purely imaginary, $\mu_1 = i|\mu| = -\mu_2$. All the solutions are bounded and are called the stable parameter region.

- $\Delta = 0$: In this case, there are no two different characteristic exponents, $\mu_1 = \mu_2 = 0$, since $|\phi| = 2$. From the Floquet theorem, one is a periodic solution, while the other is unbounded.

In particular, the instability/stability chart of Mathieu's equation can be calculated numerically, and the instability region, determined by α, q are illustrated in Fig. A.1.

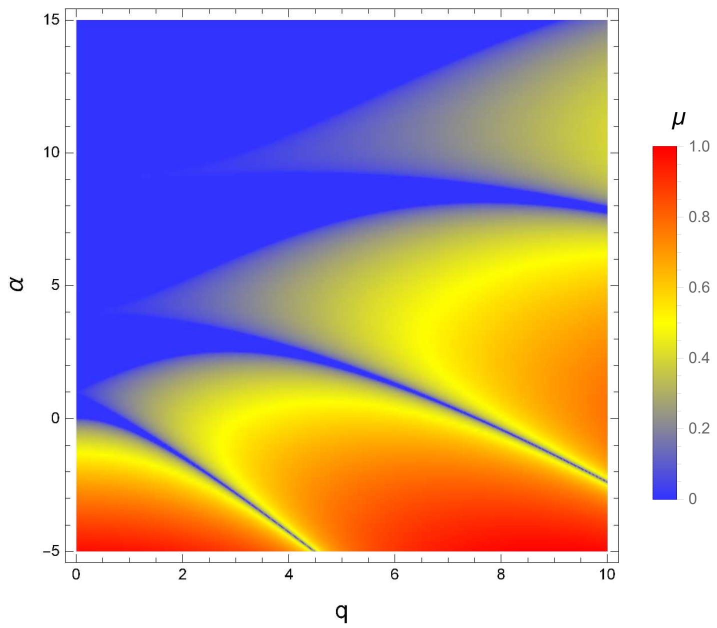

Figure A.1: Instability diagram for Mathieu's equation $\ddot{x} + (\alpha - 2q\cos(2t))x = 0$. The colour code (see the colour bar on the right-hand side of the plot) represents the value of the Floquet exponent $Re(\mu) \equiv \mu$. The blue regions correspond to fully stable solutions, the other regions, organized into distinct bands, correspond to unstable solutions. The chart is independent on the initial conditions.

Lamé equation

The Lamé's differential equation has the general form

$$\frac{d^2 x}{dz^2} + (\alpha + \beta \varrho(z))\, x = 0, \quad \alpha, q \in \mathbb{R}, \;\; x, \varrho, z \in \mathbb{C}, \tag{A.20}$$

where $\wp$ is a Weierstrass elliptic function, a complex function that is meromorphic and double periodic. In the parametric resonance, the most important cases correspond to a particular Weierstrass elliptic function, the Jacobi elliptic cosine, whose Lamé equation can be parametrised as

$$\frac{d^2x}{dz^2} + \left(\alpha + 2qk^2\mathrm{cn}^2(z,k)\right)x = 0. \tag{A.21}$$

Here, k is called the elliptic modulus that satisfies

$$0 < k < 1, \tag{A.22}$$

and $q, \alpha \in \mathbb{R}$ are the resonance parameter.
The Jacobi elliptic cosine $\mathrm{cn}(z,k)$ is a complex function defined implicitly through

$$z = \int_1^{\mathrm{cn}(z,k)} \frac{dy}{\sqrt{(1-y^2)(1-k^2-k^2y^2)}}, \tag{A.23}$$

that satisfies the following identities [80],

$$\begin{aligned} \mathrm{sn}^2(z,k) + \mathrm{cn}^2(z,k) &= 1, \\ \mathrm{cn}(z,0) &= \cos(z), \\ \mathrm{sn}(z,0) &= \sin(z), \end{aligned} \tag{A.24}$$

where $\mathrm{sn}(z,k)$ is the Jacobi elliptic sine. The Jacobi cosine is double periodic with

$$\mathrm{cn}(z + 2mK + 2niK', k) = (-1)^{m+n}\mathrm{cn}(z,k), \quad m, n \in \mathbb{Z}, \tag{A.25}$$

where $K(k), K'(k)$ are the complete elliptic integral of the first kind, with $K(k') \equiv K'(k)$, $k' = \sqrt{1-k^2}$ and

$$K(k) = \int_0^1 \frac{dy}{\sqrt{(1-y^2)(1-k^2y^2)}}. \tag{A.26}$$

From the Schwartz reflection principle

$$\overline{\mathrm{cn}(z,k)} = \mathrm{cn}(\bar{z},k), \tag{A.27}$$

evaluating the function on the real axis implies that $\mathrm{cn}(z,k)$ is real with period $4K(k)$ as seen in Eq. (A.25).
This solution has the same stability/instability discussion as in the previous chapter; in particular, in the $k \to 0$ limit, the two are related. Taking a specific elliptic modulus $k = \frac{1}{\sqrt{2}}$, the stability/instability band can be seen in Fig. A.2.

A.2 Parametric resonance in a $\lambda\phi^4$ model

In this first model, we will discuss the effect of parametric resonance in a simple scalar field theory, compare the lattice with the analytical result, and underscore the characteristic feature of this mechanism in a radiation-dominated universe.

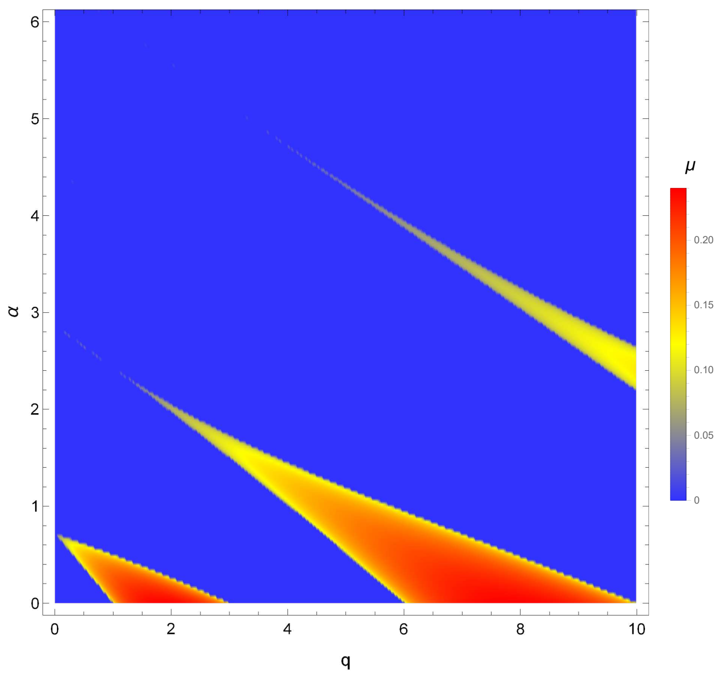

Figure A.2: Instability diagram for Lamé's equation $\ddot{x} + (\alpha + q\mathrm{cn}^2(z, \frac{1}{\sqrt{2}}))x = 0$. The colour code (see the colour bar on the right-hand side of the plot) represents the real value of the Floquet exponent μ. The blue regions correspond to fully stable solutions, the other regions, organized into distinct bands, correspond to unstable solutions.

A.2.1 Linear analysis

Consider a scalar potential with a quartic interaction

$$V(\phi) = \frac{\lambda}{4}\phi^4, \tag{A.28}$$

the equation of motion for the scalar field in a fixed FLRW background, derived from Eq. (2.6)

$$\ddot{\phi} + 3H\dot{\phi} - \frac{\nabla^2}{R^2}\phi + \lambda\phi^3 = 0. \tag{A.29}$$

Splitting the field in the homogeneous field and the fluctuation,

$$\phi(t, \vec{x}) = \phi_0(t) + \delta\phi(t, \vec{x}). \tag{A.30}$$

We will assume that at the initial time t_i, the condensate is the dominant component,

$$\frac{\langle\phi^2\rangle}{\phi_0^2}(t_i) = 1, \tag{A.31}$$

with some amplitude;

$$\phi(t_i, \vec{x}) = \phi_0(t_i) \equiv \phi_i, \;\; \dot{\phi}(t_i, \vec{x}) = 0. \tag{A.32}$$

Then the equation of motion at linear order can be split as,

$$\ddot{\phi}_0 + 3H\dot{\phi}_0 + \lambda\phi_0^3 = 0 + \mathcal{O}(\phi_0^2\delta\phi), \quad \delta\ddot{\phi} + 3H\delta\dot{\phi} - \frac{\nabla^2}{R^2}\delta\phi + 3\lambda\phi_0^2\delta\phi = 0 + \mathcal{O}(\phi_0\delta\phi^2). \tag{A.33}$$

The fluctuation of the scalar field, at the linear order, acquires an effective mass that, in general, is a function of ϕ_0. If the condensate oscillates, then parametric resonance enters the equation

of motion for the fluctuation.
We define the initial time t_i and the initial effective mass term for the homogeneous mode as,

$$H(t_i) = w_i, \quad w_i \equiv \sqrt{\lambda \phi_i^2}. \tag{A.34}$$

Making a convenient conformal transformation of the time and field variables

$$\vec{x} \to \vec{y} \equiv w_i \vec{x}, \quad t \to z \equiv w_i \eta, \quad \eta \equiv \int \frac{dt}{R(t)}, \tag{A.35}$$

$$\delta\phi \to f \equiv R\frac{\delta\phi}{\phi_i}, \quad \phi_0 \to X \equiv R\frac{\phi_0}{\phi_i}, \tag{A.36}$$

In a radiation-dominated epoch, normalising the scale factor such that $R(t_i) = 1$,

$$R = R(t_i)\sqrt{\frac{t}{t_i}} = 1 + (z - z_i), \quad R'' = 0, \tag{A.37}$$

the equation of motion at linear order becomes

$$X'' + X^3 = 0 + \mathcal{O}(X^2 f), \quad f'' - \nabla_{\vec{y}}^2 f + 3X^2 f = 0 + \mathcal{O}(X f^2), \quad {}' \equiv \frac{d}{dz}. \tag{A.38}$$

In these variables, the equations of motion are reduced to flat spacetime, because ϕ^4 is conformally invariant in a conformally flat background geometry. The equation of motion of the conformal homogeneous mode admits an integral of motion, the energy conservation,

$$\frac{d}{dz}\left(\frac{X'^2}{2} + \frac{X^4}{4}\right) = 0. \tag{A.39}$$

The Cauchy boundary conditions at $z(t_\mathrm{i}) \equiv z_\mathrm{i}$, recalling that $\phi_i = \phi(t_i)$, $\dot{\phi}(t_i) = 0$, and normalize the scale factor such that $R(t_i) = 1$,

$$X(z_\mathrm{i}) = R(z_i)\frac{\phi_0(z_i)}{\phi_i} = 1, \quad X'(z_\mathrm{i}) = \frac{R(t_i)}{w_i \phi_i}\frac{d}{dt}\left(\phi_0 R\right)\Big|_{t=t_\mathrm{i}} = \frac{H_i}{w_i}. \tag{A.40}$$

We can define t_i as the onset of oscillation for the physical field $\phi_0(t)$, where $H_i = w_i$, so that

$$\frac{X'^2}{2} + \frac{X^4}{4} = \frac{X_i'^2}{2} + \frac{X_i^4}{4} = \frac{3}{4}. \tag{A.41}$$

Then, using the method of separation of variables,

$$z - z_i = \sqrt{2}\int_1^{X(z)} \frac{dX}{\sqrt{3 - X^4}}. \tag{A.42}$$

The right side can be rewritten as a Jacobi elliptic cosine A.23, by changing variables

$$w \equiv \frac{X}{3^{\frac{1}{4}}}, \tag{A.43}$$

$$\int_1^{X(z)} \frac{dX}{\sqrt{3 - X^4}} = \frac{1}{\sqrt{3}}\int_{3^{-\frac{1}{4}}}^{w(z)} \frac{dw}{\sqrt{1 - w^4}} = \frac{1}{\sqrt{3}}\int_{3^{-\frac{1}{4}}}^{w(z)} \frac{dw}{\sqrt{(1 - w^2)\left(1 - \frac{1}{2} + \frac{1}{2}w^2\right)}}. \tag{A.44}$$

The elliptic modulus is $k = 1/\sqrt{2}$ and does not depend on the initial condition. With respect to the Elliptic cosine in Eq. (A.23), the lower bound of the integral is different from unity, so after a further manipulation, the final result is

$$X(z) = 3^{\frac{1}{4}}\text{cn}\left(3^{\frac{1}{4}}(z - z_i) - cn^{-1}\left(3^{-\frac{1}{4}}, \frac{1}{\sqrt{2}}\right)\ , \frac{1}{\sqrt{2}}\right). \tag{A.45}$$

The solution is illustrated in Figure A.3 and, as discussed in (A.25), is periodic,

$$X(z + T) = X(t), \quad T = \frac{4}{3^{\frac{1}{4}}}K\left(\frac{1}{\sqrt{2}}\right) = 5.6, \tag{A.46}$$

where $K(k)$ stands for the complete elliptic integral of the first kind, which can be computed numerically.

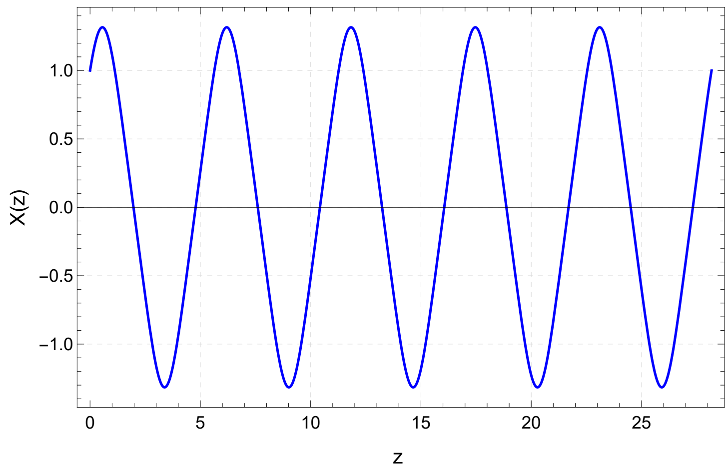

Figure A.3: The oscillatory solution of the homogeneous mode in Eq.(A.38), in rescale conformal time $z = w_i\eta$ with $X(z_i) = 1,\ X'(z_i) = 1, z_i = 0$.

This oscillatory background sources the parametric resonance of the fluctuation. Quantising the fluctuation in Fourier space,

$$f(z, \vec{y}) = \int \frac{d^3\vec{\kappa}}{(2\pi)^3}\left(e^{i\vec{\kappa}\vec{y}}\ \ b_\kappa f_\kappa(z) + e^{-i\vec{\kappa}\vec{y}}\ b^\dagger_\kappa f^*_\kappa(z)\right), \tag{A.47}$$

the background homogeneous field enters the equation of motion of the fluctuation,

$$f''_\kappa + \left(\kappa^2 + 3X^2\right) f_\kappa = 0, \quad ' \equiv \frac{d}{dz}. \tag{A.48}$$

Since we are at linear order, each mode evolves independently. Rescaling the time variable,

$$z \to 3^{\frac{1}{4}}(z - z_i) - cn^{-1}\left(3^{-\frac{1}{4}}, \frac{1}{\sqrt{2}}\right), \tag{A.49}$$

the differential equation is precisely the Lamè equation in Eq. A.21,

$$f''_\kappa + \left(\frac{\kappa^2}{\sqrt{3}} + 3\text{cn}^2\left(z, \frac{1}{\sqrt{2}}\right)\right) f_\kappa = 0, \tag{A.50}$$

with the resonance parameters

$$q = 3, \quad \alpha = \frac{\kappa^2}{\sqrt{3}}. \tag{A.51}$$

Thus, the mode equation has reduced to the flat case, but with a frequency $w_k(z)$ that depends on the dimensionless conformal time,

$$w_\kappa^2(z) \equiv \frac{\kappa^2}{\sqrt{3}} + 3\mathrm{cn}^2\left(z, \frac{1}{\sqrt{2}}\right). \tag{A.52}$$

If the initial conditions are not trivial, i.e., at z_i, $f_\kappa(z_i) \neq 0$ or $f'_\kappa(z_i) \neq 0$, the range of the mode function in the unstable regime exhibits an exponential growth in rescaled time, as illustrated in Fig. A.6. In particular, the unstable solutions satisfy the following conditions,

$$f_\kappa(z) \propto e^{\mu_\kappa z}, \qquad 1.6 \lesssim \kappa \lesssim 1.75, \quad \mu_k^{\max} \sim 0.036, \tag{A.53}$$

as illustrated in Fig. A.4.

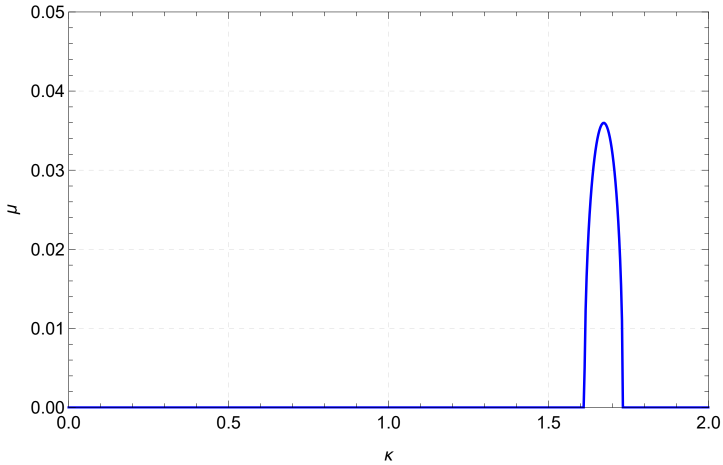

Figure A.4: Floquet exponent for Lamé's equation $f''_\kappa + (\frac{\kappa^2}{\sqrt{3}} + 3\mathrm{cn}^2(z, \frac{1}{\sqrt{2}}))f_\kappa = 0$. Regions with $\mu_\kappa > 0$ are unstable, with solution $f_\kappa(z) \propto e^{\mu z}$.

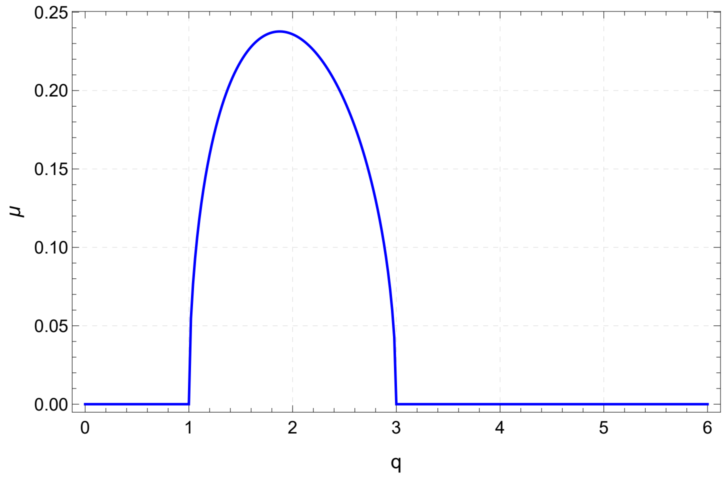

Figure A.5: Floquet exponent for Lamé's equation $x'' + (0 + q\mathrm{cn}^2(z, \frac{1}{\sqrt{2}}))x = 0$. Regions with $\mu_{\kappa=0} > 0$ are unstable. $q = 3$ sits at the edge of a broad resonance band

So the parametric resonance selects only a range of modes that get excited. In particular, taking the mode $\kappa = 0$, we can see from Fig. A.5 that $q = 3$ sits near a broad resonance band.

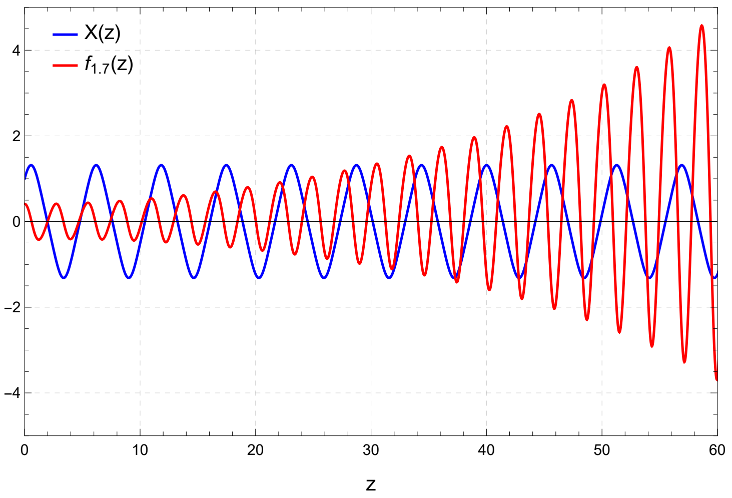

Figure A.6: Resonant amplification of a fluctuation mode for κ=1.7 and $q = 3$. The red curve shows the growing mode function $f_\kappa(z)$, while the blue curve is the background oscillation $X(z)$

The energy density in the physical fields, but in conformal rescale coordinate,

$$\rho(z, \vec{y}) = w_i^2 \left(\frac{\phi'^2}{2R^2} + \frac{(\vec{\nabla}\phi)^2}{2R^2} + \frac{V(\phi)}{w_i^2} \right), \quad ' \equiv \frac{d}{dz}, \tag{A.54}$$

where the three components are, respectively, the kinetic, gradient, and potential energy contributions. In the linear regime, the energy density of the scalar perfect fluid is dominated by the homogeneous mode, so we can approximate,

$$\rho(z, \vec{y}) \simeq \rho_0(z) = w_i^2 \left(\frac{\phi_0'^2}{2R^2} + \frac{V(\phi_0)}{w_i^2} \right) + \mathcal{O}(\delta\phi^2). \tag{A.55}$$

As discussed in Eq. (1.47), the virial theorem implies a partition of energy between kinetic and potential energies, on average,

$$\langle \text{Kin} \rangle = 2 \langle \text{Pot} \rangle, \tag{A.56}$$

and the homogeneous condensate behaves as radiation. Using the solution of the homogeneous mode in rescaled field coordinate, we can extrapolate the homogeneous kinetic and potential energy, recalling that $R(z) = \frac{H_i}{w_i}(1+z) = 1+z$,

$$R^4 \frac{\rho_{0,\text{kin}}}{w_i^2 \phi_i^2} = \frac{1}{2} \left(X' - \frac{XR'}{R} \right)^2, \quad R^4 \frac{\rho_{0,\text{pot}}}{w_i^2 \phi_i^2} = \frac{X^4}{4}, \tag{A.57}$$

and the analytical behaviour of the two components can be seen in Fig. A.7.

In this regime, the energy density of fluctuations is growing exponentially due to the parametric resonance. In the rescaled field variable f, X, the action is conformally flat, so we can define the occupation number for a specific mode κ as,

$$n_\kappa(z) = \frac{w_k}{2} \left(\frac{|f_\kappa(z)'|^2}{w_\kappa^2} + |f_\kappa|^2 \right) - \frac{1}{2} = \frac{w_k R^2}{2\phi_i^2} \left(\frac{|\delta\phi_\kappa' + \frac{R'}{R}\delta\phi_\kappa|^2}{w_\kappa^2} + |\delta\phi_\kappa|^2 \right) - \frac{1}{2}, \tag{A.58}$$

where we have subtracted the initial number density under the assumption of zero fluctuation at the initial time and express the occupation number as a function of the physical field. In

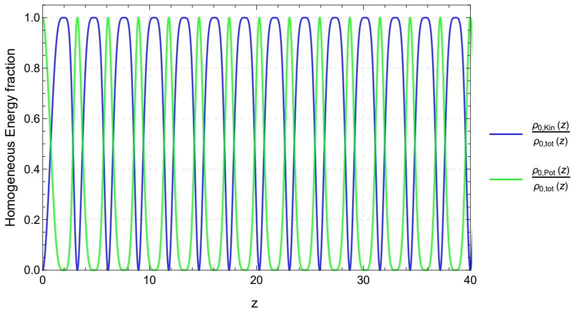

(a) Analytical energy fraction of the homogeneous field, in blue the fractional kinetic energy, while in green the fractional potential.

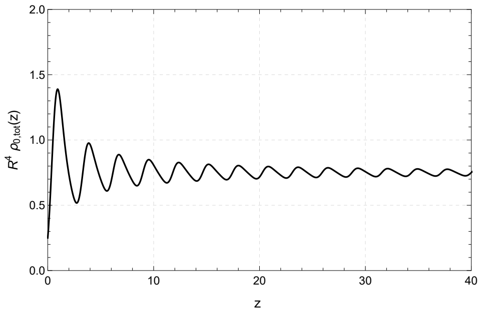

(b) Homogeneous energy density $\rho_{0,\mathrm{tot}} = \rho_{0,\mathrm{kin}} + \rho_{0,\mathrm{pot}}$ behaviour, a part some normalization. After the first transition, it reaches the oscillatory regime $w(z) \gg H(z)$, where fast oscillate around $3/4$, as expected from the initial condition $X(z_i) = X'(z_i) = 1$.

Figure A.7

particular, the effective frequency in the Hartree-Fock approximation, that capture the one-loop correction, is defined as

$$w_\kappa^2 = \kappa^2 + R^2 \left\langle \frac{d^2\tilde{V}}{d\phi^2} \right\rangle = \kappa^2 + 3 \left\langle \left(R\frac{\phi}{\phi_i} \right)^2 \right\rangle. \tag{A.59}$$

This approximation, and in particular the expression for the number spectra, is valid as long as

$$\frac{\langle\phi\rangle^2}{\langle\phi^2\rangle} \sim 1. \tag{A.60}$$

Imposing the usual Bunch-Davies initial condition,

$$f_\kappa(0) = \frac{1}{\sqrt{2w_\kappa(0)}}, \qquad f'_\kappa(z) = \frac{-iw_\kappa(0)}{\sqrt{2w_\kappa(0)}}, \tag{A.61}$$

we can extract the numerical solution of the number density from the equation of motion of the mode function in Eq. (A.48). In the Fig. A.8, we can see that only the mode in the unstable band grows exponentially. In the linear regime, we expect the dominant contribution to come from the mode in the narrow unstable band, for $1.62 \lesssim \kappa \lesssim 1.73$, so that the energy density of the fluctuation can be approximated,

$$R^4 \frac{\langle\delta\rho\rangle}{w_i^2\phi_i^2} \simeq \frac{\Delta\hat{\kappa}\cdot\hat{\kappa}^2}{\pi^2} w_{\hat{\kappa}}(z) n_{\hat{\kappa}}(z), \tag{A.62}$$

where $\Delta\hat{\kappa}$ is the approximate width of the narrow band.

Once the energy density of the fluctuations becomes comparable to the energy density of the homogeneous mode, the linear regime breaks down. We refer to this time as z_{br}, because it indicates the time when the energy of the homogeneous mode starts to be effectively transferred into fluctuation. We can estimate the end of this first phase using

$$\frac{\langle\delta\rho\rangle}{\rho_0}(z_{\mathrm{br}}) \sim 1 \Longrightarrow z_{\mathrm{br}} \sim \mathcal{O}(10^2), \tag{A.63}$$

where we used $n_{\hat{\kappa}} \sim e^{\mu_{\hat{\kappa}} z}$, $\rho_0 \sim \frac{3}{4}$, $\hat{\kappa} = 1.69$, $\Delta\hat{\kappa} \sim 0.03$ and $\mu_{\hat{\kappa}} \sim 0.036$.

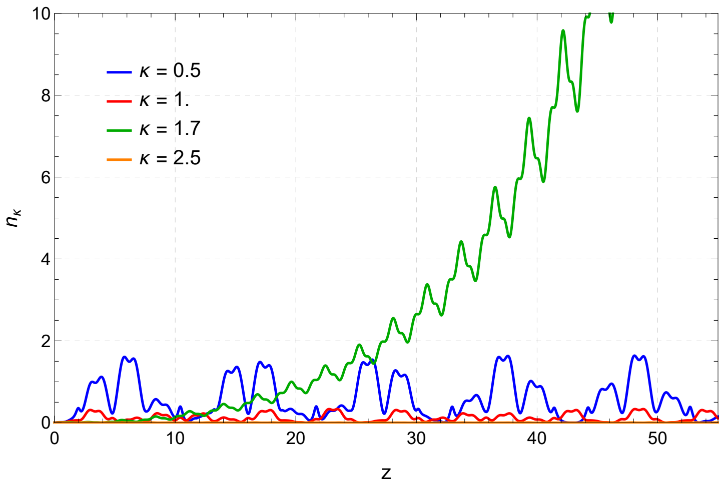

Figure A.8: Occupation number for different mode κ at linear order. Only the mode in the unstable band of the Lamè equation has an occupation number that grows exponentially.

Note that we are making an approximation. We are assuming a large occupation number, so that the particles behave classically. This is a good approximation for parametric resonance, since this regime is reached soon after the starting point of the dynamics. A more detailed discussion on the number density of quantum particles in a curved background can be found in [81, 82].

Efficient scattering and backreaction

The results of the previous section rely on the assumption of the linear regime, so that each mode κ evolves independently from the others and, in particular, the homogeneous dynamics is unperturbed in first approximation. As seen in the above section, the modes within the instability band grow exponentially, and soon after the onset of oscillations, the linear regime is no longer a valid approximation, necessitating the inclusion of new effects. In particular, as we will prove with lattice simulations, two important effects will enter in the physics,

- **Back-Reaction**: the creation of particles leads to a decrease in the amplitude of oscillations of the rescaled conformal field $X(z)$, which otherwise would remain constant. But this will change the effective mass of the fluctuation. This is efficient when the energy density of the fluctuation is of the same order of the energy of the condensate.

- **Efficient scattering**: efficient scattering between the homogeneous mode and the created particles excites new modes and modifies the instability band of the Lamè equation.

Initially, we expect the excitation of additional momentum modes, and the dynamics are governed by the Lamé equation in Eq. (A.48), with different resonance parameters. As the system evolves, the periodic background source becomes inefficient, leading to the termination of parametric resonance. This non-linear evolution cannot be captured analytically, and we therefore resort to lattice simulations to follow the full dynamics.

This qualitative picture is discussed in detail in Refs. [83, 84]. The aim of the present chapter is not to provide a complete analytical description of the non-linear dynamics, but rather to benchmark the linear Lamé analysis against the full lattice evolution, and to extract from the simulation output the key physical quantities that characterise the parametric resonance: the onset of backreaction, the efficiency of energy transfer from the condensate to the fluctuations, and the final state of the field after the resonance is terminated.

A.2.2 Lattice analysis

A.2.2.1 Introduction to CosmoLattice

To study the non-linear regime of the dynamics described above, we employ CosmoLattice [85], a modern C++ package for lattice simulations of interacting scalar (and gauge) field theories in an expanding universe. CosmoLattice operates in the classical-statistical approximation, which is justified whenever the occupation numbers of the relevant modes are large, $n_\kappa \gg 1$, so that the field quantum nature can be neglected. When such circumstances are met, classical field theory can be used to solve complex field dynamics, including cases where non-linear interactions characterise the field evolution and non-perturbative particle production effects are present.

Lattice discretisation. In 3-dimensions, the spatial volume is a cubic lattice of length L, with N^3 points. This set of points is collectively referred to as the lattice. After fixing L and N, the smallest possible distance between two sites, the so-called *lattice spacing*, is given by

$$\delta x \equiv \frac{L}{N}. \tag{A.64}$$

A continuum function f($\vec{x}$) with periodic boundary conditions implies that any momenta must be discretised. The infrared cut-off $k_{\rm IR}$ and the maximum (UV) comoving momentum accessible on the lattice are

$$k_{\rm IR} = \frac{2\pi}{L}\,, \quad k_{\rm max} = \sqrt{3}\,\frac{\pi}{\delta\tilde{x}} = \frac{\sqrt{3}}{2}\,N\,k_{\rm IR}\,. \tag{A.65}$$

fixing $N, k_{\rm IR}$ automatically determines L. The discrete Fourier transform (DFT) is then defined by

$$f(\vec{n}) \equiv \frac{1}{N^3}\sum_{\tilde{n}} e^{-i\frac{2\pi}{N}\tilde{\vec{n}}\vec{n}} f(\tilde{\vec{n}}), \tag{A.66}$$

with $\vec{n}$ indicates a point in the box, $\tilde{\vec{n}}$ indicates a point in the reciprocal lattice.

Program variables. Simulations are carried out not in the original physical field and space-time variables, but in a set of dimensionless *program variables* $\{\tilde{\phi},\, z,\, \tilde{x}^i\}$, defined by [85]

$$\tilde{\phi} \;\equiv\; \frac{\phi}{f_*}\,, \quad dz \;\equiv\; R^{-\alpha}\,\omega_*\,dt\,, \quad dy^i \;\equiv\; \omega_*\,dx^i\,, \tag{A.67}$$

where f_* and ω_* are constants that carry the dimensions of energy, and α is a constant that controls the time coordinate the simulation uses (e.g., $\alpha = 0$ corresponds to cosmic time, $\alpha = 1$ to rescale conformal time). The programme momenta are then expressed as

$$\kappa \equiv \frac{k}{w_*}, \tag{A.68}$$

so that the notation is the same as in the analytical discussion. In cosmolattice, any field theory is implemented by means of the *program potential*, which is a dimensionless quantity defined in terms of the programme variables as follows,

$$\tilde{V}(\tilde{\phi}) \equiv \frac{1}{f_*^2 w_*^2} V(f_*\phi). \tag{A.69}$$

Define also the dimensionless *program energy/ pressure densities*,

$$\tilde{\rho} \equiv \tilde{K} + \tilde{G} + \tilde{V}, \quad \tilde{p} \equiv \tilde{K} - \frac{1}{3}\tilde{G} - \tilde{V}. \tag{A.70}$$

In a model with N_s scalar fields the expression of $\tilde{K} \equiv \sum_n \tilde{K}^{(n)}$, $\tilde{G} \equiv \sum_n \tilde{G}^{(n)}$, with

$$\tilde{K}^{(n)} = \frac{1}{2R^{2\alpha}}(\tilde{\phi}'_n)^2, \quad \tilde{G}^{(n)} = \frac{1}{2R^{2\alpha}}\sum_i (\tilde{\nabla}_i \tilde{\phi}'_n)^2. \tag{A.71}$$

Initialization of fluctuations. In addition to the initial homogeneous modes, we need to initialise the set of fluctuations for each simulated scalar field. Cosmolattice mimics the initial quantum vacuum fluctuations, imposing the following sum of left- and right-moving waves to the field amplitude at each lattice point in momentum space,

$$\delta\tilde{\phi}(\tilde{\mathbf{n}}) = \frac{1}{\sqrt{2}}\left(|\delta\tilde{\phi}_1(\tilde{\mathbf{n}})|\, e^{i\theta_1(\tilde{\mathbf{n}})} + |\delta\tilde{\phi}_2(\tilde{\mathbf{n}})|\, e^{i\theta_2(\tilde{\mathbf{n}})}\right), \tag{60}$$

$$\delta\tilde{\phi}'(\tilde{\mathbf{n}}) = -\frac{1}{a^{1-\alpha}}\left[\frac{i\tilde{\omega}_k}{\sqrt{2}}\left(|\delta\tilde{\phi}_1(\tilde{\mathbf{n}})|\, e^{i\theta_1(\tilde{\mathbf{n}})} - |\delta\tilde{\phi}_2(\tilde{\mathbf{n}})|\, e^{i\theta_2(\tilde{\mathbf{n}})}\right)\right] - \tilde{\mathcal{H}}\,\delta\tilde{\phi}(\tilde{\mathbf{n}}), \tag{61}$$

where

$$\tilde{\omega}_k \equiv \sqrt{\kappa^2(\tilde{\mathbf{n}}) + R^2\tilde{m}_\phi^2}, \quad \tilde{\mathcal{H}} \equiv R^\alpha \frac{H}{\omega_*}. \tag{A.72}$$

In these expressions, $\theta_1(\tilde{\mathbf{n}})$ and $\theta_2(\tilde{\mathbf{n}})$ are two independent random phases (at each Fourier site) drawn from a uniform distribution in the range $[0, 2\pi)$, and $|\delta\tilde{\phi}_1(\tilde{\mathbf{n}})|$ and $|\delta\tilde{\phi}_2(\tilde{\mathbf{n}})|$ are random amplitudes (also assigned independently at each Fourier site) drawn from a Rayleigh distribution with expected squared amplitude

$$\left\langle |\delta\tilde{\phi}(\tilde{\mathbf{n}})|^2 \right\rangle \equiv \left(\frac{\omega_*}{f_*}\right)^2 \left(\frac{N}{\delta\tilde{x}}\right)^3 \frac{1}{2R^2\sqrt{\kappa^2(\tilde{\mathbf{n}}) + R^2\tilde{m}_\phi^2}}, \quad \tilde{m}_\phi^2 \equiv \left.\frac{\partial^2\tilde{V}}{\partial\tilde{\phi}^2}\right|_{\tilde{\phi}=\bar{\phi}_*}. \tag{62}$$

Drawing both phases and modulus amplitudes in this way is mathematically equivalent to drawing $\delta\tilde{\phi}(\tilde{\mathbf{n}})$ and $\delta\tilde{\phi}'(\tilde{\mathbf{n}})$ as Gaussian random fields.

Evolution and output CosmoLattice evolves the discrete field equations using symplectic (velocity-Verlet) integrators. The background metric can either be fixed to a power-law scale factor dictated by an external fluid (fixed background) or evolved self-consistently via the Friedmann equations. At each output time, the code provides a volume-averaged quantity, defined as

$$\langle A(\vec{n})\rangle_V \equiv \frac{1}{N^3}\sum_{\vec{n}} A(\vec{n}). \tag{A.73}$$

A.2.2.2 Lattice run for $\lambda\phi^4$

We simulate a single real scalar field ϕ with a pure quartic potential,

$$V(\phi) = \frac{\lambda}{4}\phi^4, \tag{A.74}$$

in a fixed background dominated by radiation, so that the scale factor evolves as $R(t) \propto t^{1/2}$, or equivalently $R(z) \propto (1+z)$ in the rescaled conformal time. This corresponds to the equation-of-state parameter $\omega_{\rm EoS} = 1/3$.
The choice of the mass scale is naturally given by,

$$f_* = \phi_i, \quad w_* \equiv \sqrt{\lambda}\phi_i, \tag{A.75}$$

with ϕ_i the initial amplitude. We choose as input the following initial condition,

$$\phi(t_i, \vec{x}) = \phi_i, \quad \dot{\phi}(t_i, \vec{x}) = 0. \tag{A.76}$$

where t_i is at the onset of oscillation, defined by $H(t_i) = \omega_i$. With this choice, the initial program-variable amplitude is $\tilde{\phi}(0) = 1$, and the program potential is simply

$$\tilde{V}(\tilde{\phi}) = \frac{1}{f_*^2 \omega_*^2} V(f_* \tilde{\phi}) = \frac{1}{4} \tilde{\phi}^4 . \tag{A.77}$$

The equation of motion in the programme variables reads

$$\tilde{\phi}'' - R^{-2} \nabla_y^2 \tilde{\phi} + 2 \frac{R'}{R} \tilde{\phi}' = -R^2 \tilde{\phi}^3, \quad ' \equiv \frac{d}{dz}. \tag{A.78}$$

Since Cosmolattice works from the equation of motion, the evolution depends only implicitly on λ. Note that this is precisely the programme-variable form of the equation analysed analytically throughout the parametric resonance discussion, in Eq. (A.29)

Simulation parameters. In the following section, we will present the results of a representative simulation, comparing them with the analytical estimation. The following parameters are selected.

Parameter	Symbol	Value
Lattice points per dimension	N	128
Infrared momentum cut-off	$\kappa_{\rm IR}$	0.1
Time step	δz	5×10^{-2}
UV momentum cut-off	$\kappa_{\rm cutoff}$	> 1.7
Final time	$z_{\rm max}$	$\mathcal{O}(10^3)$
Equation of state (fixed bg.)	$\omega_{\rm EoS}$	$1/3$
Coupling constant	λ	10^{-3}
Initial field amplitude	ϕ_i	such that $H_i = \omega_i$

The infrared cut-off $\kappa_{\rm IR} = 0.1$ sets the physical box size. The choice $N = 128$ gives a maximum accessible momentum $\kappa_{\rm max} = (\sqrt{3}/2) \times 128 \times 0.2 \approx 22.2$, well above the narrow instability band $1.6 \lesssim \kappa \lesssim 1.75$ identified in the Lamé analysis in Fig. A.2. The UV cut-off on the initial fluctuation spectrum ensures that only physically motivated modes are seeded at $z_0 = 0$, suppressing lattice artefacts at large momenta.

Outputs. For each run, CosmoLattice produces the following quantities that we will use in the analysis that follows.

- At each time step δz, we get in output,

$$\langle \tilde{\phi} \rangle, \ \langle \tilde{\phi^2} \rangle, \ \langle \tilde{\phi'} \rangle, \langle \tilde{\phi'^2} \rangle, \ \mathrm{rms}(\tilde{\phi}), \ \mathrm{rms}(\tilde{\phi}'). \tag{A.79}$$

- At each time step, the volume-averaged energy density components, defined from Eq. (A.71) and from the potential,

$$\langle \tilde{K} \rangle = \frac{1}{2R^2}\langle \tilde{\phi}'^2 \rangle, \quad \langle \tilde{G}^{(n)} \rangle = \frac{1}{2R^2}\sum_i \langle (\tilde{\nabla}_i \tilde{\phi}'_n)^2 \rangle, \quad \langle \tilde{V} \rangle = \frac{1}{4}\langle \tilde{\phi}^4 \rangle, \quad \langle \tilde{\rho} \rangle, \tag{A.80}$$

  where $\langle \tilde{\rho} \rangle$ is the total (programme) energy density.

- Scale factors and derivatives at each time step $R,\ R',\ R'/R$. In this case the background is fix, so it will be just to check that the lattice geometry is correct.

- The lattice occupation number per mode, $\langle n_\kappa \rangle$ for bin Δn_{bin}, is defined

$$n_\kappa(z) = \mathcal{C}(N, L)\frac{w_k}{2}\left(\frac{\langle |(R\tilde{\phi}_\kappa)'|^2 \rangle}{w_\kappa^2} + \langle |(R\tilde{\phi}_\kappa)|^2 \rangle \right) \tag{A.81}$$

  where $\mathcal{C}$ is a constant function of lattice parameter and the mode frequency $w_\kappa^2(z) = \kappa^2 + R^2 \langle \frac{d^2V}{d\phi^2} \rangle$. This formula is independent of N, L once the average is expanded; more details are given in Ref. [85]

A.2.2.3 Lattice results

From the output file, we can see that there are three different time regimes,

- $0 < z \lesssim z_{\text{br}}$: This is the time interval in which the linear regime is a good approximation, and we can compare it with the analytical results.

- $z_{\text{br}} < z < z_{\text{eq}}$: the parametric resonance of the narrow resonance band effectively reacts back on the homogeneous mode, leading to a significant decrease in amplitude. The instability band of the Lamè equation is significantly restructured.

- $z > z_{\text{eq}}$: Parametric resonance is no more efficient.

Lattice output: scale factor

As discussed in the previous section, the input evolution for the geometry is a fixed radiation background. As expected, the output file of the scale factor and derivative is consistent during all dynamics; the lattice output matches the analytical expression in Eq. (A.37), with $z_i = 0$.

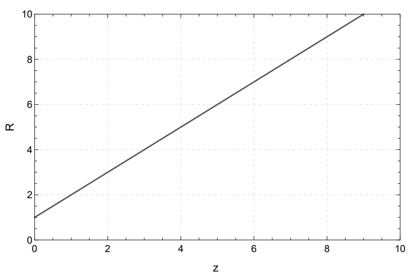

(a) Scale factor evolution from Lattice simulation

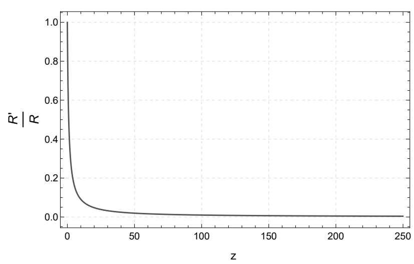

(b) Conformal Hubble rate from Lattice simulation

Lattice output: homogeneous field dynamics

The lattice evolves the rescaled physical field; the homogeneous mode is extracted as the volume average

$$\langle \tilde{\phi}(z, \vec{y}) \rangle = \frac{\langle \phi(z, \vec{y}) \rangle}{\phi_i} = \frac{X(z)}{R(z)}, \tag{A.82}$$

where in the last equation we have redefined the output as a function of $X(z)$, to match with the analytical estimation in Eq. (A.45). Fig. A.10 summarises the behaviour of the spatial average field across the three dynamical regimes.

- **Linear regime ($z < z_{\rm br}$).** During the early evolution, the homogeneous mode oscillates coherently, and the linear solution in Eq. (A.45) provides an accurate description of the lattice output, as shown in the left panel of Fig. A.10.
- **Effective non-linear regime, ($z_{\rm br} < z < z_{\rm eq}$).** The exponentially growing fluctuation modes carry enough energy to significantly alter the background, and the amplitude of the homogeneous mode begins to decrease, efficiently transferring energy from the condensate to the particle excitations.
- **Late-time regime ($z \gg z_{\rm eq}$).** Once the homogeneous condensate loses more than 50% of the initial energy, the parametric resonance is no longer efficient. The system does not return to linear dynamics: the homogeneous mode continues to lose energy, but at a slower rate compared to the resonance regime, due to scattering and particle production.

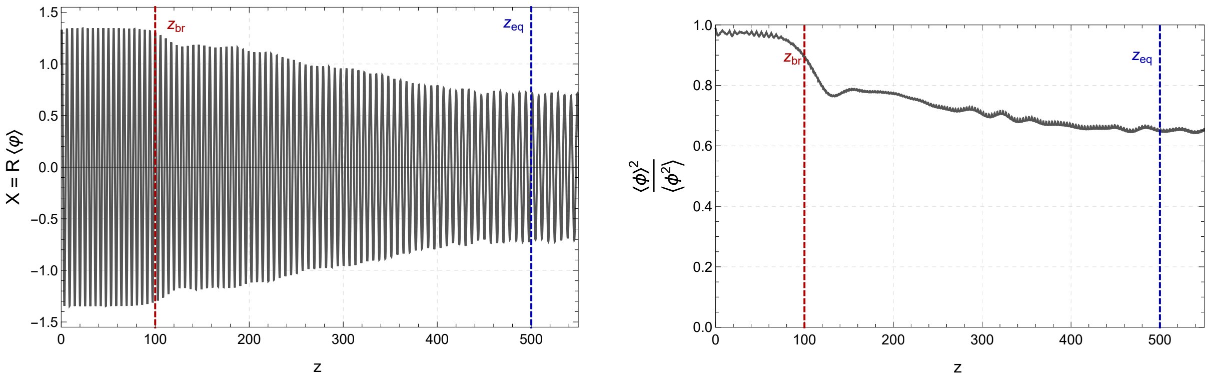

(a) Lattice dynamics of the rescaled homogeneous mode.

(b) Condensate-to-fluctuation ratio $\langle\phi\rangle^2/\langle\phi^2\rangle$; the red dashed line marks $z_{\rm br}$, while the blue $z_{\rm eq}$.

Figure A.10

In the right panel of Fig. A.10, the degree of coherence of the condensate, captured by the ratio

$$\frac{\langle\tilde{\phi}\rangle^2}{\langle\tilde{\phi}^2\rangle} = \frac{\langle\phi\rangle^2}{\langle\phi^2\rangle}. \tag{A.83}$$

Here $\langle\tilde{\phi}^2\rangle = \langle\tilde{\phi}\rangle^2 + \langle\tilde{\delta}\phi^2\rangle$ is the mean-square field on the lattice, where $\langle\tilde{\delta}\phi^2\rangle$ is the variance of the classical field fluctuations. In the first regime, it remains close to unity; the mean-square field is dominated by the coherent zero mode. Then the efficient non-linear regimes begin, and parametric resonance ends when

$$\frac{\langle\phi\rangle^2}{\langle\phi^2\rangle} \simeq 0.9, \tag{A.84}$$

very close to unity. This effect is described in Ref. [83], even a very small amount of fluctuation may shift the resonance band away from its original position, which may terminate the resonance for the leading modes.

Lattice output: energy analysis

The evolution of the average fractional energy components is shown in Fig. A.11, where the various contributions are defined in Eq. (A.80).

- **Linear regime** ($z < z_{\rm br}$). The energy budget is entirely dominated by the homogeneous condensate, in agreement with the analytical treatment. The virial theorem for a quartic potential fixes the time-averaged partition to

$$\frac{E_V}{E_{\rm tot}} \simeq 33.3\%, \quad \frac{E_G}{E_{\rm tot}} \lesssim 0.01\%, \quad \frac{E_K}{E_{\rm tot}} \simeq 66.6\%, \tag{A.85}$$

with the gradient energy remaining negligible but growing exponentially as the resonant modes are populated.

- **Non-linear regime** ($z_{\rm br} < z < z_{\rm eq}$). The energy stored in the homogeneous condensate is rapidly transferred to the fluctuations. The gradient energy rises sharply and overtakes the potential energy, reflecting the fact that the energy of the system is increasingly concentrated in the spatial inhomogeneities rather than in the interaction. The kinetic energy fraction remains comparatively large throughout this phase, indicating that a significant portion of it now resides in the fluctuations rather than in the homogeneous mode alone.

- **Late-time regime** ($z \gg z_{\rm eq}$). After the termination of parametric resonance, the energy fractions evolve much more slowly. The potential energy continues to decrease as the residual condensate gradually loses its remaining energy to fluctuations, but on a timescale far longer than that of the resonance phase.

The equation of state for the population of scalar fields is described in the left panel of Fig. A.12, and behaves like radiation for all the dynamics, as illustrated in the right panel of Fig. A.7. To quantify the depletion of the condensate, we define its fractional energy as

$$E_X = \frac{1}{2R^2}\langle\tilde{\phi}'\rangle^2 + \frac{1}{4}\langle\tilde{\phi}\rangle^4. \tag{A.86}$$

As shown in the right panel of Fig. A.12, by $z \gg z_{\rm eq}$ roughly 80% of the initial condensate energy has been transferred to fluctuations and to the interaction energy between the zero mode and the fluctuations, marking the near-complete dissolution of the coherent background at late time.

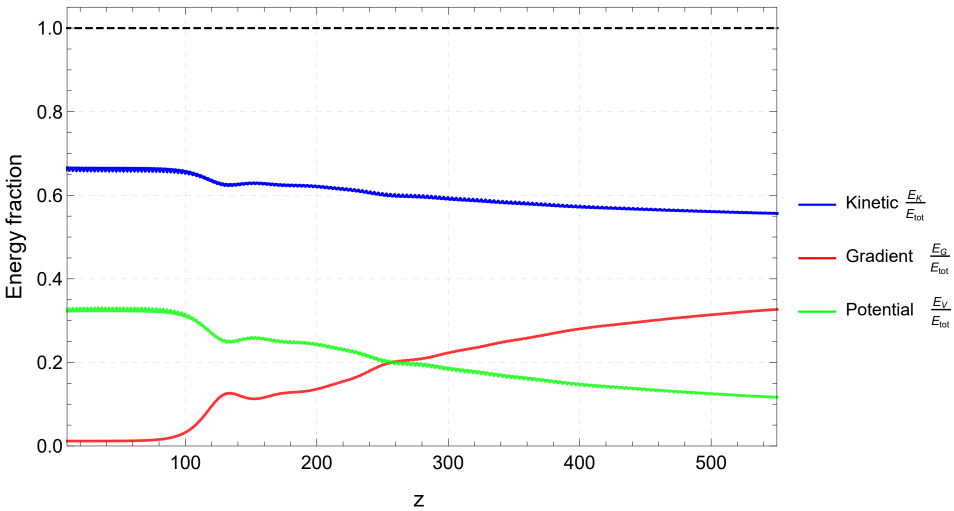

Figure A.11: Average energy fractions evolution, in blue the fractional kinetic energy, in red the gradient energy and in green the potential.

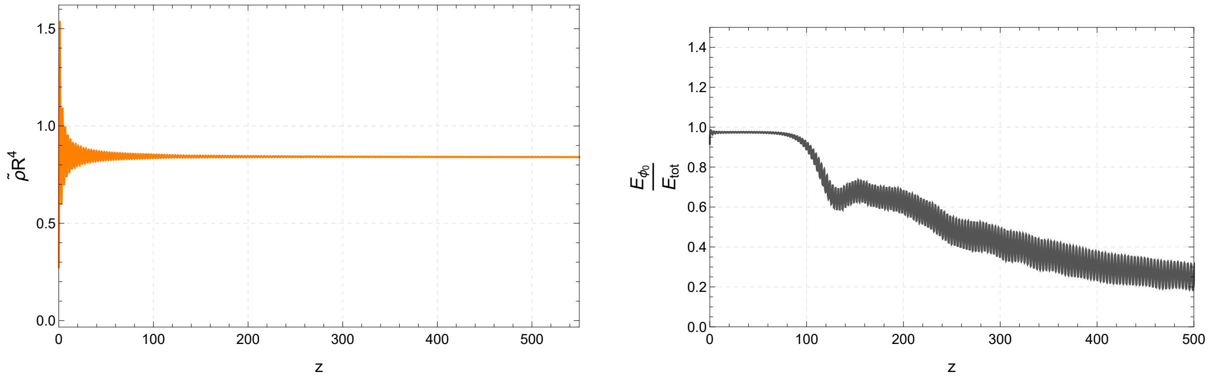

(a) Total energy density rescaled by R^4, confirming radiation-like scaling after the first few oscillations.

(b) Fractional energy of the homogeneous condensate $E_X/E_{\rm tot}$.

Figure A.12

Lattice output: occupation number analysis

The spectral analysis supports what we have discussed so far, as illustrated in Fig. A.13,

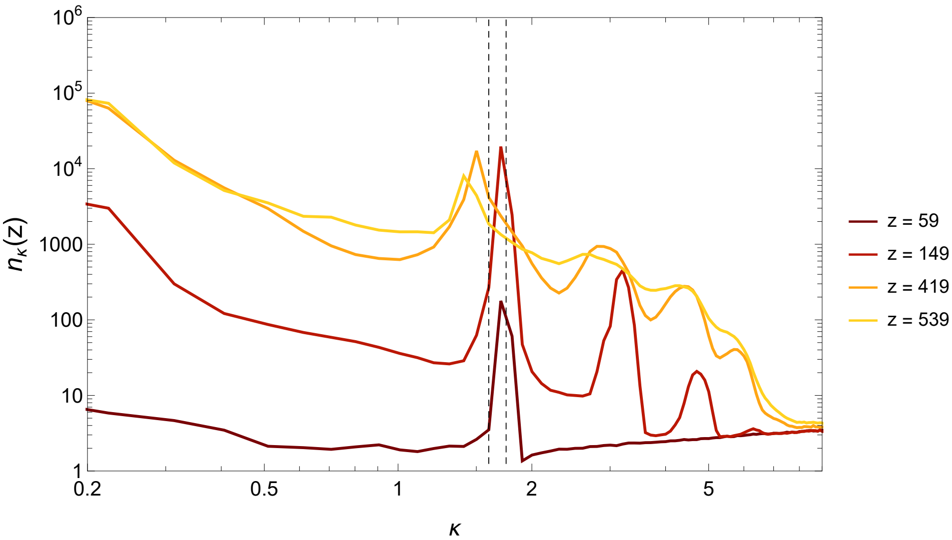

Figure A.13: Lattice occupation number as a function of κ at different snapshot time. The lighter the color, the later the time. The black dashed line is the expected mode that experiences parametric resonance in the linear regime, from Fig. A.2.

- **Linear regime** ($z < z_{\rm br}$). The linear regime estimates the narrow unstable resonance band at $\kappa \sim 1.7$, which is compatible with the lattice output. This is the only mode that starts to grow exponentially at the beginning of the simulation.
- **Non-linear regime** ($z_{\rm br} < z < z_{\rm eq}$): The instability chart of the Lamè equation is changed significantly due to efficient back-reaction. A set of narrow resonance bands starts to grow at higher momentum κ, the higher the mode, the later it starts to grow.For lower momenta, the spectrum appears to develop into a broad resonance band.
- **Late-time regime** ($z \gg z_{\rm eq}$): the occupation number remains approximately constant, and the mode with $\kappa < 8$ remains excited.

A.3 Parametric resonance in an axion model with quartic interactions

For the quartic axion case, there are two main differences. The first is that we have a complex field, so there are more interaction terms. The second is the presence of the radial mode with a constant mass, which significantly changes the dynamics.

A.3.1 Linear analysis

The potential is the one defined in Chapter 2,

$$V = \lambda_{PQ}\left(|\Phi|^2 - \frac{f_a^2}{2}\right)^2. \tag{A.87}$$

We will work in a different convention, easier to compare with the lattice simulation, defined as

$$\Phi = \frac{r}{\sqrt{2}}e^{i\theta}. \tag{A.88}$$

The radial and angular modes are related to the fields in Chapter 2 by

$$r = \chi + f_a, \quad \theta = \frac{a}{f_a}. \tag{A.89}$$

The equations of motion are

$$\delta S = 0 \implies \begin{cases} \nabla_\mu\left(r^2\nabla^\mu\theta\right) = 0, \\ \Box r - r\nabla_\mu\theta\nabla^\mu\theta - \lambda_{PQ}r\left(r^2 - f_a^2\right) = 0. \end{cases} \tag{A.90}$$

We assume, as initial conditions, purely homogeneous fields at t_i with a large displacement from the true vacuum,

$$r(t_i,\vec{x}) = r(t_i) \gg f_a, \quad \dot{r}(t_i,\vec{x}) = 0, \quad \theta(t_i,\vec{x}) = \theta(t_i), \quad \dot{\theta}(t_i,\vec{x}) = 0, \quad \dot{} \equiv \frac{d}{dt}. \tag{A.91}$$

In the linear regime, the homogeneous dynamics is not affected by fluctuations. Splitting as usual into homogeneous and spatial fluctuation the fields,

$$r(t,\vec{x}) = r_0(t) + \delta r(t,\vec{x}), \quad \theta(t,\vec{x}) = \theta_0(t) + \delta\theta(t,\vec{x}). \tag{A.92}$$

The homogeneous angular dynamics is solved in Eq. (2.25) and therefore $\theta_0(t) = \theta(t_i)$.
For the radial field and the axion fluctuation, it is convenient to introduce rescaled variables for both time and fields, analogously to the quartic case for the radial mode,

$$w_i \equiv \sqrt{2\lambda_{PQ}}|\Phi_i| = \sqrt{\lambda_{PQ}}r_i, \quad t \to z \equiv w_i\int\frac{dt}{R(t)}, \tag{A.93}$$

$$\delta\theta \to \delta f = R\frac{r}{r_i}\delta\theta, \quad r_0 + \delta r \to X_0 + \delta X \equiv R\frac{(r_0+\delta r)}{r_i}, \tag{A.94}$$

where we choose the initial time t_i such that $w_i = H_i$. The equations of motion at linear order for X_0, δX, and δf are

$$\begin{cases} X_0'' + X_0^3 - R^2X_0\frac{f_a^2}{r_i^2} = 0 + \mathcal{O}(\delta X X_0^2) \\ \delta X'' - \left(\frac{\nabla^2}{w_i^2} - 3X_0^2 + R^2\frac{f_a^2}{r_i^2}\right)\delta X = 0 + \mathcal{O}(\delta X^2 X_0) \\ \delta f'' - \left(\frac{\nabla^2}{w_i^2} + \frac{X_0''}{X_0}\right)\delta f = 0 + \mathcal{O}(\delta f\delta X) \end{cases}, \quad ' \equiv \frac{d}{dz}. \tag{A.95}$$

For the parametric resonance to be achieved, we need a large displacement of the field from the minimum $r_i \gg f_a$; otherwise, the effective frequency in the fluctuation equation is constant and no longer oscillates as required for the Lamé instability.

Initially, the radial dynamics is well described by a quartic potential. From Section A.2 and the appearance of the mass term, we can identify four reference times:

- z_i: the initial simulation time, defined by $H_i = w_i$.
- $z_{\rm br}$: when the linear regime no longer captures the main dynamics; the onset of effective decay of the homogeneous mode.
- $z_{\rm mass}$: due to the expansion of the universe, the quadratic term in the homogeneous equation begins to dominate, the field changes its dynamics and oscillates around the true vacuum. This can be identified roughly as the time when

$$X_0^2(z_{\rm mass}) \sim R^2(z_{\rm mass}) \left(\frac{f_a}{r_i}\right)^2. \tag{A.96}$$

- $z_{\rm eq}$: if the ratio $\frac{f_a}{r_i}$ is small enough, the parametric resonance ends before the field starts to oscillate around the true vacuum.

The ratio f_a/r_i therefore determines the duration of the parametric resonance. For the homogeneous mode, the differential equation can be analysed in two regimes. The first is analogous to the quartic case, whose solution is derived in Eq. (1.32), while the second involves oscillations around f_a in the WKB approximation, as discussed in Eq. (1.32),

$$\begin{cases} X_0(z) = 3^{\frac{1}{4}} \mathrm{cn}\left(3^{\frac{1}{4}}(z-z_i) - \mathrm{cn}^{-1}\left(3^{-\frac{1}{4}}, \frac{1}{\sqrt{2}}\right), \frac{1}{\sqrt{2}}\right), & z \ll z_{\rm mass}, \\ X_0(z) = (1+z)\left(\frac{f_a}{r_i} + \frac{A_*}{(1+z)^{\frac{3}{2}}}\cos\left(\frac{f_a}{r_i}\int_{z_*}^{z} R(z')dz' + C_*\right)\right), & z \gg z_{\rm mass}, \end{cases} \tag{A.97}$$

where A_* and C_* are integration constants. The numerical integration is shown in the upper-left panel of Fig. A.14, where both regimes are captured using the reference value

$$\frac{f_a}{r_i} \sim 10^{-2}. \tag{A.98}$$

From Eq. (A.96) we can estimate $z_{\rm mass} \sim 10^2$, as confirmed by the numerical integration. Going to Fourier space and quantising the field, the fluctuations in the linear regime obey a Lamé differential equation. Defining the rescaled comoving momenta

$$\kappa_r = \frac{k_{r,\rm com}}{w_i}, \quad \kappa_\theta = \frac{k_{\theta,\rm com}}{w_i}, \tag{A.99}$$

the equations of motion in the first regime $z \ll z_{\rm mass}$ are the followings

$$\begin{cases} \delta X''_{\kappa_r} + \left(\kappa_r^2 + 3X_0^2 + R^2\frac{f_a^2}{r_i^2}\right)\delta X_{\kappa_r} = 0 + \mathcal{O}(\delta X^2 X_0), \\ \delta f''_{\kappa_\theta} + \left(\kappa_\theta^2 + X_0^2 - R^2\frac{f_a^2}{r_i^2}\right)\delta f_{\kappa_\theta} = 0 + \mathcal{O}(\delta f \delta X), \end{cases} \quad z \ll z_{\rm mass}. \tag{A.100}$$

The fluctuations obey a Lamé equation in Eq. (A.48) with respective resonance parameters

$$\alpha_r = \frac{\kappa_r^2}{\sqrt{3}}, \quad q_r = 3, \quad \alpha_\theta = \frac{\kappa_\theta^2}{\sqrt{3}}, \quad q_\theta = 1. \tag{A.101}$$

Modes inside the unstable band experience exponential growth. From the Floquet exponent values, as can be seen in the upper-right panel of Fig. A.14, we expect a narrow resonance band for the radial fluctuation and a broad resonance band for the angular mode. For $z \gg z_{\rm mass}$, the equations of motion reduce to the standard case for massive and massless fields,

$$\begin{cases} \delta X''_{\kappa_r} + \left(\kappa_r^2 + 4R^2 \frac{f_a^2}{r_i^2}\right) \delta X_{\kappa_r} \simeq 0 \\ \delta f''_{\kappa_\theta} + \kappa_\theta^2 \, \delta f_{\kappa_\theta} \simeq 0 \end{cases} , \quad z \gg z_{\rm mass}. \tag{A.102}$$

The energy density of the system can be divided into radial and angular contributions,

$$\rho_{\rm tot} = \rho_r + \rho_\theta, \tag{A.103}$$

with

$$\rho_r = \frac{w_i^2 r'^2}{2R^2} + \frac{(\vec{\nabla} r)^2}{2R^2} + \frac{\lambda}{4}\left(r^2 - f_a^2\right)^2, \quad \rho_\theta = \frac{w_i^2 r^2 \theta'^2}{2R^2} + \frac{r^2 (\vec{\nabla}\theta)^2}{2R^2}. \tag{A.104}$$

In the linear regime the energy density is dominated by the homogeneous mode, whose analytical energy density is

$$\rho_{r,0}^{\rm tot} = \rho_{r,0}^{\rm kin} + \rho_{r,0}^{\rm pot} = \frac{w_i^2 r_i^2}{R^4}\left(\frac{R^2}{2}\left(\frac{X_0}{R}\right)'^{\,2} + \frac{1}{4}\left(X_0^2 - \left(\frac{f_a}{r_i}\right)^2\right)^2\right). \tag{A.105}$$

As discussed in Eq. (1.47), we expect on average that the homogeneous mode behaves like radiation at early times $z \ll z_{\rm mass}$ and like matter at late times $z \gg z_{\rm mass}$,

$$\begin{aligned} R^4 \rho_{0,r} &\simeq \text{const}, \quad z \ll z_{\rm mass}, \\ R^3 \rho_{0,r} &\simeq \text{const}, \quad z \gg z_{\rm mass}. \end{aligned} \tag{A.106}$$

A.3.2 Lattice analysis

We have discussed the relevant quantities in Section A.2.2.1. The structure will be the same as the quartic case. The simulation does not need further manipulation, because Cosmolattice is able to simulate complex field.

Lattice run for $\frac{\lambda_{PQ}}{4}\left(r^2 - f_a^2\right)^2$

The choice of the mass scale is naturally given by,

$$f_* = r_i, \quad w_* \equiv \sqrt{\lambda} r_i, \tag{A.107}$$

with r_i the initial amplitude. We choose as input the same initial condition in Eq. (A.92). With this choice, the initial program-variable radial amplitude is $\tilde{r}(0) = 1$, and the program potential is simply

$$\tilde{V}(\tilde{\phi}) = \frac{1}{f_*^2 \omega_*^2} V(f_* \tilde{\phi}) = \frac{1}{4}\left(\tilde{r}^2 - \frac{f_a^2}{r_i^2}\right)^2. \tag{A.108}$$

Since Cosmolattice works from the equation of motion, the evolution depends only implicitly on λ_{PQ}.

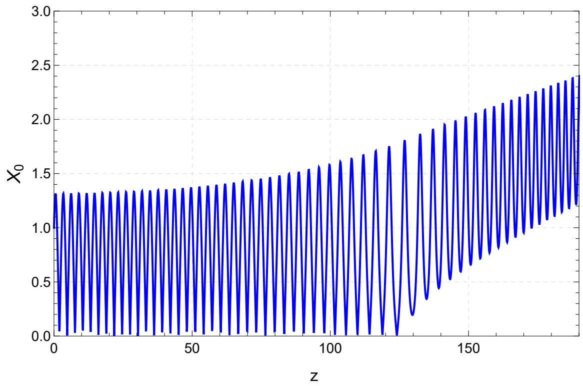

(a) Rescaled homogeneous radial mode $X_0 = R\,r/r_i$ in the linear regime, obtained by numerically integrating Eq. (A.95) with $f_a/r_i = 10^{-2}$. The two dynamical regimes are clearly visible.

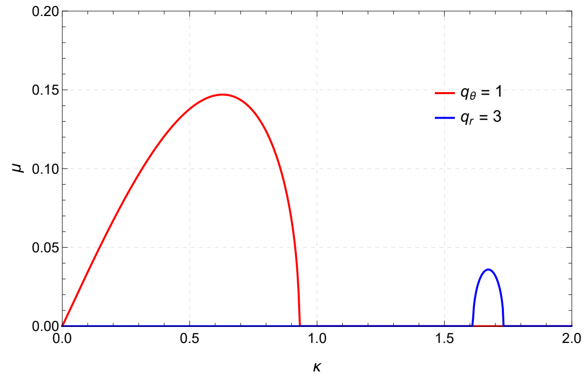

(b) Floquet exponent for solutions of the Lamé equation with resonance parameters $q_\theta = 1$ (angular mode) and $q_r = 3$ (radial mode).

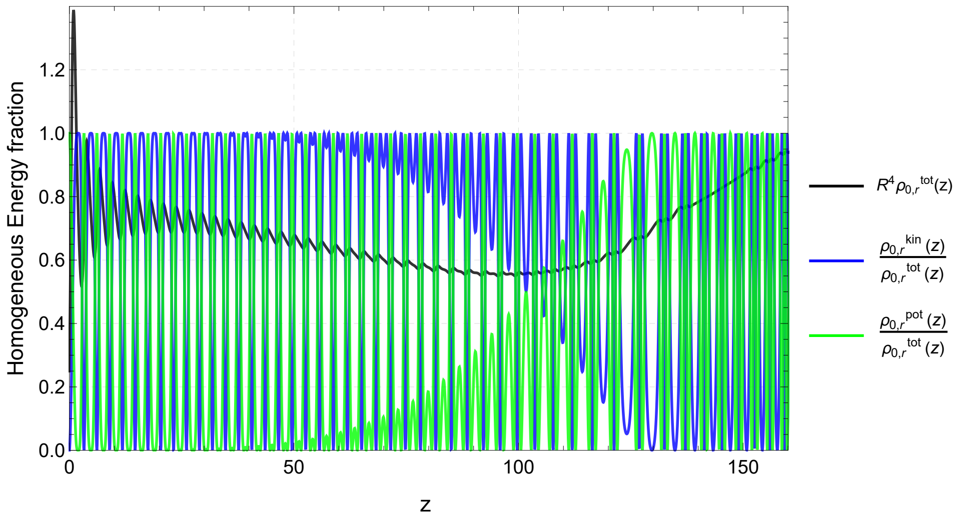

(c) Homogeneous energy behaviour in the two dynamical regimes. In black, the total energy $R^4\rho_{0,\text{tot}}$, which is approximately constant at early times and scales like matter at late times. In blue and green, the kinetic and potential fractional energies, respectively.

Figure A.14

Simulation parameters. In the following section, we will present the results of a representative simulation, comparing them with the analytical estimation. The following parameters are selected.

Parameter	Symbol	Value
Lattice points per dimension	N	128
Infrared momentum cut-off	$\kappa_{\rm IR}$	0.08
Time step	δz	5×10^{-2}
UV momentum cut-off	$\kappa_{\rm cutoff}$	> 1.7
Final time	$z_{\rm max}$	$\mathcal{O}(10^3)$
Equation of state (fixed bg.)	$\omega_{\rm EoS}$	1/3
Coupling constant	λ_{PQ}	10^{-3}
Ratio initial displacement	$\frac{f_a}{r_i}$	$\mathcal{O}(10^{-2})$
Initial angular value	θ_i	$\frac{\pi}{4}$

Outputs. For each run, CosmoLattice produces the following quantities that we will use in the analysis that follows.

- At each time step δz, we get in output,

$$\langle\tilde{\phi}_i\rangle,\ \langle\tilde{\phi}_i^2\rangle,\ \langle\tilde{\phi}_i'\rangle, \langle\tilde{\phi}_i'^2\rangle,\ \mathrm{rms}(\tilde{\phi}_i),\ \mathrm{rms}(\tilde{\phi}_i'),\quad \tilde{\phi}_i = \tilde{r}, \theta, \tag{A.109}$$

  where the angle is not rescaled.

- The volume-averaged energy densities in output at each time step of the radial mode, are

$$\tilde{E}_V = \frac{1}{4}\left\langle\left(\tilde{r}^2 - \left(\frac{f_a}{r_i}\right)^2\right)^2\right\rangle,\ \tilde{E}_{r,K} = \frac{1}{2R^2}\left\langle\tilde{r}'^2\right\rangle,\ \tilde{E}_{r,G} = \frac{1}{2R^2}\left\langle\sum_i \nabla_i\tilde{r}^2\right\rangle, \tag{A.110}$$

  while for the angular energy,

$$\tilde{E}_{\theta,K} = \frac{1}{2R^2}\left\langle\left(\tilde{r}\theta'\right)^2\right\rangle, \quad \tilde{E}_{\theta,G} = \frac{1}{2R^2}\left\langle\sum_i\left(\tilde{r}\nabla_i\theta\right)^2\right\rangle. \tag{A.111}$$

  The total rescaled energy density is their sum,

$$\langle\tilde{\rho}\rangle \equiv \tilde{E}_{\rm tot} = \tilde{E}_{r,\rm tot} + \tilde{E}_{\theta,\rm tot} = \tilde{E}_V + \tilde{E}_{r,G} + \tilde{E}_{r,K} + \tilde{E}_{\theta,G} + \tilde{E}_{\theta,K}. \tag{A.112}$$

- Scale factors and derivatives at each time step $R,\ R',\ R'/R$, the same as the quartic simulation.

- The total occupation number density spectrum is defined as

$$n_\kappa(z) = \mathcal{C}(N,L)\frac{w_k R^2}{2}\left(\frac{\langle|\frac{R'}{R}\tilde{r}_\kappa + \tilde{r}_\kappa' + i\tilde{r}_\kappa\theta_\kappa'|^2\rangle}{w_\kappa^2} + \langle|\tilde{r}_\kappa|^2\rangle\right), \tag{A.113}$$

  where $\mathcal{C}$ is a constant function of lattice parameter and the mode frequency $w_\kappa^2(z) = \kappa^2 + R^2\langle\frac{d^2V}{d\phi^2}\rangle$. This formula is independent of N, L once the average is expanded; more details are given in Ref. [85].

Lattice output: homogeneous condensate

The scale factor evolution is analogous to the quartic case. As illustrated in Fig. A.15, we can identify the two characteristic times,

$$z_{\rm br} \simeq 20, \quad z_{\rm mass} \simeq 80. \tag{A.114}$$

After the mass term becomes dominant, the linear regime can be trusted again. As discussed for the quartic case, the analytical regime does not capture the backreaction of the unstable modes on the homogeneous mode, which rapidly transfers half of the energy to the fluctuations. The rescaled field evolution is shown in the upper-left panel of Fig. A.15. The homogeneous angular component, as expected, remains in the vacuum state throughout the run. Neglecting the axion mass term fixes the validity of the simulation to $z \ll z_{\rm QCD}$, where, using $RT \sim$ const to first approximation,

$$z_{\rm QCD} \sim \frac{\sqrt{M_{\rm pl} w_i}}{T_{\rm QCD}}. \tag{A.115}$$

For our lattice simulation parameters, we obtain $z_{\rm QCD} \sim 10^{15}$.

Lattice output: radial and angular energy

The various contributions of the energy component are shown in Fig. A.16. The results can be divided into three intervals.

- $0 < z \ll z_{\rm br}$: the energy density is dominated by the radial homogeneous mode, as the analytical solution shown in Fig. A.14 describes well both the kinetic and potential fractional behaviour and the total energy density. On average,

$$\begin{aligned} &\frac{E_{r,K}}{E_{\rm tot}} \sim \frac{E_{r_0,K}}{E_{\rm tot}} = 62\%, \quad \frac{E_{r,V}}{E_{\rm tot}} \sim \frac{E_{r_0,V}}{E_{\rm tot}} = 0.32\%, \\ &\frac{E_{r,G}}{E_{\rm tot}} \simeq 0.4\%, \quad \frac{E_{\theta,\rm tot}}{E_{\rm tot}} \simeq 0.5\%, \quad 0 < z \ll z_{\rm br}. \end{aligned} \tag{A.116}$$

  The exponential growth of the unstable modes drives an exponential increase in the angular fluctuation energy density via parametric resonance, so that at $z_{\rm br}$ equipartition is reached:

$$\frac{E_{\theta,\rm tot}}{E_{\rm tot}}(z_{\rm br}) \sim \frac{E_{r,\rm tot}}{E_{\rm tot}}(z_{\rm br}). \tag{A.117}$$

  From this point on, backreaction on the homogeneous condensate is non-negligible.

- $z_{\rm br} < z < z_{\rm mass}$: the potential energy, mostly dominated by the homogeneous mode, is effectively transferred to the fluctuations of the angular and radial modes, as illustrated in Fig. A.16. In particular,

$$\begin{aligned} &\frac{E_{r,K}}{E_{\rm tot}} = 16\%, \quad \frac{E_{r,V}}{E_{\rm tot}} = 12\%, \quad \frac{E_{r,G}}{E_{\rm tot}} = 5\%, \\ &\frac{E_{\theta,K}}{E_{\rm tot}} = 42\%, \quad \frac{E_{\theta,G}}{E_{\rm tot}} = 24\%, \quad \frac{E_{r,\rm tot}}{E_{\theta,\rm tot}} \simeq \frac{1}{2}, \quad z \sim z_{\rm mass}. \end{aligned} \tag{A.118}$$

- $z \gg z_{\rm mass}$: the dynamics of the angular and radial modes can be safely treated perturbatively. From this point on, the energy density of the homogeneous mode scales like matter, while the angular energy scales like radiation. As shown in the upper-left panel of Fig. A.16, the residual homogeneous radial energy is very small.

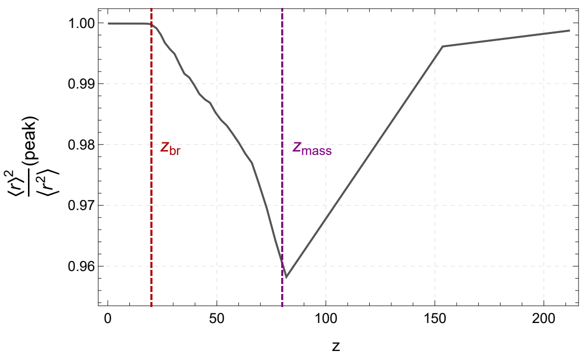

(a) Ratio between $\langle r^2 \rangle$ and the radial condensate r_0^2. As in the quartic case, backreaction is efficient when the fluctuation contribution is subdominant. After z_{mass}, the system slowly re-enters the linear regime, though fluctuations no longer dominate the energy density.

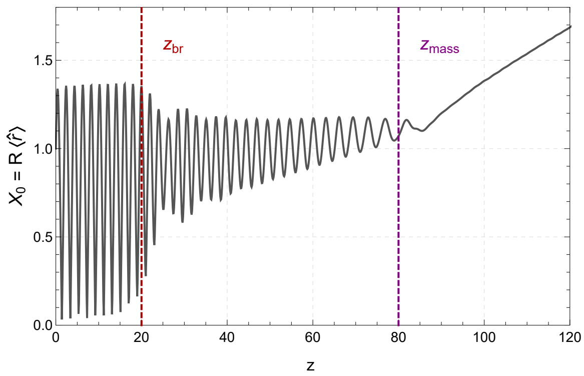

(b) Rescaled conformal radial homogeneous mode $X_0 = R\langle \hat{r} \rangle$. The red dashed line marks the onset of backreaction z_{br}, where the linear regime breaks down; the purple dashed line marks z_{mass}, when the field begins to oscillate around the true vacuum and parametric resonance ceases.

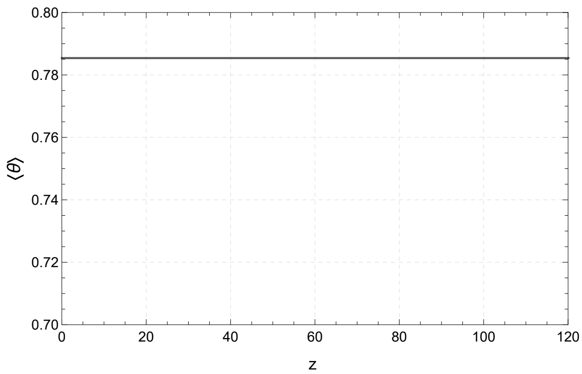

(c) Homogeneous angular mode with initial condition $\langle \theta \rangle(z_i) = \frac{\pi}{4}$, remaining frozen at the initial value throughout the run.

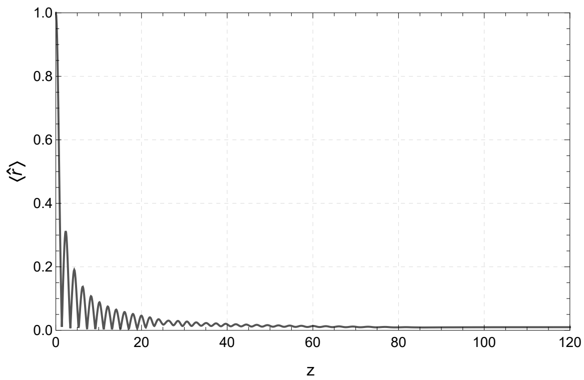

(d) Full time history of the rescaled homogeneous radial field $\langle \hat{r} \rangle = \langle r/r_i \rangle$, showing the transition from oscillation to the approach to the true vacuum.

Figure A.15: Radial homogeneous mode dynamics across the three regimes: linear ($z < z_{\mathrm{br}}$), parametric resonance ($z_{\mathrm{br}} < z < z_{\mathrm{mass}}$), and oscillation around the true vacuum ($z > z_{\mathrm{mass}}$).

Lattice output: occupation number spectra

The output of the occupation number spectra is shown in Fig. A.17 and can again be split into three regimes:

- $0 < z < z_{\mathrm{br}}$: this is analogous to the quartic case. The narrow and broad resonance bands appear at the values of κ expected from the linear regime. However, scattering is already efficient, so other modes are also excited. The radial narrow band at $q = 3$ can be distinguished only at early times, since its Floquet exponent is very small compared to the axion instability.

- $z_{\mathrm{br}} < z < z_{\mathrm{mass}}$: the instability chart of the Lamé equation is significantly modified, and modes with $\kappa < 5$ become excited, while the modes excited in the linear regime remain fixed.

- $z > z_{\mathrm{mass}}$: the fluctuations no longer experience a strong oscillatory background, and parametric resonance ceases to be efficient. The lattice occupation number remains approximately stable, with the most excited modes at $\kappa < 1$.

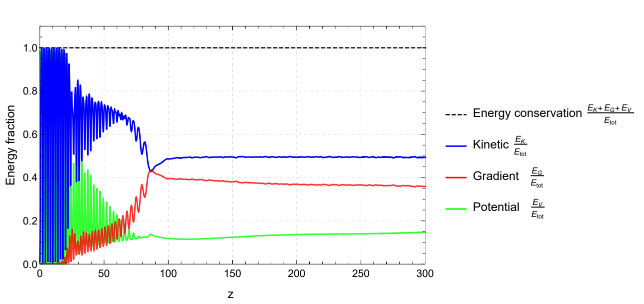

(a) Combined radial and angular energy fractions from the lattice output across the three regimes.

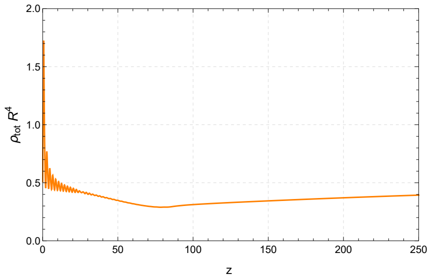

(b) Total energy density $R^4\rho$, approximately constant after the first oscillations, confirming radiation-like scaling.

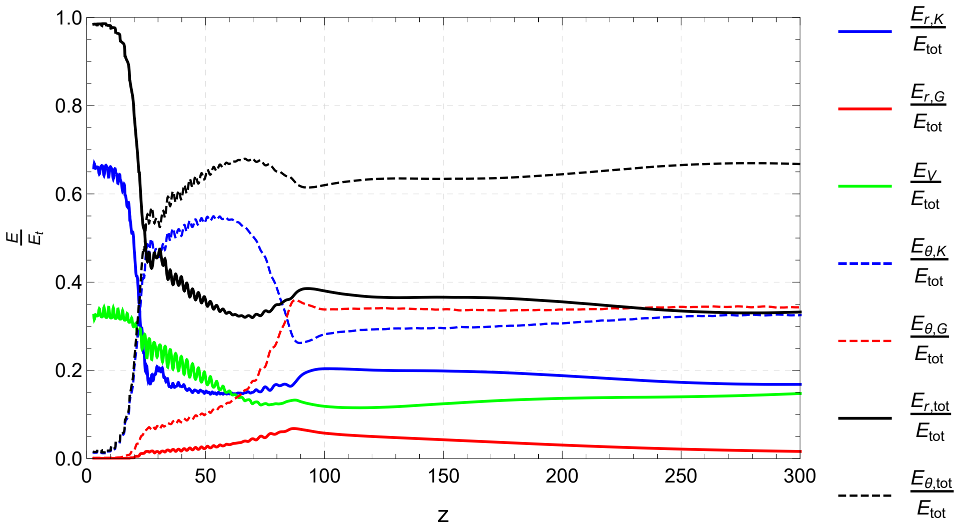

(c) Energy fraction for each contribution from the lattice output. Dashed lines correspond to angular contributions, solid lines to radial contributions.

Figure A.16: Energy density evolution across the three dynamical regimes.

A.4 Comparison with the claims of Co, Hall and Harigaya

In the paper by Co, Hall, and Harigaya [11] the mechanism is described at a qualitative level. We are therefore in a position to use our simulation to validate their claims directly. Before doing so, we remark on the generality of our results. The choice $\lambda = 10^{-3}$ does not affect the lattice equations of motion: a different coupling constant corresponds, via the identification $\omega_* = \sqrt{\lambda}\,\phi_i$, merely to a different rescaling of the time variable. Similarly, the ratio $f_a/r_i \sim 10^{-2}$ chosen for our representative run determines when the radial mass $m_S \propto \lambda^{1/2} r$ becomes dynamically important, setting $z_{\rm mass} \sim 80$; a smaller ratio would delay this threshold, extending the regime of parametric resonance accordingly.

In the following, we address the main claims of Co et al. , checking each against both the analytical results of the preceding sections and the lattice output.

The first claim is that axion modes with non-zero momenta grow rapidly from initial seeds set by quantum fluctuations, with a typical momentum of order $m_S = \sqrt{V''} = \sqrt{3\lambda r^2}$. This is confirmed in first approximation. Our analytical analysis of the Lamé equation shows that in the linear regime $z \lesssim z_{\rm br}$ the excited angular modes are concentrated in a narrow instability

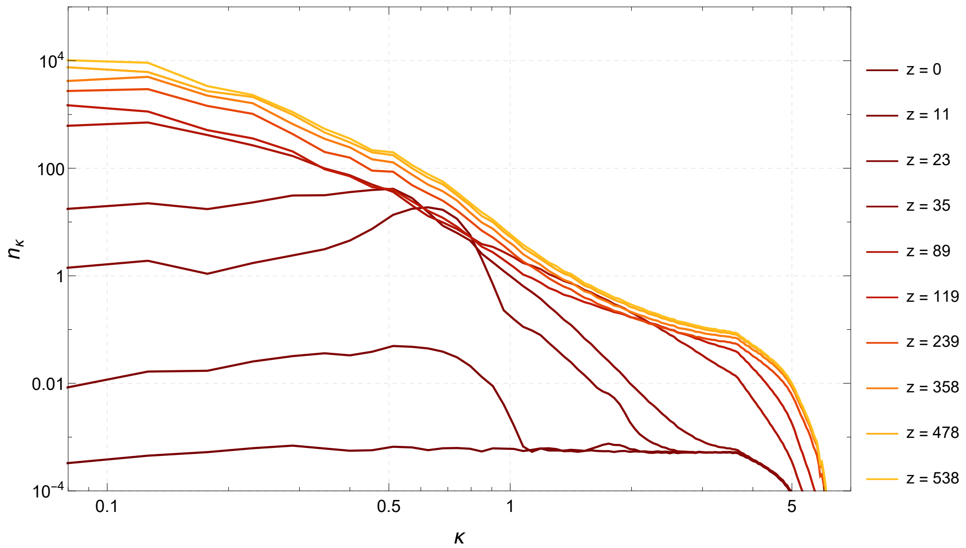

Figure A.17: Occupation number as a function of the rescaled momentum κ at different times, summing radial and angular contributions. The colour intensity decreases with time.

band around

$$\kappa_\theta \sim 0.7, \quad k_{\theta,\mathrm{com}} \sim 0.7\,\omega_i, \quad z \lesssim z_{\mathrm{br}}, \tag{A.119}$$

consistent with the claim that the typical momentum is of order $m_S \sim \omega(z)$, as shown in Fig. A.14. However, even within the formally linear regime, the lattice reveals in Fig. A.17 that scattering effects are not entirely negligible: modes below $\kappa_\theta \lesssim 0.5$ are already excited from the vacuum seeds, so the growth is not purely exponential in a single isolated band.

The second claim is that the energy of the fluctuations eventually becomes comparable to that of the radial oscillation, after which backreaction is non-negligible and parametric resonance ceases. This is also confirmed. From the lattice energy plot in Fig. A.16, the equipartition between the angular and radial sectors occurs at $z \sim z_{\mathrm{br}}$,

$$\frac{E_{r,\mathrm{tot}}}{E_{\theta,\mathrm{tot}}}(z_{\mathrm{br}}) \sim 1. \tag{A.120}$$

However, while the modes in the expected narrow instability band do stop growing after z_{br}, the spectrum in Fig. A.17 shows that other modes continue to grow exponentially. The resonance does not simply cease; rather, the instability bands are restructured by the back-reaction, with energy continuing to flow into new modes.

The third claim is that, due to efficient scattering between the oscillating radial field and the axion fluctuations, the entire zero-mode energy of the radial field is transferred into comparable radial and axion fluctuations,

$$Y_r(z_i) \sim Y_{\delta r}(z) \sim Y_{\delta\theta}(z), \quad z \gtrsim z_{\mathrm{mass}}. \tag{A.121}$$

For this point, we need further work to separate the radial number density from the angular one. For the moment, we can make energy considerations. Shortly after z_{br} the zero-mode energy is indeed rapidly depleted: by $z \sim z_{\mathrm{mass}}$ we find $E_{r,0}/E_{r,\mathrm{tot}} \sim 1\%$ from Fig. A.15, while the energy split between radial and angular sectors reaches

$$\frac{E_{r,\mathrm{tot}}}{E_{\theta,\mathrm{tot}}}(z_{\mathrm{mass}}) \sim \frac{1}{2}. \tag{A.122}$$

The fourth claim is that the production occurs at very early times, $\Gamma \sim \sqrt{3}\,\omega_i$. This is correct. The backreaction time $z_{\rm br} \sim \mathcal{O}(10)$ in rescaled conformal time happens early after the onset of oscillation, define via $H_i = w_i$, consistent with the claim.

In summary, the qualitative picture of Co et al. is supported in the first approximation by our simulation. The main refinement is that the growth of fluctuations is not purely confined to a single well-defined band, even before and after backreaction. From Fig. A.13, a huge number of lower modes get excited, possibly leading to quantitatively different results.

Directions for improving the analysis

The comparison above is semi-quantitative. The following steps would improve the precision and scope of the results. First, the radial lattice occupation number should be extracted separately by implementing the appropriate effective frequency $\omega_{r,\kappa}$ in the output, which would allow a direct test of $Y_{\delta\theta} \sim Y_{\delta r} \sim Y_{r,0}$. Secondly, a fully detailed set of convergence runs varying N, δz, and $\kappa_{\rm IR}$ should be performed to check the sensitivity of the results to the lattice discretisation. Finally, it would be valuable to map out how the key dynamical time scales $z_{\rm br}$ and $z_{\rm mass}$ depend on the parameters f_a/r_i and λ_{PQ}, to make contact with the parameter-space analysis of Co et al.

Appendix B

Stochastic inflation

The stochastic approach to inflation is based on the idea that the infrared part of the scalar field may be considered as a classical space-dependent stochastic field which satisfies a local Langevin equation [86]. In the stochastic approach, we represent the Heisenberg operator of the quantum field as

$$\phi(t,\vec{x}) = \bar{\phi}(t,\vec{x}) + \int \frac{d^3k}{(2\pi)^3}\theta(k-\epsilon R(t)H)\left[a_{\vec{k}}\phi_{\vec{k}}(t)e^{-i\vec{k}\vec{x}} + a^{\dagger}_{\vec{k}}\phi^{*}_{\vec{k}}(t)e^{i\vec{k}\vec{x}}\right]. \tag{B.1}$$

Here $\bar{\phi}$ is a coarse-grained or a long-wavelength part of ϕ, $\theta(z)$ is the step function, and ϵ is a small constant parameter. The ladder operators $a^{\dagger}_{\vec{k}}, a_{\vec{k}}$ satisfying the commutation relations,

$$[a_{\vec{k}}, a^{\dagger}_{\vec{k'}}] = (2\pi)^3\delta^{(3)}(\vec{k}-\vec{k'}) \tag{B.2}$$

In a de-Sitter background, H is taken to be constant. So, $\bar{\phi}$ is the averaged over a constant physical 3D volume slightly larger than the volume inside the event horizon. The Fokker-Planck equation for the one-point PDF $\rho_1[\bar{\phi}(t,\vec{x}) = \tilde{\phi}]$, has the form [45],

$$\frac{\partial\rho_1}{\partial t} = \frac{1}{3H}\frac{\partial}{\partial\tilde{\phi}}\{V'[\tilde{\phi}]\rho_1\} + \frac{H^3}{8\pi^2}\frac{\partial^2\rho_1}{\partial\tilde{\phi}^2}. \tag{B.3}$$

Once we have found a solution of the above equation, we can calculate the expectation value of any function $\bar{\phi}$. In particular, we will use the stochastic approach to follow the variance of the coarse-grainded field during inflation, in particular

$$\langle\bar{\phi}^2\rangle = \int d\tilde{\phi}\tilde{\phi}^2\rho_1[\tilde{\phi}]. \tag{B.4}$$

This relation explains the sense in which the transition from quantum to classical behaviour takes place here: though the scalar field remains a quantum operator formally, we can introduce an auxiliary classical stochastic scalar field $\tilde{\phi}$, with the PDF that has the same expectation values for all observables with excellent accuracy.

We introduce dimensionless variables

$$\tilde{t} \equiv H_I t, \quad y \equiv \frac{\bar{\phi}}{H_I}, \quad U \equiv \frac{V}{H_I^4}, \quad \tilde{\rho}_1 \equiv H_I\,\rho_1, \tag{B.5}$$

so that the Fokker-Planck equation becomes

$$\frac{\partial \tilde{\rho}_1[y]}{\partial \tilde{t}} = \frac{1}{3}\frac{\partial}{\partial y}\left(\tilde{\rho}_1[y]\,\frac{\partial U}{\partial y}\right) + \frac{1}{8\pi^2}\frac{\partial^2 \tilde{\rho}_1[y]}{\partial y^2} \equiv \mathbb{L}\,\tilde{\rho}_1[y]. \tag{B.6}$$

Since the Fokker–Planck operator $\mathbb{L}$ is time-independent, the general solution is

$$\tilde{\rho}_1(y,\tilde{t}) = \sum_{n=0}^{\infty} \alpha_n\,\Psi_n(y)\,e^{-\Lambda_n(\tilde{t}-\tilde{t}_0)}, \tag{B.7}$$

where $\{\Psi_n\}$ are eigenvectors of $\mathbb{L}$ with eigenvalues $\{\Lambda_n\}$. The operator $\mathbb{L}$ is not hermitian, but it can be made via the following transformation

$$\mathbb{L}_H \equiv e^{Q/2}\,\mathbb{L}\,e^{-Q/2}, \quad Q = \frac{8\pi^2}{3}\,U. \tag{B.8}$$

The Hermitian eigenvectors $\Phi_n \equiv e^{Q/2}\Psi_n$ satisfy the same eigenvalue equation $\mathbb{L}_H\Phi_n = -\Lambda_n\Phi_n$ and are orthonormal, $\int_{-\infty}^{\infty} dy\,\Phi_m^*(y)\Phi_n(y) = \delta_{mn}$.

We introduce ladder operators

$$A = \sqrt{\frac{1}{8\pi^2}}\,e^{-Q/2}\frac{\partial}{\partial y}\,e^{Q/2}, \quad A^\dagger = -\sqrt{\frac{1}{8\pi^2}}\,e^{Q/2}\frac{\partial}{\partial y}\,e^{-Q/2}, \tag{B.9}$$

which allow us to write $\mathbb{L}_H = -A^\dagger A \equiv -\mathbb{N}$, so that $\mathbb{N}\Phi_n = \Lambda_n\Phi_n$. Their commutator is

$$\left[A, A^\dagger\right] = \frac{1}{8\pi^2}\frac{\partial^2 Q}{\partial y^2} = \frac{1}{3}\frac{\partial^2 U}{\partial y^2}. \tag{B.10}$$

Pure quadratic potential

We specialise to the mass potential

$$V(\phi) = \tfrac{1}{2}m^2\phi^2 \implies U(y) = \tfrac{1}{2}\tilde{m}^2 y^2, \quad \tilde{m} \equiv \frac{m}{H_I}. \tag{B.11}$$

Then

$$\left[A, A^\dagger\right] = \frac{\tilde{m}^2}{3} = \text{const}, \tag{B.12}$$

which is exactly the algebra of a quantum harmonic oscillator. The commutators with $\mathcal{N}$ give

$$[\mathcal{N}, A] = -\frac{\tilde{m}^2}{3}\,A, \quad [\mathcal{N}, A^\dagger] = +\frac{\tilde{m}^2}{3}\,A^\dagger, \tag{B.13}$$

so A and $A^\dagger$ lower and raise the eigenvalue by $\tilde{m}^2/3$. Since $\Lambda_n = (A\Phi_n, A\Phi_n) \geq 0$, the spectrum is

$$\Lambda_n = n\,\frac{\tilde{m}^2}{3} = n\,\frac{m^2}{3H_I^2}, \quad n = 0, 1, 2, \ldots \tag{B.14}$$

Setting $\beta \equiv 4\pi^2\tilde{m}^2/3$, the eigenvalue equation for Φ_n reduces to

$$\Phi_n''(\tilde{y}) + \left(2n + 1 - \tilde{y}^2\right)\Phi_n(\tilde{y}) = 0, \quad \tilde{y} \equiv \sqrt{\beta}\,y, \tag{B.15}$$

whose normalisable solutions are

$$\Phi_n(\tilde{y}) = c_n\, e^{-\tilde{y}^2/2}\, H_n(\tilde{y}), \quad c_n = \frac{1}{\sqrt{2^n n!}}\left(\frac{\beta}{\pi}\right)^{1/4}, \tag{B.16}$$

with H_n the Hermite polynomials. The eigenfunctions $\Psi_n = e^{-Q/2}\Phi_n = e^{-\beta y^2/2}\Phi_n$ are therefore

$$\Psi_n(y) = \frac{1}{\sqrt{2^n n!}}\left(\frac{\beta}{\pi}\right)^{1/4} H_n\Big(\sqrt{\beta}\, y\Big)\, e^{-\beta y^2}. \tag{B.17}$$

Assuming the field is exactly at the origin at the onset of inflation, $\tilde{\rho}_1(y, \tilde{t}_0) = \delta(y)$, the expansion coefficients are

$$\alpha_n = \begin{cases} \left(\frac{\beta}{\pi}\right)^{1/4} \frac{(-1)^{n/2}}{(n/2)!}\sqrt{\frac{n!}{2^n}}, & n \text{ even}, \\ 0, & n \text{ odd}. \end{cases} \tag{B.18}$$

Using the orthogonality of Hermite polynomials, $\int_{-\infty}^{\infty} d\tilde{y}\, e^{-\tilde{y}^2} H_m(\tilde{y}) H_n(\tilde{y}) = 2^n \sqrt{\pi}\, n!\, \delta_{mn}$, only the $n = 0$ and $n = 2$ terms contribute to $\langle y^2 \rangle$:

$$\begin{aligned} \langle y^2\rangle(\tilde{t}) &= \int_{-\infty}^{\infty} dy\; y^2\, \tilde{\rho}_1(y, \tilde{t}) \\ &= \underbrace{\sqrt{\frac{\beta}{\pi}}\int_{-\infty}^{\infty} dy\; y^2 e^{-\beta y^2}}_{=1/(2\beta)} - \frac{1}{4}\sqrt{\frac{\beta}{\pi}}\exp\left\{-\frac{2\tilde{m}^2(\tilde{t}-\tilde{t}_0)}{3}\right\} \underbrace{\int_{-\infty}^{\infty} dy\; y^2 H_2\Big(\sqrt{\beta}\, y\Big)\, e^{-\beta y^2}}_{=2\sqrt{\pi}/\beta^{3/2}} \\ &= \frac{1}{2\beta}\left[1 - \exp\left\{-\frac{2\tilde{m}^2(\tilde{t}-\tilde{t}_0)}{3}\right\}\right]. \end{aligned} \tag{B.19}$$

The number of e-folds N elapsed since the start of inflation satisfies $\tilde{t} - \tilde{t}_0 = N$, so restoring dimensionful quantities ($\beta = 4\pi^2 m^2/(3H_I^2)$, $\langle\bar{\phi}^2\rangle = H_I^2\langle y^2\rangle$) we obtain

$$\langle\bar{\phi}^2\rangle(N) = \frac{3H_I^4}{8\pi^2 m^2}\left[1 - \exp\left(-N\,\frac{2m^2}{3H_I^2}\right)\right]. \tag{B.20}$$

For $N \gg 3H_I^2/(2m^2)$ the exponential is suppressed and the field reaches its equilibrium (de Sitter invariant) variance

$$\langle\bar{\phi}^2\rangle_{\text{eq}} \approx \frac{3H_I^4}{8\pi^2 m^2}. \tag{B.21}$$

This equilibration requires $N \gtrsim 3H_I^2/(2m^2)$, which is a large number of e-folds when $m \ll H_I$. This result is equal to the one we can find in the Hartree-Fock regime [87], in which thea case of pure massive term is exact.

Pure quartic potential

We now consider the massless self-interacting case

$$V(\phi) = \frac{\lambda}{4}\phi^4 \implies U(y) = \frac{\lambda}{4}y^4. \tag{B.22}$$

The commutator of the ladder operators is now

$$\left[A, A^{\dagger}\right] = \frac{1}{3}\frac{\partial^2 U}{\partial y^2} = \lambda y^2, \tag{B.23}$$

which is *field-dependent*. The harmonic-oscillator analogy breaks down and no closed-form spectral decomposition exists; the eigenvalue problem must be treated numerically.

But there is a general equilibrium solution of the Fokker–Planck equation, with $\Lambda_0 = 0$, is

$$\rho_{1,\mathrm{eq}}(\phi) = \mathcal{N}^{-1}\exp\left(-\frac{8\pi^2}{3}U\right) = \mathcal{N}^{-1}\exp\left(-\frac{2\pi^2\lambda}{3H_I^4}\phi^4\right), \tag{B.24}$$

where $\mathcal{N}$ is the normalization constant [45]. This distribution is significantly *non-Gaussian*: it has negative kurtosis $K = \langle\phi^4\rangle/\langle\phi^2\rangle^2 - 3 \approx -0.812$.

The normalization integrals reduce to Gamma functions. Setting $\alpha \equiv 2\pi^2\lambda/(3H_I^4)$, one uses

$$\int_0^{\infty} dy\, y^{2n}\, e^{-\alpha y^4} = \frac{1}{4}\,\alpha^{-(2n+1)/4}\,\Gamma\left(\frac{2n+1}{4}\right), \tag{B.25}$$

to obtain

$$\left\langle\phi^2\right\rangle_{\mathrm{eq}} = \frac{\displaystyle\int_{-\infty}^{\infty} d\phi\, \phi^2\, e^{-\alpha\phi^4}}{\displaystyle\int_{-\infty}^{\infty} d\phi\, e^{-\alpha\phi^4}} = \frac{\Gamma(3/4)}{\Gamma(1/4)}\,\alpha^{-1/2}. \tag{B.26}$$

Restoring all factors this gives [45]

$$\left\langle\phi^2\right\rangle_{\mathrm{eq}} = \frac{\Gamma(3/4)}{\Gamma(1/4)}\sqrt{\frac{3}{2\pi^2\lambda}}\,H_I^2 \approx 0.132\,\frac{H_I^2}{\sqrt{\lambda}}. \tag{B.27}$$

This result is non-perturbative in λ: the variance scales as $\lambda^{-1/2}$ rather than as a power series in λ, reflecting the complete breakdown of perturbation theory around the free-field solution for $m^2 \lesssim H_I^2$.

From Ref. [45], the number of e-folds to reach the equilibrium are approximately given by

$$N > \frac{10}{\sqrt{\lambda}}. \tag{B.28}$$

Appendix C

Fitting the WKB approximation to the full solution

In the standard misalignment mechanism, as discussed in Section 1.2.2, the transition between the overdamped and the oscillatory regimes is definedby the sharp matching condition,

$$3H(t_{\rm osc}) = M(t_{\rm osc}). \tag{C.1}$$

In this chapter, we estimate the accuracy of this approximation by determining the effective matching parameter x, defined via

$$xH = M, \tag{C.2}$$

such that the late-time analytical (WKB) solution reproduces the amplitude of the full numerical solution.

The equation of motion in RD for a homogeneous, free massive scalar field is,

$$\ddot{\phi} + \frac{3}{2t}\dot{\phi} + m^2\phi = 0, \quad \dot{} \equiv \frac{d}{dt}. \tag{C.3}$$

We impose the initial conditions,

$$\phi(t_i) = 0, \quad \dot{\phi}(t_i) = 0. \tag{C.4}$$

Analytical solution

As discussed in Section 1.2.2, the solution is described in two regimes,

$$\begin{cases} \phi(t) = \phi_i & t_i < t < t_{\rm osc} \\ \phi(t) = \phi_{\rm wkb}(t) & t > t_{\rm osc} \end{cases}. \tag{C.5}$$

To compare with the numerical solution, we compute the WKB solution including the leading correction in $\frac{m}{H}$. Changing variable, $\gamma(t) = t^{3/4}\phi(t)$, the equation of motion can be rewritten as

$$\ddot{\gamma}(t) + \left(m^2(t) + \frac{3H^2(t)}{4}\right)\gamma(t) = 0. \tag{C.6}$$

In this form, it is a harmonic oscillator with a time-dependent frequency, damped by the expansion of the universe,

$$w(t) = \sqrt{\left(m^2 + \frac{3H^2(t)}{4}\right)}. \tag{C.7}$$

The WKB approximation is valid when

$$\left|\frac{\dot{w}}{w^2}\right| = \frac{1}{1+\frac{3H^2}{4m^2}}\left(\frac{3H^3}{8m^3}\right) \ll 1. \tag{C.8}$$

Then, for $t > t_{\rm osc}$, the analytical solution can be derived as,

$$\phi_{\rm wkb}(t) \simeq A\sqrt{\frac{w(t_{osc})R^3(t_{osc})}{w(t)R^3(t)}}\cos\left(\int_{t_{osc}}^{t} w(\tilde{t})d\tilde{t} + \theta\right), \tag{C.9}$$

where the integration constant A, θ are fixed at the matching time $t_{\rm osc}$, defined by

$$xH(t_{\rm osc}) = w(t_{\rm osc}). \tag{C.10}$$

The parameter x will be determined by requiring the late-time analytical amplitude

$$A_{\rm wkb}(t,x) = A\sqrt{\frac{w(t_{\rm osc})R^3(t_{\rm osc})}{w(t)R^3(t)}}, \tag{C.11}$$

matches the numerical one.

Numerical solution

The differential equation (C.3) can be solved numerically. A direct integration is not straightforward: the field begins nearly constant and later enters a regime of rapid oscillations, where a fixed-step integrator loses accuracy. We therefore proceed in two stages. First, we integrate numerically from the initial time until the system is well within the oscillatory regime, where the numerical solution remains reliable. We then match onto the analytical WKB solution, with the same form of Eq. (C.9), but at matching time $t_{\rm match} \gg t_{\rm osc}$. Indeed, the dominant deviation from the sharp-boundary approximation arises near $t_{\rm osc}$, while the late-time WKB solution is insensitive to the matching point once $t_{\rm match}$ lies deep in the oscillatory regime.

To handle the full dynamical range, it is convenient to change integration variable and work with an order-unity dimensionless field. We define

$$z(T) = \ln\left(\frac{R(T)}{R_0}\right) = \ln\left(\frac{T_0}{T}\right) + \frac{1}{3}\ln\left(\frac{g_*(T_0)}{g_*(T)}\right), \quad y(z) = \frac{\phi}{f_a}, \tag{C.12}$$

where entropy conservation (1.19) has been used and $z_0 = 0$ corresponds to the initial time. The equation of motion can be rewritten as

$$y''(z) + y'(z) + \left(\frac{m(z)}{H_0}\right)^2 e^{4(z-z_0)}y(z) = 0. \tag{C.13}$$

To capture the onset of the oscillations, we numerically integrate in $z \in \{z(T_0), z(T_f)\}$, where the temperatures are defined as

$$H(T_0) = 10^2 m(T_0), \quad H(T_f) = 10^{-2}m(T_f). \tag{C.14}$$

so that the integration begins well in the overdamped regime and ends well within the oscillatory regime. The Hubble rate in RD is

$$H(T) = \sqrt{\frac{g_*(T)\pi^2}{90}}\frac{T^2}{M_{\rm pl}}, \tag{C.15}$$

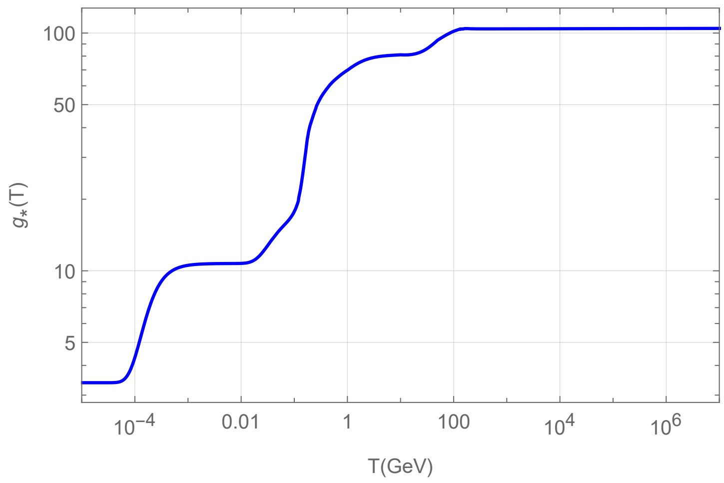

Figure C.1: Interpolating function of the effective degrees of freedom $g_*(T)$

where $g_*(T)$ is obtained from an interpolation function fitted to the data of Ref. [88], shown in Fig. C.1

The resulting numerical solution is shown in Fig. C.2. To extend the solution to late times where oscillations become rapid, we match onto the WKB solution at t_{match}, defined as

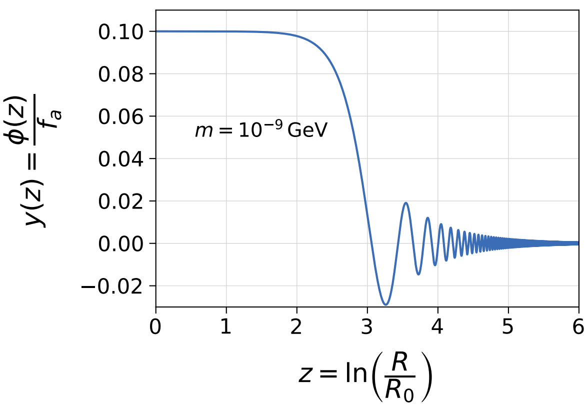

Figure C.2: Numerical solution of the EOM for a free massive scalar field in a radiation-dominated universe.

$$\frac{H(t_{\text{match}})}{m(t_{\text{match}})} = 10^{-1}. \tag{C.16}$$

The amplitude is then defined as

$$A^N_{\text{wkb}}(t) = A^N \sqrt{\frac{w(t_{\text{match}})R^3(t_{\text{match}})}{w(t)R^3(t)}} \tag{C.17}$$

Estimation of x

We have obtained two expressions for the late-time amplitude: the analytical one $A_{\text{wkb}}(t, x)$, defined with a sharp matching boundary at $xH = m$, and the numerical one $A^N_{\text{wkb}}(t)$. Requiring these to agree at later times yields

$$1 = \frac{A_{\rm wkb}(t,x)}{A^N_{\rm wkb}(t)} = \frac{A}{A^N}\left(x\frac{H_{\rm osc}}{m}\right)^{3/4}\sqrt{\frac{w_{\rm osc}}{w_{\rm match}}} \tag{C.18}$$

Since $\frac{H_{\rm osc}}{m} = \frac{1}{x}$, the dependence on the mass drops out at leading order, and one finds

$$x = 1.6\ . \tag{C.19}$$

This result shows that the conventional condition $3H(t_{osc}) = m(t_{osc})$ underestimates the true matching time, introducing an error of $\mathcal{O}(1)$ in the final field amplitude.

Appendix D

χ scattering rate in the Early Universe

.

The scattering rate of the radial field χ with particles in the thermal bath determines whether the radial condensate thermalizes or remains non-thermal and subsequently contributes to the DM abundance. The dominant interactions depend on the temperature of the Universe.

The interactions follow from Chapter 3. Throughout this chapter we assume the radiatively stable regime,

$$\lambda_{H\Phi} \ll \frac{m_\chi}{f_a}, \quad |\sin(\theta)| \lesssim \frac{m_\chi}{m_h}. \tag{D.1}$$

$T_{\rm EW} \ll T < f_a$

For temperatures above the electroweak phase transition, electroweak symmetry is restored and the Higgs field is effectively massless for $T > m_h$. In the broken PQ phase,

$$|\Phi| = \frac{f_a + \chi}{2}. \tag{D.2}$$

The relevant processes are

$$\chi H \leftrightarrow \chi H, \quad HH \leftrightarrow \chi\chi, \quad HH \to HH\chi. \tag{D.3}$$

Using NDA and the relativistic Higgs number density $n_H \sim T^3$, the first two processes give

$$\Gamma(\chi H \leftrightarrow \chi H) \sim \Gamma(HH \leftrightarrow \chi\chi) \sim \lambda_{H\Phi}^2 T. \tag{D.4}$$

Comparing with the Hubble rate during RD,

$$H(T) \simeq \frac{T^2}{M_{\rm pl}}, \tag{D.5}$$

shows that these interactions do not reach thermal equilibrium for

$$T > m_h, \quad \lambda_{H\Phi} \ll \frac{m_\chi}{f_a}. \tag{D.6}$$

The three-body process is enhanced by powers of f_a,

$$\Gamma(HH \to HH\chi) \sim 10^{-3}\,\frac{\lambda_H^2 \lambda_{H\Phi}^2 f_a^2}{T}. \tag{D.7}$$

The condition $\Gamma > H$ yields

$$10^2\,\mathrm{GeV} \ll T_{\mathrm{eff}} < 10^2\,\mathrm{GeV}\left(10^4 \frac{m_\chi^2}{\mathrm{MeV}^2}\right)^{1/3}. \tag{D.8}$$

A solution exists for

$$m_\chi \gg 10^{-2}\,\mathrm{MeV}. \tag{D.9}$$

Therefore, thermal radial mode production through the Higgs portal is possible in a region of parameter space even in the small-mixing regime.

$T_{\mathrm{QCD}} \ll T \ll T_{\mathrm{EW}}$

For

$$T_{\mathrm{QCD}} \ll T \ll T_{\mathrm{EW}}, \tag{D.10}$$

the Higgs vacuum expectation value is restored and the interactions are described by the broken electroweak phase. The relativistic degrees of freedom in the thermal bath are

$$\psi \in \{e, \mu, \tau, u, d, s, c, b, g, \gamma\}. \tag{D.11}$$

The relevant scattering processes are

$$\chi\psi \leftrightarrow \chi\psi, \quad \chi\psi' \leftrightarrow \psi\psi, \quad \chi\psi' \leftrightarrow \psi'\psi. \tag{D.12}$$

For elastic scattering,

$$\Gamma(\chi\psi \to \chi\psi) \simeq g_{\chi\psi\psi}^4\, T. \tag{D.13}$$

Using

$$\sin(\theta) \lesssim \frac{m_\chi}{m_h}, \tag{D.14}$$

this interaction never becomes efficient for

$$T > T_{\mathrm{QCD}}, \quad m_\chi < \mathrm{MeV}, \tag{D.15}$$

assuming perturbative Yukawa couplings,

$$g_{h\psi\psi} < 1. \tag{D.16}$$

The dominant channels are instead QCD-mediated,

$$\chi g \leftrightarrow \bar{q}q, \quad \chi q \leftrightarrow gq. \tag{D.17}$$

For the first process,

$$\Gamma(\chi g \leftrightarrow \bar{q}q) \sim \frac{\alpha_s^3}{16\pi^2 v^2} \sin^2\theta\, T^3. \tag{D.18}$$

Requiring $\Gamma > H$ gives efficient scattering for

$$m_\chi \gtrsim 10^{-1}\,\mathrm{MeV}, \tag{D.19}$$

while maintaining

$$\sin(\theta) \lesssim \frac{m_\chi}{m_h}. \tag{D.20}$$

For the second process,

$$\Gamma(\chi q \leftrightarrow gq) \sim \alpha_s \, \sin^2\theta \, g_{\chi\bar{q}q}^2 \, T. \tag{D.21}$$

The condition $\Gamma > H$ implies

$$m_q < T_{\mathrm{eff}} < M_{\mathrm{pl}}\,\alpha_s\, \sin^2\theta \, \frac{m_q^2}{v^2}, \tag{D.22}$$

with relativistic quarks satisfying

$$m_q \ll T. \tag{D.23}$$

Efficient scattering can occur through the charm and bottom quarks for

$$m_\chi \gtrsim 10^{-2}\,\mathrm{MeV}. \tag{D.24}$$

$m_\chi \ll T \ll \Lambda_{\mathrm{QCD}}$

Below the confinement scale, the relativistic degrees of freedom are

$$\gamma, \quad e, \quad \mu. \tag{D.25}$$

Neutrinos are neglected since their interactions arise only at loop level. The relevant processes are

$$\chi\ell \leftrightarrow \ell\gamma, \quad \chi\gamma \leftrightarrow \bar{f}f, \tag{D.26}$$

with

$$\ell \in \{e, \mu\}. \tag{D.27}$$

The corresponding rates are

$$\Gamma(\chi\ell \leftrightarrow \ell\gamma) \sim \alpha_{\mathrm{em}} \, \sin^2\theta \, g_{h\bar{\ell}\ell}^2 \, T, \tag{D.28}$$

and

$$\Gamma(\chi\gamma \leftrightarrow \bar{f}f) \sim \frac{\alpha_{\mathrm{em}}^3}{16\pi^2 v^2} \sin^2\theta. \tag{D.29}$$

Both rates remain below the Hubble expansion rate throughout this temperature range,

$$\Gamma < H, \tag{D.30}$$

and therefore these interactions never become efficient.

Bibliography

1. Weinberg, S. A New Light Boson? *Phys. Rev. Lett.* **40,** 223–226. `https://link.aps.org/doi/10.1103/PhysRevLett.40.223` (4 Jan. 1978).
2. Wilczek, F. Problem of Strong P and T Invariance in the Presence of Instantons. *Phys. Rev. Lett.* **40,** 279–282. `https://link.aps.org/doi/10.1103/PhysRevLett.40.279` (5 Jan. 1978).
3. Peccei, R. D. & Quinn, H. R. CP Conservation in the Presence of Pseudoparticles. *Phys. Rev. Lett.* **38,** 1440–1443. `https://link.aps.org/doi/10.1103/PhysRevLett.38.1440` (25 June 1977).
4. Peccei, R. D. & Quinn, H. R. Constraints imposed by CP conservation in the presence of pseudoparticles. *Phys. Rev. D* **16,** 1791–1797. `https://link.aps.org/doi/10.1103/PhysRevD.16.1791` (6 Sept. 1977).
5. Abbott, L. & Sikivie, P. A cosmological bound on the invisible axion. *Physics Letters B* **120,** 133–136. ISSN: 0370-2693. `https://www.sciencedirect.com/science/article/pii/037026938390638X` (1983).
6. Dine, M. & Fischler, W. The not-so-harmless axion. *Physics Letters B* **120,** 137–141. ISSN: 0370-2693. `https://www.sciencedirect.com/science/article/pii/0370269383906391` (1983).
7. Preskill, J., Wise, M. B. & Wilczek, F. Cosmology of the invisible axion. *Physics Letters B* **120,** 127–132. ISSN: 0370-2693. `https://www.sciencedirect.com/science/article/pii/0370269383906378` (1983).
8. Davis, R. L. Cosmic Axions from Cosmic Strings. *Phys. Lett. B* **180,** 225–230 (1986).
9. Harari, D. & Sikivie, P. On the Evolution of Global Strings in the Early Universe. *Phys. Lett. B* **195,** 361–365 (1987).
10. Adams, C. B. *et al. Axion Dark Matter* in *Snowmass 2021* (Mar. 2022). arXiv: `2203.14923 [hep-ex]`.
11. Co, R. T., Hall, L. J. & Harigaya, K. QCD Axion Dark Matter with a Small Decay Constant. *Phys. Rev. Lett.* **120,** 211602. arXiv: `1711.10486 [hep-ph]` (2018).
12. Armengaud, E. *et al.* Physics potential of the International Axion Observatory (IAXO). *JCAP* **06,** 047. arXiv: `1904.09155 [hep-ph]` (2019).
13. *Nature Physics* **13,** 584–590. ISSN: 1745-2481. `http://dx.doi.org/10.1038/nphys4109` (May 2017).
14. Caldwell, A. *et al.* Dielectric Haloscopes: A New Way to Detect Axion Dark Matter. *Physical Review Letters* **118.** ISSN: 1079-7114. `http://dx.doi.org/10.1103/PhysRevLett.118.091801` (Mar. 2017).
15. Liu, J. *et al.* Broadband Solenoidal Haloscope for Terahertz Axion Detection. *Phys. Rev. Lett.* **128,** 131801. arXiv: `2111.12103 [physics.ins-det]` (2022).
16. Kolb, E. W. & Turner, M. S. *The Early Universe* ISBN: 978-0-429-49286-0, 978-0-201-62674-2 (Taylor and Francis, May 2019).
17. Carroll, S. M. *Spacetime and geometry* (Cambridge University Press, 2019).

18. Planck Collaboration *et al.* Planck 2018 results - VI. Cosmological parameters. *A&A* **641,** A6. https://doi.org/10.1051/0004-6361/201833910 (2020).
19. Riess, A. G. *et al.* A Comprehensive Measurement of the Local Value of the Hubble Constant with 1 km s^{-1} Mpc^{-1} Uncertainty from the Hubble Space Telescope and the SH0ES Team. *Astrophys. J. Lett.* **934,** L7. arXiv: 2112.04510 [astro-ph.CO] (2022).
20. Cirelli, M., Strumia, A. & Zupan, J. Dark Matter. arXiv: 2406.01705 [hep-ph] (June 2024).
21. Akrami, Y. *et al.* Planck 2018 results. X. Constraints on inflation. *Astron. Astrophys.* **641,** A10. arXiv: 1807.06211 [astro-ph.CO] (2020).
22. Clowe, D. *et al.* A Direct Empirical Proof of the Existence of Dark Matter. *The Astrophysical Journal* **648,** L109–L113. ISSN: 1538-4357. http://dx.doi.org/10.1086/508162 (Aug. 2006).
23. Lelli, F., McGaugh, S. S. & Schombert, J. M. SPARC: MASS MODELS FOR 175 DISK GALAXIES WITH SPITZER PHOTOMETRY AND ACCURATE ROTATION CURVES. *The Astronomical Journal* **152,** 157. ISSN: 1538-3881. http://dx.doi.org/10.3847/0004-6256/152/6/157 (Nov. 2016).
24. Gorbunov, D. S. & Rubakov, V. A. *Introduction to the theory of the early universe: Cosmological perturbations and inflationary theory* (World Scientific, 2011).
25. Wentzel, G. Eine Verallgemeinerung der Quantenbedingungen für die Zwecke der Wellenmechanik. *Z. Phys.* **38,** 518–529 (1926).
26. Kramers, H. A. Wellenmechanik und halbzahlige Quantisierung. *Z. Phys.* **39,** 828–840 (1926).
27. Brillouin, L. La mécanique ondulatoire de Schrödinger; une méthode générale de resolution par approximations successives. *Compt. Rend. Hebd. Seances Acad. Sci.* **183,** 24–26 (1926).
28. Arias, P. *et al.* WISPy Cold Dark Matter. *JCAP* **06,** 013. arXiv: 1201.5902 [hep-ph] (2012).
29. Jordan, D. & Smith, P. *Nonlinear ordinary differential equations: an introduction for scientists and engineers* (Oxford University Press, 2007).
30. Di Luzio, L., Giannotti, M., Nardi, E. & Visinelli, L. The landscape of QCD axion models. *Phys. Rept.* **870,** 1–117. arXiv: 2003.01100 [hep-ph] (2020).
31. Marsh, D. J. E. Axion Cosmology. *Phys. Rept.* **643,** 1–79. arXiv: 1510.07633 [astro-ph.CO] (2016).
32. Coleman, S. *Aspects of Symmetry: Selected Erice Lectures* ISBN: 978-0-521-31827-3 (Cambridge University Press, Cambridge, U.K., 1985).
33. Crewther, R., Di Vecchia, P., Veneziano, G. & Witten, E. Chiral estimate of the electric dipole moment of the neutron in quantum chromodynamics. *Physics Letters B* **88,** 123–127. ISSN: 0370-2693. https://www.sciencedirect.com/science/article/pii/037026937990128X (1979).
34. Baker, C. A. *et al.* Improved Experimental Limit on the Electric Dipole Moment of the Neutron. *Phys. Rev. Lett.* **97,** 131801. https://link.aps.org/doi/10.1103/PhysRevLett.97.131801 (13 Sept. 2006).
35. Vafa, C. & Witten, E. Parity Conservation in Quantum Chromodynamics. *Phys. Rev. Lett.* **53,** 535–536. https://link.aps.org/doi/10.1103/PhysRevLett.53.535 (6 Aug. 1984).
36. Dine, M. & Fischler, W. The Not So Harmless Axion. *Phys. Lett. B* **120** (ed Srednicki, M. A.) 137–141 (1983).
37. Grifols, J. A., Masso, E. & Toldra, R. Gravitinos from gravitational collapse. *Phys. Rev. D* **57,** 614–616. arXiv: hep-ph/9707536 (1998).

38. Arvanitaki, A., Baryakhtar, M. & Huang, X. Discovering the QCD axion with black holes and gravitational waves. *Physical Review D* **91.** ISSN: 1550-2368. `http://dx.doi.org/10.1103/PhysRevD.91.084011` (Apr. 2015).
39. Kim, J. E. Weak-Interaction Singlet and Strong CP Invariance. *Phys. Rev. Lett.* **43,** 103–107. `https://link.aps.org/doi/10.1103/PhysRevLett.43.103` (2 July 1979).
40. Shifman, M., Vainshtein, A. & Zakharov, V. Can confinement ensure natural CP invariance of strong interactions? *Nuclear Physics B* **166,** 493–506. ISSN: 0550-3213. `https://www.sciencedirect.com/science/article/pii/0550321380902096` (1980).
41. Crotty, P., García-Bellido, J., Lesgourgues, J. & Riazuelo, A. Bounds on Isocurvature Perturbations from Cosmic Microwave Background and Large Scale Structure Data. *Physical Review Letters* **91.** ISSN: 1079-7114. `http://dx.doi.org/10.1103/PhysRevLett.91.171301` (Oct. 2003).
42. Wantz, O. & Shellard, E. P. S. Axion Cosmology Revisited. *Phys. Rev. D* **82,** 123508. arXiv: `0910.1066 [astro-ph.CO]` (2010).
43. Kibble, T. W. B. Topology of Cosmic Domains and Strings. *J. Phys. A* **9,** 1387–1398 (1976).
44. Baumann, D. Primordial Cosmology. *PoS* **TASI2017,** 009. arXiv: `1807.03098 [hep-th]` (2018).
45. Starobinsky, A. A. & Yokoyama, J. Equilibrium state of a selfinteracting scalar field in the De Sitter background. *Phys. Rev. D* **50,** 6357–6368. arXiv: `astro-ph/9407016` (1994).
46. Planck Collaboration *et al.* Planck intermediate results - LVII. Joint Planck LFI and HFI data processing. *A&A* **643,** A42. `https://doi.org/10.1051/0004-6361/202038073` (2020).
47. Co, R. T., Hall, L. J. & Harigaya, K. Axion Kinetic Misalignment Mechanism. *Phys. Rev. Lett.* **124,** 251802. arXiv: `1910.14152 [hep-ph]` (2020).
48. Peskin, M. E. & Schroeder, D. V. *An Introduction to quantum field theory* ISBN: 978-0-201-50397-5, 978-0-429-50355-9, 978-0-429-49417-8 (Addison-Wesley, Reading, USA, 1995).
49. Figueroa, D. G. & Torrenti, F. Parametric resonance in the early Universe—a fitting analysis. *JCAP* **02,** 001. arXiv: `1609.05197 [astro-ph.CO]` (2017).
50. Burgess, C. P., Pospelov, M. & ter Veldhuis, T. The Minimal model of nonbaryonic dark matter: A Singlet scalar. *Nucl. Phys. B* **619,** 709–728. arXiv: `hep-ph/0011335` (2001).
51. Davoudiasl, H., Kitano, R., Li, T. & Murayama, H. The New minimal standard model. *Phys. Lett. B* **609,** 117–123. arXiv: `hep-ph/0405097` (2005).
52. Robens, T. & Stefaniak, T. Status of the Higgs Singlet Extension of the Standard Model after LHC Run 1. *Eur. Phys. J. C* **75,** 104. arXiv: `1501.02234 [hep-ph]` (2015).
53. Falkowski, A., Gross, C. & Lebedev, O. A second Higgs from the Higgs portal. *JHEP* **05,** 057. arXiv: `1502.01361 [hep-ph]` (2015).
54. Lee, B. W., Quigg, C. & Thacker, H. B. Weak Interactions at Very High-Energies: The Role of the Higgs Boson Mass. *Phys. Rev. D* **16,** 1519 (1977).
55. Chen, C.-Y., Dawson, S. & Lewis, I. M. Exploring resonant di-Higgs boson production in the Higgs singlet model. *Phys. Rev. D* **91,** 035015. arXiv: `1410.5488 [hep-ph]` (2015).
56. Elias-Miro, J., Espinosa, J. R., Giudice, G. F., Lee, H. M. & Strumia, A. Stabilization of the Electroweak Vacuum by a Scalar Threshold Effect. *JHEP* **06,** 031. arXiv: `1203.0237 [hep-ph]` (2012).
57. Shifman, M. A., Vainshtein, A. I., Voloshin, M. B. & Zakharov, V. I. Low-Energy Theorems for Higgs Boson Couplings to Photons. *Sov. J. Nucl. Phys.* **30,** 711–716 (1979).
58. Junnarkar, P. M. & Walker-Loud, A. Scalar strange content of the nucleon from lattice QCD. *Phys. Rev. D* **87,** 114510. `https://link.aps.org/doi/10.1103/PhysRevD.87.114510` (11 June 2013).

59. 't Hooft, G. Naturalness, chiral symmetry, and spontaneous chiral symmetry breaking. *NATO Sci. Ser. B* **59** (eds 't Hooft, G. *et al.*) 135–157 (1980).
60. Foot, R., Kobakhidze, A., McDonald, K. L. & Volkas, R. R. Poincaré protection for a natural electroweak scale. *Phys. Rev. D* **89,** 115018. arXiv: `1310.0223 [hep-ph]` (2014).
61. Bergsma, F. *et al.* Search for Axion Like Particle Production in 400-GeV Proton - Copper Interactions. *Phys. Lett. B* **157,** 458–462 (1985).
62. Artamonov, A. V. *et al.* Study of the decay $K^+ \to \pi^+ \nu\bar{\nu}$ in the momentum region $140 < P_\pi < 199$ MeV/c. *Phys. Rev. D* **79,** 092004. arXiv: `0903.0030 [hep-ex]` (2009).
63. Schmidt-Hoberg, K., Staub, F. & Winkler, M. W. Constraints on light mediators: confronting dark matter searches with B physics. *Phys. Lett. B* **727,** 506–510. arXiv: `1310.6752 [hep-ph]` (2013).
64. Aubert, B. *et al.* Direct CP, Lepton Flavor and Isospin Asymmetries in the Decays $B \to K^{(*)}\ell^+\ell^-$. *Phys. Rev. Lett.* **102,** 091803. arXiv: `0807.4119 [hep-ex]` (2009).
65. Wei, J. .-. *et al.* Measurement of the Differential Branching Fraction and Forward-Backward Asymmetry for $B \to K^{(*)}\ell^+\ell^-$. *Phys. Rev. Lett.* **103,** 171801. arXiv: `0904.0770 [hep-ex]` (2009).
66. Bar, N., Blum, K. & D'Amico, G. Is there a supernova bound on axions? *Phys. Rev. D* **101,** 123025. arXiv: `1907.05020 [hep-ph]` (2020).
67. Hardy, E. & Lasenby, R. Stellar cooling bounds on new light particles: plasma mixing effects. *JHEP* **02,** 033. arXiv: `1611.05852 [hep-ph]` (2017).
68. Fiorillo, D. F. G., Lella, A., O'Hare, C. A. J. & Vitagliano, E. Leading Bounds on Micrometer to Picometer Fifth Forces from Neutron Star Cooling. *Phys. Rev. Lett.* **135,** 211003. arXiv: `2506.19906 [hep-ph]` (2025).
69. Flacke, T., Frugiuele, C., Fuchs, E., Gupta, R. S. & Perez, G. Phenomenology of relaxion-Higgs mixing. *JHEP* **06,** 050. arXiv: `1610.02025 [hep-ph]` (2017).
70. Tino, G., Cacciapuoti, L., Capozziello, S., Lambiase, G. & Sorrentino, F. Precision gravity tests and the Einstein Equivalence Principle. *Progress in Particle and Nuclear Physics* **112,** 103772. ISSN: 0146-6410. `https://www.sciencedirect.com/science/article/pii/S0146641020300193` (2020).
71. Hoskins, J. K., Newman, R. D., Spero, R. & Schultz, J. Experimental tests of the gravitational inverse-square law for mass separations from 2 to 105 cm. *Phys. Rev. D* **32,** 3084–3095. `https://link.aps.org/doi/10.1103/PhysRevD.32.3084` (12 Dec. 1985).
72. Kapner, D. J. *et al.* Tests of the Gravitational Inverse-Square Law below the Dark-Energy Length Scale. *Phys. Rev. Lett.* **98,** 021101. `https://link.aps.org/doi/10.1103/PhysRevLett.98.021101` (2 Jan. 2007).
73. Yang, S.-Q. *et al.* Test of the Gravitational Inverse Square Law at Millimeter Ranges. *Phys. Rev. Lett.* **108,** 081101. `https://link.aps.org/doi/10.1103/PhysRevLett.108.081101` (8 Feb. 2012).
74. Chen, Y.-J. *et al.* Stronger Limits on Hypothetical Yukawa Interactions in the 30–8000 nm Range. *Phys. Rev. Lett.* **116,** 221102. `https://link.aps.org/doi/10.1103/PhysRevLett.116.221102` (22 June 2016).
75. Lee, J. G., Adelberger, E. G., Cook, T. S., Fleischer, S. M. & Heckel, B. R. New Test of the Gravitational $1/r^2$ Law at Separations down to 52 μm. *Phys. Rev. Lett.* **124,** 101101. `https://link.aps.org/doi/10.1103/PhysRevLett.124.101101` (10 Mar. 2020).
76. Smith, G. L. *et al.* Short-range tests of the equivalence principle. *Phys. Rev. D* **61,** 022001. `https://link.aps.org/doi/10.1103/PhysRevD.61.022001` (2 Dec. 1999).
77. Bergé, J. *et al.* MICROSCOPE Mission: First Constraints on the Violation of the Weak Equivalence Principle by a Light Scalar Dilaton. *Phys. Rev. Lett.* **120,** 141101. `https://link.aps.org/doi/10.1103/PhysRevLett.120.141101` (14 Apr. 2018).

78. O'Hare, C. A. J. & Vitagliano, E. Cornering the axion with CP-violating interactions. *Phys. Rev. D* **102,** 115026. arXiv: 2010.03889 [hep-ph] (2020).
79. Arcadi, G., Djouadi, A. & Raidal, M. Dark Matter through the Higgs portal. *Phys. Rept.* **842,** 1–180. arXiv: 1903.03616 [hep-ph] (2020).
80. *NIST Digital Library of Mathematical Functions* https://dlmf.nist.gov/, Release 1.2.6 of 2026-03-15. F. W. J. Olver, A. B. Olde Daalhuis, D. W. Lozier, B. I. Schneider, R. F. Boisvert, C. W. Clark, B. R. Miller, B. V. Saunders, H. S. Cohl, and M. A. McClain, eds. https://dlmf.nist.gov/.
81. Birrell, N. D. & Davies, P. C. W. Quantum fields in curved space (1984).
82. Kofman, L., Linde, A. D. & Starobinsky, A. A. Towards the theory of reheating after inflation. *Phys. Rev. D* **56,** 3258–3295. arXiv: hep-ph/9704452 (1997).
83. Greene, P. B., Kofman, L., Linde, A. D. & Starobinsky, A. A. Structure of resonance in preheating after inflation. *Phys. Rev. D* **56,** 6175–6192. arXiv: hep-ph/9705347 (1997).
84. Lozanov, K. D. Lectures on Reheating after Inflation. arXiv: 1907.04402 [astro-ph.CO] (July 2019).
85. Figueroa, D. G., Florio, A., Torrenti, F. & Valkenburg, W. CosmoLattice: A modern code for lattice simulations of scalar and gauge field dynamics in an expanding universe. *Comput. Phys. Commun.* **283,** 108586. arXiv: 2102.01031 [astro-ph.CO] (2023).
86. Starobinsky, A. A. *Stochastic de sitter (inflationary) stage in the early universe* in *Field Theory, Quantum Gravity and Strings* (eds de Vega, H. J. & Sánchez, N.) (Springer Berlin Heidelberg, Berlin, Heidelberg, 1986), 107–126. ISBN: 978-3-540-39789-2.
87. Vilenkin, A. Quantum fluctuations in the new inflationary universe. *Nuclear Physics B* **226,** 527–546. ISSN: 0550-3213. https://www.sciencedirect.com/science/article/pii/0550321383902080 (1983).
88. Saikawa, K. & Shirai, S. Primordial gravitational waves, precisely: The role of thermodynamics in the Standard Model. *JCAP* **05,** 035. arXiv: 1803.01038 [hep-ph] (2018).